METAL/CERAMIC INTERFACE ENGINEERING - ADHESION STRENGTH MEASUREMENT BETWEEN DIELECTRIC CERAMIC AND ELECTRODE METAL

Chao-Yu Lee

THESE ***DISSERTATION*** **博士論文**

présentée par *submitted by* 作者

Chao-Yu LEE **李炤佑**

Pour obtenir le grade de **DOCTEUR DE L'UNIVERSITE JOSEPH FOURIER-GRENOBLE 1 (France) et de l'UNIVERSITE NATIONALE DE TAIWAN, TAPEI (Rép. de Chine)**

In partial fulfillment of the requirements for the Degree of ***DOCTOR IN THE UNIVERSITY JOSEPH FOURIER, GRENOBLE (France) and the NATIONAL TAIWAN UNIVERSITY, TAIPEI (R.O.C.)***

*以取得*法國傅立葉大學(格勒若勃,法國)及國立台灣大學(台北,中華民國)之博士學位

Spécialité :	***Speciality:***	**專長：**
Mécanique, Energétique et Ingénierie	***Mechanics, Energetics and Engineering***	**力學, 能源與工程**

INGENIERIE DES INTERFACES METAL/CERAMIQUE – MESURE DE L'ADHERENCE ENTRE UNE CERAMIQUE DIELECTRIQUE ET UN METAL D'ELECTRODE

METAL/CERAMIC INTERFACE ENGINEERING - ADHESION STRENGTH MEASUREMENT BETWEEN DIELECTRIC CERAMIC AND ELECTRODE METAL

金屬/陶瓷界面工程: 介電陶瓷與金屬電極之接著強度研究

Soutenue le 16 Juillet 2007 *Defended on July,16th, 2007* 口試日期:2007 年 7 月 16 日

Jury :		*Jury:*		口試委員
(Rapporteur)	**Pr. J.L. HUANG**	(黃肇瑞)	*(External Referee)*	*校外審閱*
(Rapporteur)	**Pr. T. PARDOEN**		*(External Referee)*	*校外審閱*
(Examinateur)	**Dr. M. BRACCINI**		*(Examinor)*	*審查*
(Examinateur)	**Pr. J. FOULETIER**		*(Examinor)*	*審查*
(Examinateur)	**Dr. J.L LOUBET**		*(Examinor)*	*審查*
(Codirecteur de Thèse)	**Pr. M. DUPEUX**		*(Co-Supervisor)*	*指導教授*
(Codirecteur de Thèse)	**Pr. W.H. TUAN**	(段維新)	*(Co-Supervisor)*	*指導教授*

Laboratoire de **S**cience et **I**ngénierie des **Ma**tériaux et des **P**rocédés, CNRS-INPG-UJF Grenoble (France)

Et Département de Science et Génie des Matériaux, NTU, Taipei (Rép. de Chine)

Laboratory of Science and Engineering of Materials and Processes, CNRS-INPG-UJF, Grenoble (France) and Department of Materials Science and Engineering, N.T.U., Taipei (R.O.C.)

材料及製程科學與工程實驗室(SIMAP), CNRS-INPG-UJF, Grenoble (法國)

及國立台灣大學材料科學與工程學系, 台北(中華民國)

Abstract

The present study investigates the mechanical strength of metal/oxide interface. Ceramic was commercial available $BaTiO_3$. Silver and nickel pastes are used as the metal materials. The metal film was prepared by screen-printing. Specimens with Ag or Ni layer, fabricated at different sintering temperatures, covering dense $BaTiO_3$ substrates with different surface roughness have been prepared with a special geometry appropriate for blister and indentation testing.

The blister test technique allows numerical estimation of interfacial adhesion strength through determination of the interfacial crack propagation energy. A simple method is proposed to correct for generalized plastic straining of silver layer. The average value of $Ag/BaTiO_3$ adhesion strength ranges from 4 J/m^2 to 7 J/m^2 according to the firing temperature of Ag. For Ni film fired at 1200°C for 2 h on dense barium titanate, the average value is about 1 J/m^2

Three indentation tests are developed to measure critical energy release rate of the same metal/oxide interfaces. The average G_{ci} of $Ag/BaTiO_3$ interface is about 0.5 J/m^2 according to normal and interface indentation tests. Cross-sectional indentation test has been also successfully performed and a new model for analysis of its results is developed. The average G_{ci} of $Ag/BaTiO_3$ interfaces are obtained from 1 J/m^2 to 3 J/m^2 according to the models.

Keywords: *blister test, interface indentation test, cross-sectional indentation test, silver, nickel, barium titanate, metal/oxide interface, adhesion strength.*

Résumé

Cette étude est consacrée à la résistance mécanique des interfaces métal/oxyde. La céramique utilisée est un titanate de baryum ($BaTiO_3$) commercial. Les matériaux métalliques sont des pâtes d'argent et de nickel. Les couches métalliques ont été obtenues par sérigraphie. Nous avons préparé des échantillons comprenant des couches d'argent et de nickel frittées à différentes températures, sur des substrats de $BaTiO_3$ de diverses rugosités, avec des géométries adaptées à des essais de gonflement-décollement et d'indentation.

La technique de gonflement-décollement permet une mesure quantitative de l'adhérence interfaciale grâce à la détermination de l'énergie de propagation G_{ci} d'une fissure interfaciale. Nous proposons une méthode simple pour prendre en compte la plasticité généralisée de la couche métallique d'argent lors du décollement. L'adhérence $Ag/BaTiO_3$ varie entre 4 J/m^2 et 7 J/m^2 selon la température de frittage de l'argent. Pour les couches de nickel frittées pendant 2 h à 1200°C sur du titanate de baryum dense, l'énergie d'adhérence moyenne est de l'ordre de 1 J/m^2.

Trois types d'essais d'indentation ont été appliqués aux mêmes interfaces métal/oxyde. La valeur moyenne de G_{ci} estimée à partir des essais d'indentation normale et interfaciale est de l'ordre de 0,5 J/m^2. Des essais d'indentation sur section transversale ont également été effectués avec succès et un nouveau modèle est proposé pour l'analyse de leurs résultats. Selon le modèle de dépouillement utilisé, la moyenne des énergies d'adhérence $Ag/BaTiO_3$ s'établit entre 1 et 3 J/m^2.

Mots-clés : essai de gonflement-décollement, essais d'indentation interfaciale, essai d'indentation sur section transversale, argent, nickel, titanate de baryum, interface métal/oxyde, adhérence interfaciale.

摘要

本論文是研究金屬與陶瓷界面的機械強度性質，陶瓷是使用商用鈦酸鋇粉，金屬部分為銀膏及鎳膏所製成的金屬膜，膜的成型方是為網版印刷法。使用不同表面性質的緻密鈦酸鋇做為基板，金屬膏覆蓋在陶瓷基板上並在不同溫度下燒結，試片加工製成特殊形狀以符合 Blister test 的試片形狀要求。

Blister test 可以得到量化的介面強度，並可由此得出介面裂縫延伸的所需的能量，在實驗過程中會伴隨著塑性變形，在本實驗中我們提出一個簡單的處理方法以減去塑性變形的影響。在不同銀膠燒結溫度下，銀及鈦酸鋇的界面強度落在 4 -7 J/m2 之間，鎳及鈦酸鋇的界面強度約為 1 J/m2。

本實驗中嘗試發展三種 indentation 方法來量測相同的金屬與陶瓷界面的強度，經由 normal 及 interface indentation 所得出的銀與碳酸鋇的界面強度約為 0.5 J/m2. 第三種測試方法 Cross-sectional indentation test 為本研究中發展出的全新測試方法，並提出一種新的理論分析。依照不同的分析模型，所得出的銀與碳酸鋇的界面強度約為 1 到 3 J/m2.

關鍵字： blister test， interface indentation test， cross-sectional indentation test， 銀， 鎳， 鈦酸鋇， 金屬陶瓷界面， 接著強度

Acknowledgments

I would first like to express my sincere appreciation to my advisors, Professor Wei-Hsing TUAN and Professor Michel DUPEUX, for their guidance, concern, understanding, advice, and support through my study and research at National Taiwan University and Université Joseph Fourier. They were always willing to give me a hand when I met any troubles with academics or life in general.

I also wish to acknowledge my other committee members, Prof. Thomas PARDOEN, Prof. Jow-Lay HUANG, Prof. Jacques FOULETIER, Dr. Jean-Luc LOUBET and Dr. Muriel BRACCINI for serving on my advisory committee, as well as for useful suggestions on my research work.

Thank you to Institut Français de Taipei and National Taiwan University for funding this research. I would also like to thank the Material Science and Engineering Department at National Taiwan University and Laboratory of Science et Ingénierie des MAtériaux et Procédés (previous known as Laboratoire de Thermodynamique et de Physico-Chimie Métallurgiques) for providing research facilities.

I would like to thank my parent for their constant support and understanding over the years. I would like to thank my friends, both in Taiwan and France, for their support and encouragement. I will never forget those who had helped me. I specially want to thank Ya-Hsiu TAI for her inspiration and care.

Table of Contents

Introduction **1**

Chapter Ⅰ: Metal/Oxide Interfaces **3**

1. Introduction 5
2. Metal-oxide interfaces 5
   - 2.1. Formation of metal/oxide interface 5
   - 2.2. Interface chemistry and atomic structure 5
   - 2.3. Fracture behavior of metal-oxide interface 7
   - 2.4. Metal-oxide adhesion 12
3. Metal-oxide adhesion measurement 14
   - 3.1. Tape test 14
   - 3.2. Pin Pull test 14
   - 3.3. Peel test 15
   - 3.4. Scratch test 16
   - 3.5. Beam bending test 17
   - 3.6. Indentation test 19
   - 3.7. Laser spallation technique 19
   - 3.8. Telephone cord delamination method 20
   - 3.9. Interface indentation test 21
   - 3.10. Cross-sectional nanoindentation test 21
   - 3.11. Blister test 22
4. Conclusions 23

References 24

Chapter II: Interface Adhesion Measurement by Blister Test **27**

1. Introduction 29
2. Development of the blister test 30
3. Mechanical analysis 32
   - 3.1. Nomenclature 32
   - 3.2. Criterion for debonding 33
   - 3.3. Crack extension force 34
   - 3.4. Near edge loads 45
   - 3.5. Mode mixity in blister test 47
   - 3.6. Correction for plastic work 48

4. Conclusions 50
References 51

Chapter Ⅲ: Interface Adhesion Measurement by Indentation Test 55

1. Introduction 57
2. Development of the indentation test for measuring interfacial fracture toughness. 59
   2.1. Development of the normal indentation test 59
   2.2. Development of the interface indentation test 59
   2.3. Development of the cross-sectional indentation test 60
3. Mechanical analysis 60
   3.1. Normal indentation test 60
   3.2. Interface indentation test 61
   3.3. Cross-sectional indentation test 63
      3.3.1 The Plate model 63
      3.3.2. Analytical approximation (Tapered beams model) 64
      3.3.3. The model of an elastic plate with elastically restrained edges 68
      3.3.4. Point load model 73
4. Mode mixity of cross-sectional indentation test 73
5. Conclusions 75
References 76

Chapter Ⅳ: Experiments 79

1. Materials 81
   1.1. Barium Titanate 81
   1.2. Metals 82
2. Blister test 84
   2.1. Blister test apparatus 84
      2.1.1.Sample mounting 85
      2.1.2.Data acquisition system 86
      2.1.3.Theory of fringe projection method: 88
   2.2. Sample preparation for Blister test 93
      2.2.1.Silver (Ag)/Barium Titanate ($BaTiO_3$) 93
      2.2.2.Nickel (Ni)/Barium Titanate ($BaTiO_3$) 96
      2.2.3.Nickel (Ni)/Silver (Ag)/ Barium Titanate ($BaTiO_3$) 97
      2.2.4.Silver (Ag)/Nickel (Ni) 98
3. Indentation test 98
   3.1. Indentation test apparatus 98

3.2. Sample preparation for indentation test 98
3.2.1Interface and cross-sectional indentation test 98
3.2.2Normal indentation test 99
4. Conclusions 100
References 101

Chapter Ⅴ: Results and discussion **103**

1. Blister test 105
1.1. Silver (Ag)/Barium Titanate ($BaTiO_3$) 106
1.1.1. Influence of different silver film firing temperature 107
1.1.2. Influence of different substrate roughness 116
1.1.3. Influence of different substrate firing temperature 120
1.2. Nickel (Ni)/Barium Titanate ($BaTiO_3$) 122
1.3. Nickel (Ni)/Silver (Ag)/ Barium Titanate ($BaTiO_3$) 126
1.4. Silver (Ag)/Nickel (Ni) 128
2. Indentation test 129
2.1. Normal indentation test 129
2.2. Interface indentation test 132
2.3. Cross-sectional indentation test 135
3. Comparison between blister and indentation test 139
3.1. Comparison between G_{ci} from normal indentation test with the values from blister test. 139
3.2. Comparison between G_{ci} from interface indentation test with the values from blister test. 139
3.3. Comparison between G_{ci} from cross-sectional indentation test with the values from blister test. 140
4. Conclusions 140
4.1. Silver (Ag)/Barium Titanate ($BaTiO_3$) 140
4.2. Nickel (Ni)/Barium Titanate ($BaTiO_3$) 141
4.3. Nickel (Ni)/Silver (Ag)/ Barium Titanate ($BaTiO_3$) 141
4.4. Silver (Ag)/Nickel (Ni) 141
References 142

Chapter VI: General conclusions and future work **145**

Published Work **151**

Appendix I **153**

List of Figure

Figure 1-1: Misfit strain in a hypothetical interface between a single cubic metal (top) and a single cubic oxide (bottom) 6
Figure 1-2: Three principal modes of fracture with applied forces F. 7
Figure 1-3: Fracture mechanisms for metal-oxide interfaces. 8
Figure 1-4: Plane strain geometry of an interface crack 8
Figure 1-5: Definition of the contact angle at drops. 13
Figure 1-6: Definition of the contact angle at pores. 13
Figure 1-7: The Pin Pull test 15
Figure 1-8: The Peel test 16
Figure 1-9: The Scratch test 17
Figure 1-10: The double cantilever beam 18
Figure 1-11: The Four-point bending geometry 18
Figure 1-12: The procedure of indentation test 19
Figure 1-13: Schematic of laser spallation experiment 20
Figure 1-14: illustration of telephone cord buckles 21
Figure 1-15: Principle of the interface indentation test 21
Figure 1-16: Principle of the Cross-sectional nanoindentation test 22
Figure 1-17: The blister test. 22
Figure 2-1: Cross-sectional view of the bulge test (a) and the blister test (b). 29
Figure 2-2: Schematic of the data of the bulge and blister test. The square points denote the real experimental results 30
Figure 2-3: Island blister test. 31
Figure 2-4: Constrained blister test. 31
Figure 2-5: Schematic of blister growth 34
Figure 2-6: The cross-sectional view of blister test 35
Figure 2-7: The constant C for blister equation 41
Figure 2-8: The constitutive relation $\rho(\omega_0)$ 42
Figure 2-9: The fracture parameter C for various approaches 43
Figure 2-10: The fracture parameter C for various approaches. 44
Figure 2-11: Forces at blister edge. 46
Figure 2-12: A families of interface toughness functions. 48
Figure 2-13: schematic of the principle of correction for the effect of the generalized plasticity of the silver membrane on the interfacial debonding energy. 49

Figure 2-14: Illustration of blister equation fit to experimental data for a specimen fired at 850°C. The uncorrected value G = 11 J/m^2 is adjusted on the experimental debonding point. The corrected value G' = 4.5 J/m^2 is adjusted on the corrected debonding height, according to the schematic of figure 2-13. 50
Figure 3-1: Principle of the normal indentation test. 57
Figure 3-2: Principle of the interface indentation test 57
Figure 3-3: Schematic of CSN test configuration 58
Figure 3-4: Principle of the cross-sectional indentation test. 58
Figure 3-5: Schematic of the geometry of a chipped segment showing the dimensions used in calculating interfacial toughness 61
Figure 3-6: sketch of a cross-sectional indentation test. 64
Figure 3-7: Plate model as an assembly of taped beams 64
Figure 3-8: The function $2F(\lambda)+\lambda F'(\lambda)$ calculated for small aspect ratio $\lambda = b/a$ (λ<0.1). 66
Figure 3-9: The function $2F(\lambda)+\lambda F'(\lambda)$ calculated for aspect ratio $\lambda = b/a$ (λ<1). 67
Figure 3-10: The relationship of function F(a, b) and indentation size b and crack length a (both in meter). 67
Figure 3-11: The model of an elastic plate with elastically restrained edges 68
Figure 3-12: The function $2F(\lambda)+\lambda F'(\lambda)$ calculated for small aspect ratio $\lambda = b/a$ (elastically restrained edges model). 71
Figure 3-13: The function $2F(\lambda)+\lambda F'(\lambda)$ calculated for aspect ratio $\lambda = b/a$ (elastically restrained edges model). 71
Figure 3-14: The relationship of function F(a, b) and indentation size b and crack length a (both in meter) (elastically restrained edges model). 72
Figure 3-15: Comparison of energy release rate calculated by elastically restrained edges model and tapered beams model. 72
Figure 3-16: The variation of ω(α, β) for β=0 or β=α/4 74
Figure 3-17: the mode mixity of interface crack tip for several levels of elastic mismatch for a blister under a point load 75
Figure 4-1:The phase diagram of BaO/TiO_2. 82
Figure 4-2: The phase diagram of Ag/O. 83
Figure 4-3: The phase diagram of Ni/O. 83
Figure 4-4: The phase diagram of AgNi. 84
Figure 4-5: blister test apparatus 84
Figure 4-6: Photograph of the blister apparatus. 85
Figure 4-7: Sample mounting 85
Figure 4-8: Illustration of the complete blister system 87

Figure 4-9: Photograph of the complete blister system 87
Figure 4-10: Cross-sectional view of the fringe projection with (a) equidistance and (b) non-equidistance. 88
Figure 4-11: Images with (a) equidistance and (b) non-equidistance 88
Figure 4-12: The induced phase shift due to a mirror translation at non-normal incidence 90
Figure 4-13: Real Image in the CCD 91
Figure 4-14: Image of calculated phase analyzed by four phase-stepping. 91
Figure 4-15: Fringe projection geometry. 91
Figure 4-16: Subtraction of 2 images {reference (Fig.4-7(a))-deformed (Fig.4-7(b))}. 92
Figure 4-17: Filtered image of Fig. 4-16. 92
Figure 4-18: Measurement of the deformation of the blister test. 93
Figure 4-19: 3D image of the deformation of the blister test. 93
Figure 4-20: The flow chart for the preparation of $BaTiO_3$ substrate. The heating and cooling rate are 3℃/min in both firing stages. 94
Figure 4-21: The flow chart for the preparation of silver membrane use to cover the central hole of the substrate discs. The heating and cooling rate are 3 ℃/min 95
Figure 4-22: The flow chart for the preparation of blister test sample ($Ag/BaTiO_3$). The heating and cooling rate are 3 ℃/min. 95
Figure 4-23: After firing, the nickel film separates totally from the substrate. 96
Figure 4-24: The flow chart for the preparation of blister test sample ($Ni/BaTiO_3$). The heating and cooling rates are 3 ℃/min. 97
Figure 4-25: The flow chart for the preparation of blister test sample ($Ni/Ag/BaTiO_3$). The heating and cooling rate are 3 ℃/min. 97
Figure 4-26: The flow chart for the preparation of blister test sample (Ag/Ni). The heating and cooling rate are 3℃/min. 98
Figure 4-27: The flow chart for the sample preparation of cross-sectional indentation test ($Ag/BaTiO_3$). 99
Figure 5-1: The images of blister growth captured by CCD camera. (1) Free standing window begins to bulge without film separation. (2) Film starts to separate from substrate at critical pressure. (3) Film continues separating from substrate with pressure decrease. 105
Figure 5-2: The X-ray diffraction pattern of both surfaces (noncontact or contact with $BaTiO_3$) of silver film. 106
Figure 5-3: SEM micrographs of silver film sintered at (a) 600℃ (b)700℃ (c)800℃ (d)900℃ for 1 hour. 107
Figure 5-4: Cross-section views of $Ag/BaTiO_3$ interfaces. Ag films were fired at (a) 600 ℃ (b) 700℃ (c) 800℃ (d) 850 ℃ for 1 hour. 108

Figure 5-5: The experimental data acquired from blister test, Ag fired at 600℃, and the fitting blister equation, for 4.5 J/m^2. *110*
Figure 5-6: The experimental data acquired from blister test, Ag fired at 700℃, and the fitting blister equation, for 4.75 J/m^2. *111*
Figure 5-7: The experimental data acquired from blister test, Ag fired at 800℃, and the fitting blister equation, for 5.8 J/m^2. *111*
Figure 5-8: The experimental data acquired from blister test, Ag fired at 850℃, and the fitting blister equation, for 6.6 J/m^2. *112*
Figure 5-9: Weibull modulus plots of four silver sintering temperatures (a) 600℃ (b)700℃ (c)800℃ (d)850℃. *113*
Figure 5-10: Average G_{ci} of interface versus sintering temperature of Ag membrane. *113*
Figure 5-11: Average fracture energy of interface versus average porosity of silver membrane. ■ Silver paste fabricated by ceramic matrix composite laboratory (NTU); ● Commercial silver paste *114*
Figure 5-12: The experimental data acquired from blister test and the fitting blister equation, for G_{ci}= 3.73 J/m^2. Ag is fired at 850℃ and $BaTiO_3$ is fired at 1440℃. The average surface roughness of $BaTiO_3$ substrate is 0.21μm *117*
Figure 5-13: The experimental data acquired from blister test and the fitting blister equation, G_{ci}= 6.48 J/m^2. Ag is fired at 850℃ and $BaTiO_3$ is fired at 1440℃. The average surface roughness of $BaTiO_3$ substrate is 0.15μm. *118*
Figure 5-14: Weibull modulus plots of (a) 1440D and (b) 1440S. *119*
Figure 5-15: The experimental data acquired from blister test and the fitting blister equation, for 3.88 J/m^2. Ag is fired at 850℃ and $BaTiO_3$ is fired at 1350℃. The average surface roughness of $BaTiO_3$ substrate is 0.21μm *120*
Figure 5-16: The X-ray diffraction pattern of $BaTiO_3$ sintered at two different temperatures. *121*
Figure 5-17: The microstructure of $BaTiO_3$ fired at (a) 1350℃ (b) 1440℃ for two hours (SEM). *121*
Figure 5-18: The experimental data and critical energy release rates G_{ci} of the $BaTiO_3$/Ni interface, with the fitting blister equation for 1.26J/m^2. *123*
Figure 5-19: Nickel film fired over the melting point on barium titanate substrate in argon atmosphere. *123*
Figure 5-20: The cross-section view of Ni/$BaTiO_3$ interface *124*
Figure 5-21: The experimental data and critical energy release rates G_{ci} of the interface between $BaTiO_3$ and reduced Ni, with the fitting blister equation for 1.06J/m^2. *125*
Figure 5-22: The blister test data of Ni/Ag/$BaTiO_3$. *127*
Figure 5-23: the cross section view of Ni/ Ag/ $BaTiO_3$ sandwich structure, upper layer is Ni film, middle layer is Ag film and lower layer is $BaTiO_3$. *128*

Figure 5-24: The blister test data of Ag/Ni interface adhesion. 129
Figure 5-25: Indentation induced of a Ni coating (optical micrograph) 130
Figure 5-26: Coating detachment during loading of the indentation for a 400 nm thick silver film on $BaTiO_3$ substrate (optical microscopy). 130
Figure 5-27: Coating detachment during loading of the indentation for a 400nm thick nickel film on $BaTiO_3$ substrate (optical microscopy). 131
Figure 5-28: Plot of indentation load versus interfacial crack radius after normal indentation 131
Figure 5-29: The energy of interfacial crack extension of silver and nickel thin coatings on barium titanate, from normal indentation tests. 132
Figure 5-30: Cross-section of $Ag/BaTiO_3$ interface (a) SE mode (b) BSE mode (scanning electron microscopy). 133
Figure 5-31:The effect of the constant α for interface indentation equation on calculated G_{ci} for $Ag/BaTiO_3$ and a_c=67.9 μm. 135
Figure 5-32: The cross-sectional indentation test with a Vickers indent. 135
Figure 5-33: SEM photographs of cross-sectional indentation test with a Vickers indent 136
Figure 5-34: G_{ci} of $Ag/BaTiO_3$ (1350D) interface measured by different model on 5 different interface locations. 138
Figure 5-35: G_{ci} of $Ag/BaTiO_3$ (1440S) interface measured by different model on 6 different interface locations. 139
Figure 5-36: G_{ci} of $Ag/BaTiO_3$ interface measured by blister test and different model of cross-sectional indentation test. 140

List of Table

Table 2-1: List of variables. 32
Table 2-2: Numerical solutions of A_0 36
Table 2-3: the membrane crack extension force factor Cm 44
Table 2-4: the coefficients for crack extension force factor C, for small deflections 44
Table 2-5 summary of some reported equations of the energy release rate. 45
Table 4-1: The intrinsic properties of the materials used in this study. 81
Table 4-2: The characteristics of $BaTiO_3$ *powder used in the present study.* 81
Table 4-3: The characteristics of silver powder used in the present study. 82
Table 4-4: The characteristics of nickel powder used in the present study. 83
Table 5-1: The resulting critical energy release rates Gci of the $BaTiO_3$*/Ag interfaces for each Ag paste sintering temperature* 109
Table 5-2: The resulting critical energy release rates G_{ci} *of the* $BaTiO_3$*/Ag interfaces for different substrate surface roughness (the firing temperature of* $BaTiO_3$ *is 1440°C for 2 h).* 117
Table 5-3: The resulting critical energy release rates G_{ci} *of the* $BaTiO_3$*/Ag interfaces for different substrate surface roughness (the firing temperature of* $BaTiO_3$ *is 1350℃ for 2 h).* 119
Table 5-4: The resulting critical energy release rates G_{ci} *of the* $BaTiO_3$*/Ag interfaces for different substrate firing temperature.* 122
Table 5-5: The resulting critical energy release rates G_{ci} *of the* $BaTiO_3$*/Ni interfaces.* 126
Table 5-6: The critical energy release rates G_{ci} *of the Ni/Ag/*$BaTiO_3$ *structure.* 127
Table 5-7: Parameters used to calculate G_{ci} *in interface indentation test.* 134
Table 5-8: G_{ci} *in interface indentation test for Ag/*$BaTiO_3$ *(1350D) specimens.* 134
Table 5-9: Experimental data and calculated interface energy release rate by four models for cross-sectional Vickers indentation tests on Ag/$BaTiO_3$ *interfaces.* 137

Introduction:

The characteristics of the metal-ceramic interfaces are of major importance for many technical applications such as electronic packaging, multilayer ceramic capacitors (MLCC), wear resistance coatings on metal, functional metal-ceramic composites and micro electromechanical systems (MEMS). In many applications, the metal-ceramic interfaces play a key role in the performance of the material. The characteristics of the metal-ceramic interfaces include mechanical, electrical, thermodynamic, optical characteristics. The mechanical properties are more important than the others because all the applications require mechanical reliabilities, even if these are designed for their electric, magnetic or optical properties.

In the present study we investigate the characteristics of the interface between the electrode materials (silver and nickel) and dielectric ceramic (barium titanate), both of which are essentially used in multilayer ceramic capacitors. The adhesion strength between silver, nickel electrodes and barium titanate has been determined by means of blister test, interface indentation test and cross-sectional indentation test in this study. The blister test has been developed for a long time but is not widely used due to the difficulty of sample preparation. The indentation tests, such as normal indentation test, interface indentation test and cross-sectional indentation test, are developing at present. Each technique has advantages and disadvantages, the results of these test methods will be compared with the others.

Outline:

The objectives of this thesis are using the blister test and indentation test to characterize the mechanical properties of metal films/barium titanate interface and the adhesion strength between metal films and barium titanate. The electrode metals are silver and nickel.

Chapter 1 describes the characteristics of metal-oxide interface. A brief introduction of the mechanic properties and fracture behavior of metal-oxide interface is presented, and we also present the common techniques for measuring adhesion strength of metal-oxide interfaces.

Chapter 2 focuses on the blister test technique. We review the development of blister techniques for measuring interface adhesion. A theoretical analysis of the blister test is presented. The energetic of a debonding blister, built on the models of window deformation, is analyzed to determine the crack extension force. A simple model is consistent with complex solutions.

Chapter 3 presents the normal indentation, interface indentation and cross-sectional indentation techniques. A simple review of the development of normal, interface and cross-sectional indentation techniques for measuring interface adhesion was made. A theoretical analysis of the interface indentation test is presented. The energetic of debonding is analyzed to determine the crack extension force for cross-sectional indentation. Four models for cross-sectional indentation test are presented in this chapter.

In Chapter 4, some intrinsic properties of raw materials are described. The apparatus for blister experiment are presented. We describe the method to measure the deflection of the metal membranes and the method we used to fabricate the samples for blister test and indentation test.

Chapter 5 presents the results of metal/oxide adhesion which are measured by blister test and indentation test. The results obtained from blister test are analyzed and discussed. For indentation test, several experiments are made and the results are analyzed. The results of interface adhesion are compared with which acquired from blister test.

At last, we summarize our findings at present; we make several conclusions and suggestions in chapter 6.

Chapter Ⅰ

Metal/Oxide Interfaces

1. Introduction 5
2. Metal-oxide interfaces 5
   2.1. Formation of metal/oxide interface 5
   2.2. Interface chemistry and atomic structure 5
   2.3. Fracture behavior of metal-oxide interface 7
   2.4. Metal-oxide adhesion 12
3. Metal-oxide adhesion measurement 14
   3.1. Tape test 14
   3.2. Pin Pull test 14
   3.3. Peel test 15
   3.4. Scratch test 16
   3.5. Beam bending test 17
   3.6. Indentation test 19
   3.7. Laser spallation technique 19
   3.8. Telephone cord delamination method 20
   3.9. Interface indentation test 21
   3.10. Cross-sectional nanoindentation test 21
   3.11. Blister test 22
4. Conclusions 23
References 24

1. Introduction

The metal-oxide interface is one of the key problems and has vast technological significance in contemporary materials science. Metal-oxide interfaces are important in many applications such as structural composites, electroceramic devices, and environmental coatings. Oxide ceramics have been used in a variety of applications that take advantage on their optical, electrical properties, chemical resistance, high thermal performance, and resistance to environmental degradation. Basic researches on metal-oxide interface focus on adhesion, interface structure, chemistry and mechanical behavior **[Ernst 1995, Sinnott 2003].**

2. Metal-oxide interfaces

2.1. Formation of metal/oxide interface

There are various methods to produce metal/oxide interface such as internal oxidation of alloys, internal reduction of oxides, epitaxial growth of thin films and solid state bonding etc. On a macroscopic scale, solid state bonding allows fabricating almost any desired metal/oxide interface. Solid state bonding is often regarded as diffusion bonding. For metal/oxide interfaces, metal is more likely to diffuse into oxide. Optimum metal/oxide interfaces require heating. Higher temperature promotes removal of voids in interface and increase metal/oxide contact area, but also introduces higher residual stress during cooling. The thermal residual stress usually affects the structure and mechanical behavior of solid state bonded metal/oxide interfaces **[Ernst 1995]**.

2.2. Interface chemistry and atomic structure

There are many types of metal-oxide interfaces. Chemically, they may be broadly categorized as reactive and non-reactive. Reaction between metal and oxide forms a tertiary phase at the interface. In interfaces, both the metal and the oxide phase may be stable over a particular range of oxygen activities. Therefore, no interfacial reaction phases will be present **[Sinnott 2003]**. In this study we will focus on non-reactive interfaces.

There is no precise correlation between the energy of metal-oxide interface and its crystallography. To explain the crystallography of interface, the physical interaction between the metal and the oxide at the interface should be taken into consideration. The crystallography and the atomic interaction both influence the relative thermodynamic stability of the interface. Because the atomic interactions in metals are widely different from those in oxides, it is difficult to determine the physical interaction at metal-oxide interface.

Typically, hetero phase interfaces are not perfectly lattice matched. The atoms in metals or in oxides usually arrange in lattice places, which are different from the plane of the interface. At the metal-oxide interface the inter-atomic spacing of the two crystals cannot correspond with each other. Hence the two crystals tend to get "out of register" between these positions, and the interfacial atoms occupy positions where they may increase potential energy. Owing to the atoms replacing to positively advantageous positions, the strain exists to fit the energy equilibrium. Since the oxide is usually much stiffer than the metal, such "misfit strains" occur mainly in the metal. Figure 1-1 depicts a misfit strain in a hypothetical metal-oxide interface.

The misfit strains are accompanied with misfit stress. Misfit stress adds to the stress field that drives a crack tip through the interface and may enhance the segregation of impurities to the interface. In other words, the misfit strains influence the properties of metal-oxide interfaces.

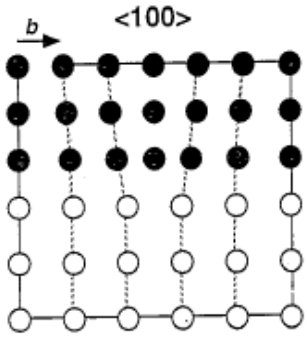

Figure 1-1: Misfit strain in a hypothetical interface between a single cubic metal (top) and a single cubic oxide (bottom) ***[*Ernst 1995*]***

In general, most of the metal-oxide interfaces are thermodynamically unstable if they have no abrupt chemical profile, and can have diffusion reactions. Such diffusion reactions include impurity segregation, mutual dissolution and inter-phases formation. Impurity segregation at the interface can definitively control the bonding and electronic properties. Whereas the reactions usually occur on the micrometer scale and may change the microscopic structure, it may alter the macroscopic properties, such as mechanical and electrical properties. High temperature is necessary to induce diffusion reactions; therefore, diffusion reactions are of major importance for metal-oxide interface applications at high temperature.

Computer modeling of metal-oxide interface becomes an important tool to predict and to understand many aspects of the metal-oxide adhesion. Recently, several different theoretical methods have been made available to study metal-oxide interfaces, like thermodynamic models, image charge models, empirical or semi-empirical atomistic calculation methods, and ab-initio atomistic calculation method **[Ernst 1995]**. Each method has its advantages and limits.

2.3. Fracture behavior of metal-oxide interface

Most of technological applications containing metal-oxide interfaces require strong, stable interfaces, even if these are designed for their electrical properties. For linear elastic fracture mechanics, there are three distinct types of loading which a crack can experience, and each load orientation has its own designation. These different loading geometries are regularly referred to as modes Ⅰ, Ⅱ, and Ⅲ. Mode Ⅰ is the principal mode of fracture that occurs when a crack is being opened by tensile forces which are applied perpendicularly to the crack plane as shown in Figure 1-2-a. Mode Ⅱ corresponds to in-plane shear loading and tends to slide one face of crack with respect to the other perpendicular to the crack front line. Mode Ⅱ is sometimes called the sliding mode of fracture as shown in Figure 1-2-b. Mode Ⅲ refers to out-of-plane shear and often called as the tearing mode of fracture or the anti-plane crack problem (Figure 1-2-c). The out-of-plane shear acting on a plate is the same manner as the one uses to tear a sheet of paper. The most important loading mode is mode Ⅰ, since it is the most frequently observed. Indeed, the crack propagation needs less energy per unit crack area in pure mode I than in mode Ⅱ, Ⅲ or mixed.

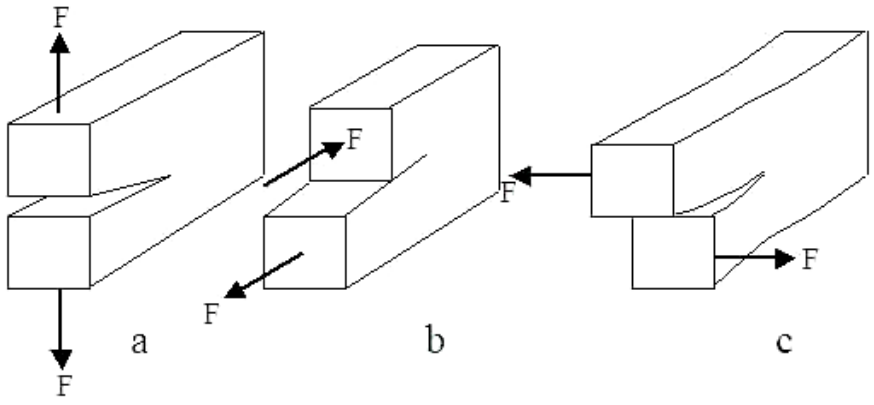

Figure 1-2: Three principal modes of fracture with applied forces F.

Similar to homogeneous solids, metal-oxide interface de-bonds either by brittle or by ductile fracture. Ductile fracture occurs mainly in the metal. The commonly observed stages in ductile interface fracture are **[Knott 1977, Wilsforf 1983, Garrison 1980]**:

(1): Formation of a free surface by stress-induced nucleation of voids.

(2): Growth of the voids by means of plastic strain and hydrostatic stress.

(3): Coalescence of the growing voids with adjacent voids.

Brittle fracture happens by bond rupture at the metal-oxide interface; the new surface grows along the metal-oxide interface. The fracture energy of brittle fracture (energy required to fracture a unit area of interface) is smaller than the fracture energy of ductile fracture; nevertheless, because of local stress concentration effects, brittle

fracture generally also includes extensive plastic deformation of the metal in a plastic zone near the crack tip (Figure 1-3). This so-called "confined" plastic deformation of metal consumes a large amount of the fracture energy of interface; it results in higher work of adhesion. The fracture energy thus depends on the thickness and the yield strength of the metal.

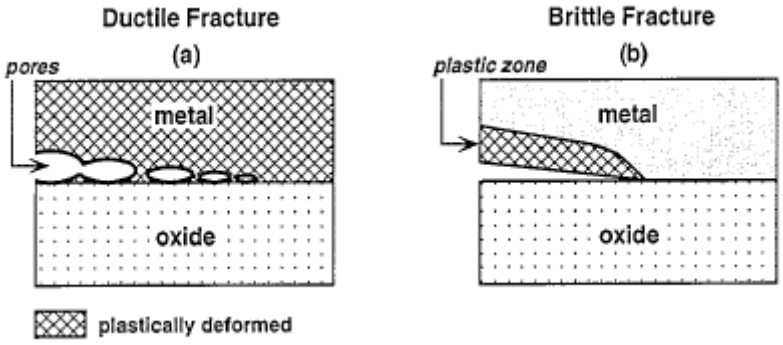

Figure 1-3: Fracture mechanisms for metal-oxide interfaces ***[*Evans 1988, 1993*]***.

The metal and the oxide usually have different elastic constants; this mismatch of elastic constants across metal-oxide interfaces complicates their fracture behaviors. The elastic mismatch especially affects the stress distribution around the crack tip at the metal-oxide interface. Consider the plane strain geometry of a sharp interface crack between two variants in isotropic and linear elastic solids as shown in Figure 1-4.

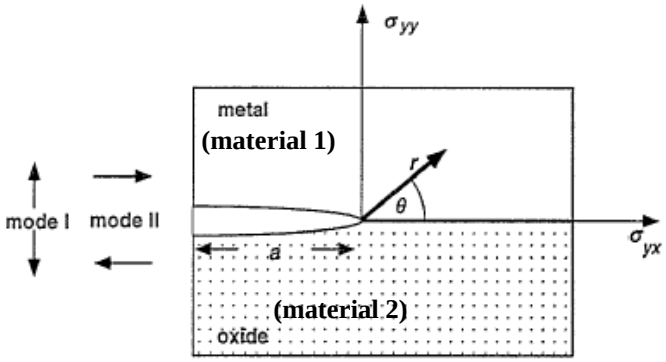

Figure 1-4: Plane strain geometry of an interface crack ***[*Ernst 1995*]***

The stress field of such a crack depends on two non-dimensional elasticity parameters, introduced by Dundurs **[Dundurs 1969]**:

$$\alpha = \frac{G_1(1-\nu_2) - G_2(1-\nu_1)}{G_1(1-\nu_2) + G_2(1-\nu_1)}$$

$$\beta = \frac{1}{2}\left[\frac{G_1(1-2\nu_2) - G_2(1-2\nu_1)}{G_1(1-\nu_2) - G_2(1-\nu_1)}\right] \qquad (1\text{-}1)$$

where G_1, G_2, ν_1 and ν_2 denote the shear moduli and Poisson numbers of the material 1 and 2 (Figure 1-4). The Dundurs parameters α and β indicate the mismatch of elastic

constants between the two connected materials. Constant α can also be expressed as

$$\alpha = \frac{\overline{E}_1 - \overline{E}_2}{\overline{E}_1 + \overline{E}_2} \tag{1-2}$$

where $\overline{E}_i = E_i/(1-\nu_i^2)$ for plane strain and $\overline{E}_i = E_i$ for plane stress, and E_i are the Young's moduli of materials.

The singular stress field in the vicinity of the tip of the interfacial crack is given by Rice et al. **[Rice 1990]**

$$\sigma_{ij} = \frac{1}{\sqrt{2\pi r}}\left[\mathrm{Re}(Kr^{i\varepsilon})\sigma_{ij}^{I}(\theta,\varepsilon) + \mathrm{Im}(Kr^{i\varepsilon})\sigma_{ij}^{II}(\theta,\varepsilon)\right](i,j=x,y) \tag{1-3}$$

Where $i = \sqrt{-1}$ and

$$\varepsilon = \frac{1}{2\pi}\ln\left(\frac{1-\beta}{1+\beta}\right) \tag{1-4}$$

$K = K_I + iK_{II}$ is the complex interface stress intensity factor. The real and imaginary parts K_I and K_{II} have similar roles as the stress intensity factors for mode I and mode II. The quantities $\sigma_{ij}^{I}(\theta,\varepsilon)$ and $\sigma_{ij}^{II}(\theta,\varepsilon)$ are angular functions. For material 1 in plane polar coordinates (r,θ) they are given by

$$\sigma_{rr}^{I} = -\frac{\sinh\varepsilon(\pi-\theta)}{\cosh\pi\varepsilon}\cos\frac{3\theta}{2} + \frac{e^{-\varepsilon(\pi-\theta)}}{\cosh\pi\varepsilon}\cos\frac{\theta}{2}\left(1+\sin^2\frac{\theta}{2}+\varepsilon\sin\theta\right) \tag{1-5}$$

$$\sigma_{r\theta}^{I} = \frac{\sinh\varepsilon(\pi-\theta)}{\cosh\pi\varepsilon}\sin\frac{3\theta}{2} + \frac{e^{-\varepsilon(\pi-\theta)}}{\cosh\pi\varepsilon}\sin\frac{\theta}{2}\left(\cos^2\frac{\theta}{2}-\varepsilon\sin\theta\right) \tag{1-6}$$

$$\sigma_{\theta\theta}^{I} = \frac{\sinh\varepsilon(\pi-\theta)}{\cosh\pi\varepsilon}\cos\frac{3\theta}{2} + \frac{e^{-\varepsilon(\pi-\theta)}}{\cosh\pi\varepsilon}\cos\frac{\theta}{2}\left(\cos^2\frac{\theta}{2}-\varepsilon\sin\theta\right) \tag{1-7}$$

$$\sigma_{rr}^{II} = \frac{\cosh\varepsilon(\pi-\theta)}{\cosh\pi\varepsilon}\sin\frac{3\theta}{2} - \frac{e^{-\varepsilon(\pi-\theta)}}{\cosh\pi\varepsilon}\sin\frac{\theta}{2}\left(1+\cos^2\frac{\theta}{2}-\varepsilon\sin\theta\right) \tag{1-8}$$

$$\sigma_{r\theta}^{II} = \frac{\cosh\varepsilon(\pi-\theta)}{\cosh\pi\varepsilon}\cos\frac{3\theta}{2} + \frac{e^{-\varepsilon(\pi-\theta)}}{\cosh\pi\varepsilon}\cos\frac{\theta}{2}\left(\sin^2\frac{\theta}{2}+\varepsilon\sin\theta\right) \tag{1-9}$$

$$\sigma_{\theta\theta}^{II} = -\frac{\cosh\varepsilon(\pi-\theta)}{\cosh\pi\varepsilon}\sin\frac{3\theta}{2} - \frac{e^{-\varepsilon(\pi-\theta)}}{\cosh\pi\varepsilon}\sin\frac{\theta}{2}\left(\sin^2\frac{\theta}{2}+\varepsilon\sin\theta\right) \tag{1-10}$$

For stresses in material 2, π should be changed to –π in the above equations.

The singular stresses on the interface along the crack ligament are given by

$$\sigma_{22} = \frac{\mathrm{Re}(Kr^{i\varepsilon})}{\sqrt{2\pi r}}, \quad \sigma_{12} = \frac{\mathrm{Im}(Kr^{i\varepsilon})}{\sqrt{2\pi r}} \tag{1-11}$$

where $r^{i\varepsilon} = \cos(\varepsilon \ln r) + i \sin(\varepsilon \ln r)$.

The stresses present an oscillatory singularity, which causes some complications for crack along bi-material interfaces.

The displacements of the crack surfaces at a distance *r* behind the crack tip $\delta_i = u_i(r, \theta = \pi) - u_i(r, \theta = -\pi)$ are given by

$$\delta_2 + i\delta_1 = \frac{8}{(1+2i\varepsilon)\cosh(\pi\varepsilon)} \frac{K_I + iK_{II}}{E_*} \sqrt{\frac{r}{2\pi}} r^{i\varepsilon} \tag{1-12}$$

Where

$$\frac{1}{E_*} = \frac{1}{2}\left(\frac{1}{\overline{\overline{E}}_1} + \frac{1}{\overline{\overline{E}}_2}\right) \tag{1-13}$$

The energy released during crack extension is the work performed by the stresses acting through the displacements. The strain energy release rate for crack growth along the interface can be obtained from Equations 1-11, 1-12:

$$G = \frac{(1-\beta^2)}{E_*}(K_I^2 + K_{II}^2) \tag{1-14}$$

Equation 1-14 can reduce to $G_I = \frac{(1-\nu^2)}{E} K_I^2$ and $G_{II} = \frac{(k+1)}{8\mu} K_{II}^2$ for mode I and mode II for similar materials (ε=0), where $k = \frac{E}{3(1-2\nu)}$ and $\mu = \frac{E}{2(1+\nu)}$.

From Equation 1-1, It can be shown that in plane strain, β=0 if both materials are incompressible ($\nu_1 = \nu_2 = 0.5$) or if both materials have identical elastic constants ($G_1 = G_2$, and $\nu_1 = \nu_2$), then ε=0. The effect of β≠0 on the stress field and fracture toughness is complicate and considered only when necessary in practical cases of material with large difference of elastic constant.

For ε=0

$$\sigma_{22} = \frac{K_I}{\sqrt{2\pi r}}, \sigma_{12} = \frac{K_{II}}{\sqrt{2\pi r}} \tag{1-15}$$

And

$$\delta_2 = \frac{8K_I}{E_*}\sqrt{\frac{r}{2\pi}}, \delta_1 = \frac{8K_{II}}{E_*}\sqrt{\frac{r}{2\pi}} \tag{1-16}$$

From these equations we observe that K_I and K_{II} play the same role as their counterparts in the case of a crack in elastic homogeneous isotropic solid. The mode I component K_I is the amplitude of the singularity of the normal stress ahead the tip and the associated normal separation of the crack flanks, while the mode 2 component K_{II} is the shear stress in the interface and the relative shearing displacement of the flanks.

A relative measure of the amount of shear and normal stress intensity factors at the crack tip can be obtained by the mode mixity angle ψ defined by **[Gdoutos 2005]**

$$\Psi = \tan^{-1}(K_{II} / K_I) \tag{1-17}$$

Another expression relating the stress around the crack tip to polar coordinates r and θ had been introduced by Rice et al. **[Rice 1990]**. Considering only the stresses in the interface plane (θ=0) and eliminating mode Ⅲ loading, the expression can be reduced to:

$$\left(\sigma_{yy} + i\sigma_{yx}\right)_{\vartheta=0} = \frac{Kr^{i\varepsilon}}{\sqrt{2\pi r}} \tag{1-18}$$

K denotes a complex stress intensity factor measuring the singularities of normal and shear stresses normal to the crack front, as mentioned before. Formally, the right side of (1-18) corresponds to the stresses ahead of a crack tip in a homogeneous solid. The stress intensity factors K_1 and K_2 for the interface crack depend on the polar coordinate r; these can be expressed as:

$$\begin{aligned} K_1(r) &= \mathrm{Re}\left(Kr^{i\varepsilon}\right) \\ K_2(r) &= \mathrm{Im}\left(Kr^{i\varepsilon}\right) \end{aligned} \tag{1-19}$$

Re and Im denote the real and the imaginary part of a complex number respectively. The "oscillation index"ε is a bimaterial real constant, which depends on the Dundurs parameter β:

$$\varepsilon = \frac{1}{2\pi}\ln\left(\frac{1+\beta}{1-\beta}\right) \tag{1-4}$$

K has the generic form **[Ernst 1995]**:

$$K = YT\sqrt{L}L^{-i\varepsilon}e^{i\psi} \tag{1-20}$$

The factor *Y* corresponds to the sample geometry. *T* is the load applied on the specimen. *L* is the crack length. *Ψ* represents the "local phase angle" of the stress field at *r*=*L* while *L* is a macroscopic length.

Owing to the identity $r^{i\varepsilon}L^{-i\varepsilon} = e^{i\varepsilon\cdot\ln(r/L)}$, from equation (1-18) and (1-20) we obtain:

$$\frac{\sigma_{yx}}{\sigma_{yy}} = \frac{K_2(r)}{K_1(r)} = \tan(\psi + \varepsilon\ln(r/L)) \tag{1-21}$$

This equation is used in the conditions when mismatch of elastic constants ($\varepsilon \neq 0$) is always present, then the mixed mode depends on the location. The tensile and shear opening modes (mode Ⅰ and Ⅱ) of crack are inseparable. As the r (distance from the crack tip) decreases, the local phase angle ($\Psi+\varepsilon\ln(r/L)$) oscillates more and more rapidly. This means that shear stresses arise at the crack tip even if the external load has no shear component.

2.4. Metal-oxide adhesion

The basic thermodynamic properties of the interface is the free energy per unit area γ. In experimental measurement, a different quantity has been used: the true work of adhesion W_a. The true work of adhesion of the interface is the amount of energy required to create free surfaces from bonded materials under reversible conditions. Considering a hetero-interface between A and B, then the true work of adhesion can be expressed as follows:

$$W_a = \gamma_a + \gamma_b - \gamma \qquad \text{(Dupré equation)} \tag{1-22}$$

where γ_a and γ_b are the surface energies of material A and B respectively. The true work of adhesion is the intrinsic property of the bi-material that depends on the type of bond through the interface and the level of contamination on the initial surface.

The attractive interaction between the material A and B occurs while W_a is greater than zero. The true work of interface is often determined by contact angle measurements. The contact angle is usually measured at annealed metal drops on the substrates or obtained by the sessile liquid drop method. If the tested metal drop is on thermal equilibrium, then from local equilibrium at a triple line of three different phases, we obtain the equation:

$$\gamma = \gamma_a - \gamma_b\cos\theta \tag{1-23}$$

Where θ is the contact angle between the metal drop free surface and the substrate (Figure 1-5). The true work of adhesion now can be expressed with the Young- Dupré equation, which describes W_a as the function of the contact angle θ:

$$W_a = \gamma_a + \gamma_b - \gamma = \gamma_b(1+\cos\theta) \tag{1-24}$$

Thus, W_a can only be determined relative to the surface energy of the metal drop.

For contact angle measured at interfacial pores (Figure 1-6), the local equilibrium can be expressed by the equation:

$$\frac{\gamma}{\sin\theta} = \frac{\gamma_a}{\sin\theta_b} = \frac{\gamma_b}{\sin\theta_a} \tag{1-25}$$

Then inserting into the Dupré Equation:

$$W_a = \gamma_a\left(1 + \frac{\sin\theta_a - \sin\theta_b}{\sin\theta}\right) \tag{1-26}$$

This yields the same result as that of equation (1-23), indicating that W_a can only be determined relative to the surface energy of the metal.

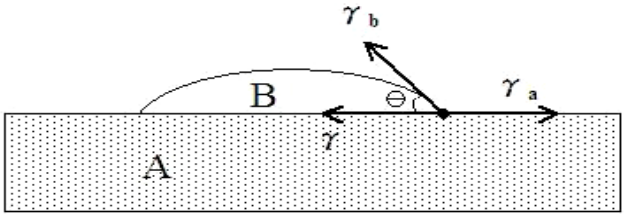

Figure 1-5: Definition of the contact angle at drops.

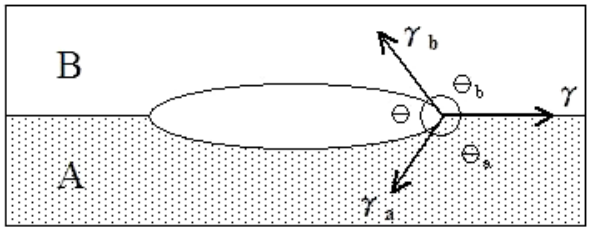

Figure 1-6: Definition of the contact angle at pores.

The practical crack propagation energy G_{ci} is always higher than W_a. This difference, which has been extensively discussed in literature **[Ernst 1995, Sinnott 2003]**, is usually explained by the various contributions of three multiplicative factors:

The first one is the non-equilibrium thermodynamic state of the newly created fracture surfaces, and is estimated between 1 and 10. The second one is the effect of interface roughness, which causes the true contact area to be larger than its projected measurable value. This factor is generally only slightly larger than 1. The third factor is the energy dissipation through confined plastic deformation of materials at the interfacial crack tip. Therefore, the G_{ci} usually exceeds W_a by two or even three orders of magnitude and reach values as high as hundreds of J/m^2 **[Felder 2003]**.

3. Metal-oxide adhesion measurement

The adhesion between metals and oxides has been an area of interest for many years. There are numerous different methods to measure the adhesion of metal/oxide interface. These tests, however, are very specific and often their results are mutually inconsistent. This is because the adhesion is strongly affected by interfacial cleanness, contact surface roughness, the mode of loading and the activity of energy-dissipating processes such as the plasticity in either of the materials. The ideal adhesion test should follow some criteria: quantitative, easy for sample preparation and results relevant to real world. So far, none of the adhesion test technique meets all of the above criteria.

The specimens used to measure metal/oxide adhesion usually have a film attaching to a substrate. Most adhesion measurement methods are designed to fit coating/substrate geometry. They can be divided into two broad categories: destructive or nondestructive. Destructive method always means a loading force is applied to the coating in some specified manner and the resulting damage subsequently observed. Nondestructive methods typically apply a pulse of energy to the interface and then analyze energy losses occurring because of mechanisms operating only at the interface to characterize the adhesion strength between the coating and the substrate.

In this section, we describe in more detail destructive techniques which have been used in literature to measure the adhesion.

3.1. Tape test

This is the traditional method to measure the adhesion. A piece of the adhesive tape is attached to the film and then the tape is pulled off **[Mittal 1976]**. If the tape pulls away the film from the substrate then we can define that the adhesion is poor. Obviously, this method gives only qualitative results and no numerical values. However, it is a simple and fast method to know whether it is a weak adhesion or not. It can be a useful characterization test in certain applications.

3.2. Pin Pull test

In Pin Pull test, a metal pin is glued to a film, which is bonded to the substrate. An increasing force F is applied in the direction normal to the test surface. Then we measure the critical force required to pull off the film from the substrate (Figure 1-7). The direction of applied force and the thickness of the glue influence the results sensitively. The adhesive strength of the pin to the film limits the application of this test **[Steinmann 1989]**.

The adhesion is determined as F/A, where A is the attached area to the pin. It is not practical to assume that the interface fracture occurs across the whole surface of the pin at the same time. It is the reason why the value of the contact area seems questionable.

Yang et al. **[Yang 1997]** described an adhesion test in which normal force is applied to metal films electro-statically. This provides uniform stress distribution and does not need the glue. The fracture stress at which films blistered from the substrate was well described by Weibull statistics.

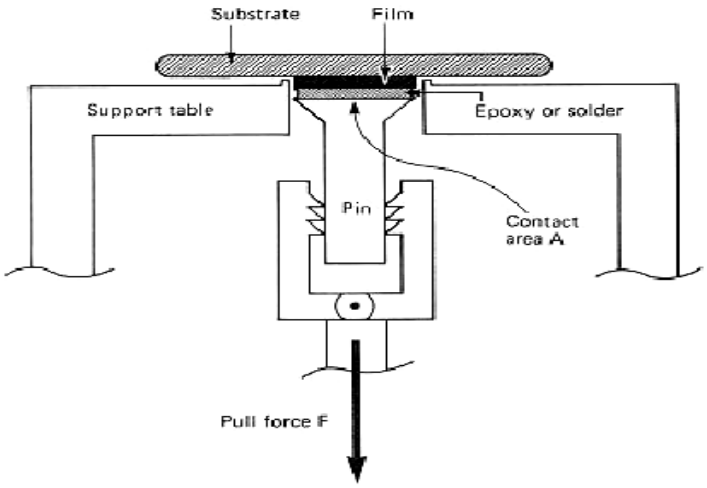

Figure 1-7: The Pin Pull test ***[Yang 1997]***

The main advantage of the pin pull test is its wide ranging applicability to all manner of coatings, from relatively soft flexible polymer coatings to hard brittle coatings such as diamond. Its main disadvantage is the wide variability in typical test data. Multiple tests must be done on a given sample coupled with statistical analysis to obtain reliable quantitative data. **[Lacombe 2006]**

3.3. Peel test

In typical peel test, the peel force P is measured while a tape of film, a few mm wide, is peeled off at slow uniform speed as shown in the Figure 1-8. The film can be pulled directly or with help of an adhesive tape overlayer. The energy release rate is given by **[Maugis 1999]**:

$$G = \frac{P}{b}\left(1-\cos\theta\right)+\frac{P^2}{2b^2Eh} \qquad (1\text{-}27)$$

Where θ is the peel angle, b and h are the width and the thickness of the tape, E is Young's modulus of the film. When tests are performed in the same conditions and in the same speed, the peel test gives repeatable results. The tensile and bending forces in both film and adhesive overlayer usually cause a large amount of plasticity that dissipates much of the energy. This test is also limited by the strength of the film and the adhesion of the tape. Therefore only the systems with relatively poor adhesion can use this test.

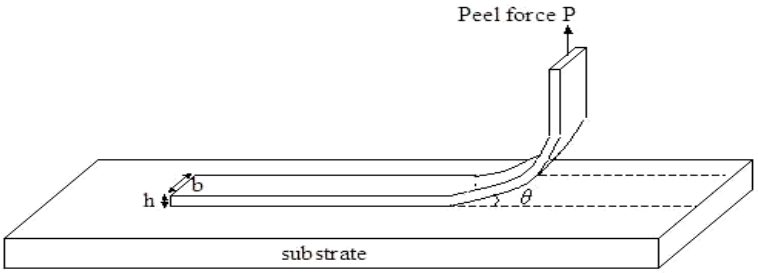

Figure 1-8: The Peel test

The advantage of the peel test is that sample preparation is simple and low-cost. A further advantage is that the rate of delamination can be controlled precisely. The disadvantage of the peel test is that relation between the quantitative value of the peel force and the strength of the coating/substrate interface is strongly dependent on the peel angle and the plastic dissipation during the crack propagation.

3.4. Scratch test

The scratch test uses a smoothly rounded stylus (typically diamond), which is dragged across the surface of the film (Figure 1-9). A vertical load is applied to the stylus and is gradually increased until a critical value is reached. When the critical value is reached, the film begins to strip from the substrate leaving a clear channel **[Lieng 1991].** The stripping of the film can be observed in a microscope, and the critical load is detected through characteristic acoustic emissions. The minimum critical load P_{cr} at which the delamination occurs can be used to measure the practical work of adhesion $W_{A.P}$ **[Volinsky 2002]**:

$$P_{cr} = \frac{\pi r^2}{2}\left(\frac{2EW_{A.P}}{h}\right) \tag{1-28}$$

Where r is the contact radius and h is the thickness of film. This analysis is available only when the compressive load is normal to the film.

It is complicate to analyze the mechanics of the scratch test and to relate the critical load to the film adhesion. Together with the mechanical properties of film and substrate, the scratch elastic stress distribution, the thickness of film, loading rate and stylus sharpness are all needed to calculate the energy of the adhesion.

Although the analysis is complicate, scratch test has several advantages. The sample preparation is relatively easy and there is no intrinsic limit to the force, so that even a tough interface may be debonded.

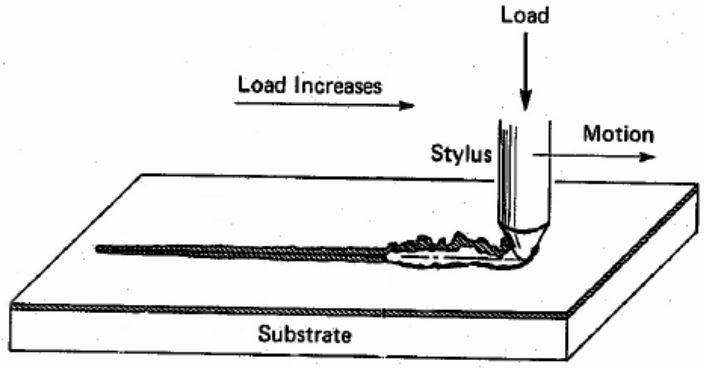

Figure 1-9: The Scratch test ***[Lieng 1991]***

3.5. Beam bending test

There are various beam bending tests; the test samples are always fabricated in the form of a sandwich. That means a thin film is enclosed between two thick beams. Typically the bottom beam is substrate and the top beam is securely adhered to the film. The pre-crack at the interface is indispensable to introduce de-bonding and the bending loads are applied to the beams to provide the driving force for delamination. Here we take the double cantilever beam (DCB) and four-point bending test for examples.

The crack extension force (G) can be analyzed by the linear elastic fracture mechanics:

$$G = \frac{P^2}{2b}\frac{\partial C}{\partial a} \tag{1-29}$$

Where C is the solid compliance, P is the loading applied, b and a denote the width and the length of crack. Both the double cantilever beam and four-point bending test can use this approach.

In the double cantilever beam test, see Figure 1-10, the crack extension force (G) can be expressed as **[Kanninen 1973]**:

$$G = \frac{12P^2 a_0}{EB^2H^3}\left[1 + \frac{AH}{a_0} + B\left(\frac{H}{a_0}\right)^2\right] \tag{1-30}$$

Where a_0 is the pre-crack length, H is the beam thickness, A and B are the proportionality coefficients (A~1.3 and B~0.5) **[Volinsky 2002]**.

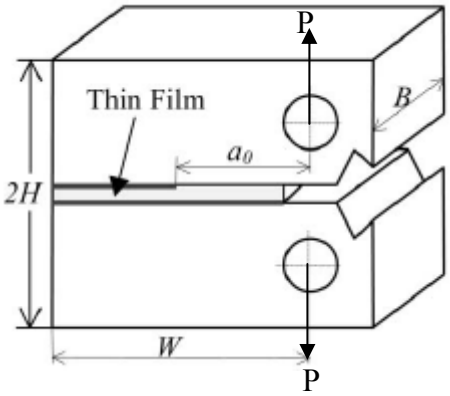

Figure 1-10: The double cantilever beam ***[Volinsky 2002]***

The advantage of this test is that it can provide the interfacial toughness for almost pure mode Ⅰ external loading.

In the four-point test (Figure 1-11), the crack extension force (G) can be expressed as **[Ma 1996]**:

$$G = \frac{21M^2}{4b^2H^3\overline{E}} \tag{1-31}$$

Where M is the bending moment (M=PL/2), $\overline{E}$ is the beam plane strain modulus, $\overline{E}$ = E/(1-ν^2) for an isotropic material. The advantage of four-point bending test is that G is independent of the interface crack length.

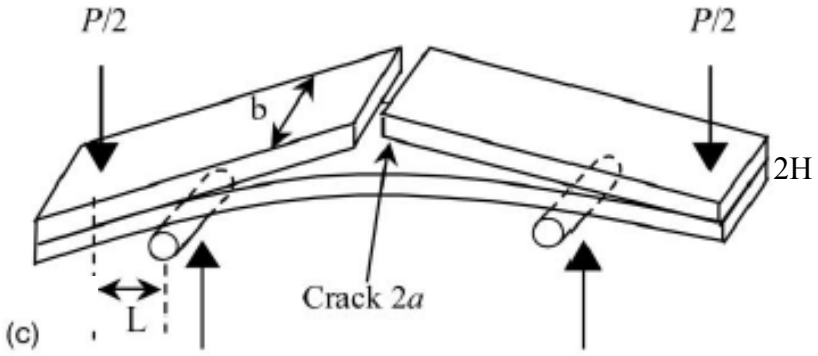

Figure 1-11: The Four-point bending geometry ***[Volinsky 2002]***

The disadvantage of the beam-bending test is the difficulty to prepare the samples. Typically, the sample preparation uses the diffusion bonding or gluing. The bonding process takes a long time and occurs at the temperature near the melting point, which is like an annealing process and may influence the interface properties.

3.6. Indentation test

Indentation test is performed with an indenter, a small conical pointed tip, which is pressed vertically into the thin film with a known force. In the case of a weakly bonded film, the film will separate from the substrate when the stress applied exceeds the bonding strength between the film and the substrate, see Figure 1-12. Marshall et al **[Marshall 1984]** provided the analysis for the conical indentation test, the strain energy release rate is:

$$\frac{GE_f}{(1-\nu_f)} = \frac{1}{2}h\sigma_1^2(1+\nu_f) + (1-\alpha)(h\sigma_R^2) - (1-\alpha)h(\sigma_1 - \sigma_B)^2 \qquad (1\text{-}32)$$

Where E_f and ν_f are film's Young's modulus and Poisson ratio, h is the film thickness, σ_B is the buckling stress for a clamped circular, σ_1 is the stress applied to the edge of the plate, α=0.383 for $\nu = 1/3$ and σ_R is the residual stress in the film. The difficulty in analyzing the indentation test is that both the elastic and the plastic deformation field are produced by indentation.

The indentation test has some advantages such as: applicable to a wide variety of coating/substrate systems, easy for sample preparation, quantitative results obtained and commercial equipment available (nanoindentation). There are two main disadvantages: complex mode of loading involving large compressive stress and high shear strain and difficult quantitative analysis and poorly understood precise mechanism of delamination **[Lacombe 2006]**.

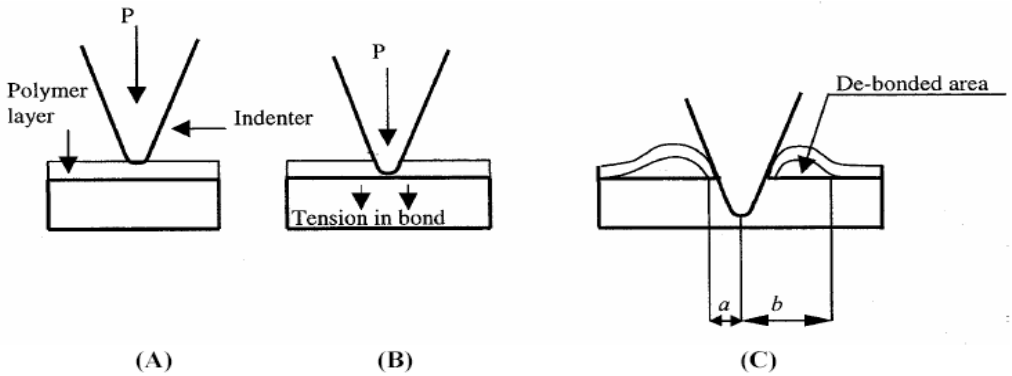

Figure 1-12: The procedure of indentation test ***[Sura 1990].***

3.7. Laser spallation technique

The laser spallation technique is developed to measure the intrinsic strength of interfaces. This technique involves impinging a high-energy laser pulse, with duration of a few nanoseconds, on the rear surface of the substrate, which is coated with a thin film of absorbing material **[Youtsos 1999]** (Figure 1-13). The absorbing film absorbs the laser pulse that causes rapid thermal expansion, which induces a compressive shock wave emission through the substrate towards the film-substrate interface. The free film surface reflects the shock wave that gives a tensile wave leading to the film removal if

the incident laser pulse has enough energy. The results acquired by the experiment match the predictions of mathematical simulation, both of which show that de-bonding occurs rapidly therefore the separation through crack growth cannot occur. Thus the atomic bond rupture is the major mechanism of separation in this technique. Laser spallation test may be the only effective method for analyzing refractory brittle systems like diamond-on-alumina specimens. The same properties which give the laser spallation test unique advantage also bring its most important disadvantages. This method needs expensive equipment that is not readily available. The need for special backing and absorbing layers also limit the usage of the method.

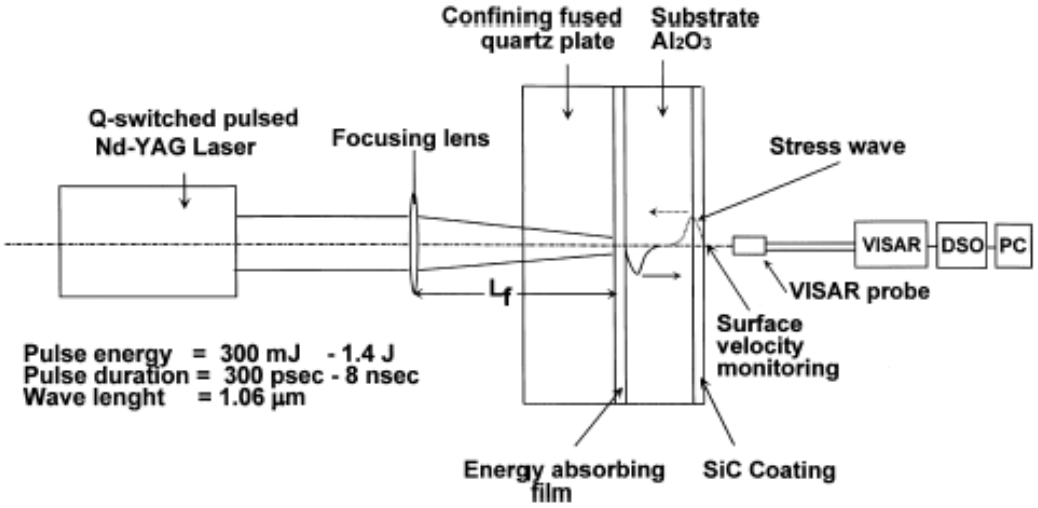

Figure 1-13: Schematic of laser spallation experiment ***[Youtsos 1999]***

3.8. Telephone cord delamination method

Telephone cord delaminations are typically found in thin-film/substrate systems with weak interfaces and very high compressive stresses in the films. The delamination is created when the film buckles from the interface to relieve strain energy in the film. The delamination will form some blisters. Once these blisters form, the interface fracture energy can be calculated by measuring the dimensions of the blister and using the models of the mechanics of telephone cord blister. **[Lee 2005]**. Figure 1-14 illustrates the topology of the telephone cord buckling of compressed diamond-like carbon on glass substrates which have been characterized with atomic force microscopy (AFM) and with the focused ion beam (FIB) imaging system **[Moon 2002]**.

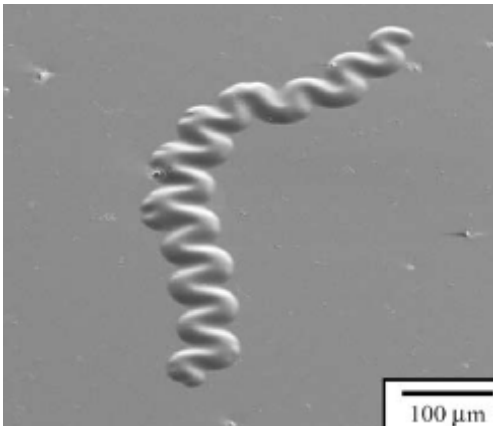

Figure 1-14: illustration of telephone cord buckles ***[Moon 2002]****.*

3.9. Interface indentation test

Recently, some authors have proposed to use indentation tests to measure interface adhesion. Vickers indentation tests are used to generate and propagate a crack in the interface plane. The generated cracks have a semi-circular shape. Starting from critical load and length of cracks, it is possible to represent adhesion in terms of interfacial toughness **[Lesage 2001]**. The advantage of the test is that equipment is simple. The disadvantage is that to obtain quantitative results is difficult, because the length of crack can't be determined precisely.

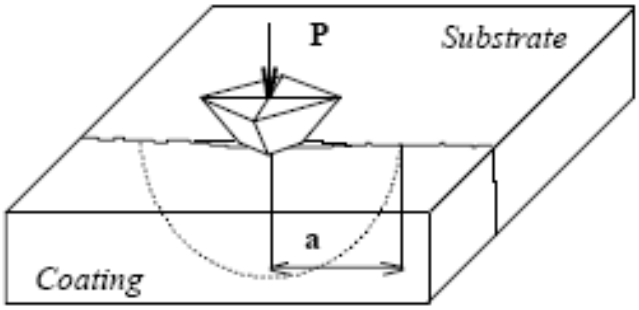

Figure 1-15: Principle of the interface indentation test ***[Lesage 2001]****.*

3.10. Cross-sectional nanoindentation test

Sanchez et al. proposed this new mechanical test (Cross-sectional nanoindentation (CSN) test) especially designed for measuring the fracture toughness of thin film/brittle substrate interfaces. Interfacial fracture is achieved by nanoindentation in the substrate cross-section. A model based on the elastic plate theory has been developed to calculate numerically the interfacial critical energy release rate (G_{ci}) for ceramic/ceramic systems from CSN test results. From the thin film elastic properties, thin film thickness, interfacial crack area and maximum thin film deflection during the test, the interfacial

critical energy release rate can be calculated **[Sanchez 1999]**.

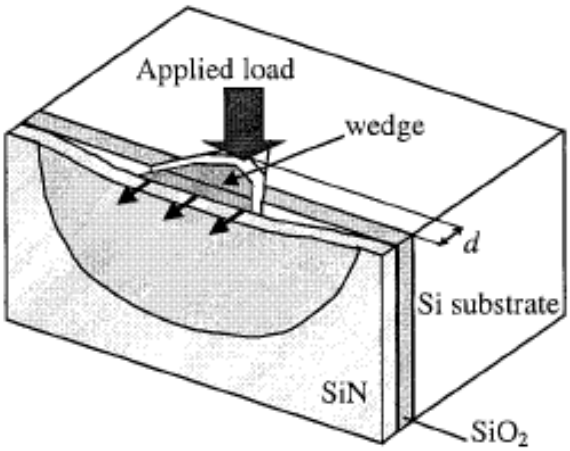

*Figure 1-16: Principle of the Cross-sectional nanoindentation test **[Sanchez 1999]**.*

3.11. Blister test

In the blister test, the biaxial film tension is analogous to the uniaxial tension in bulk materials. Uniform pressure is applied to one side of a freestanding film window, causing film to deflect outwards. We can determine the stress and strain of the film from the measurements of pressure (P) and deflection (h). The pressure applied to the film is augmented until the film begins to de-bond from the substrate. A circular blister will be formed and grows steadily (Figure 1-17) if the pressurizing fluid is incompressible. The purpose of the blister test is to determine the critical strain energy release rate of the interface **[Dannenberg 1961]**. Fully quantitative results and analysis based on fracture mechanics method can be obtained from the blister test. The main disadvantage is the difficulty in sample preparation.

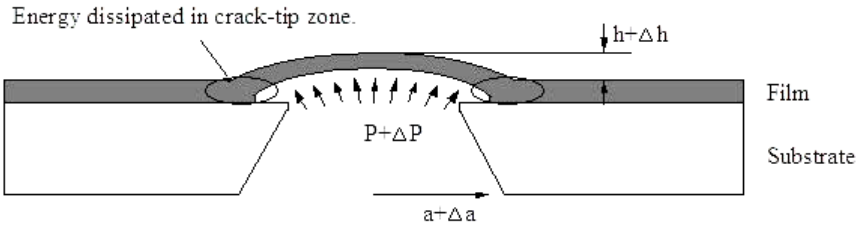

Figure 1-17: The blister test.

4. Conclusions

Metal-oxide interface plays an important role in many applications. Determination of metal-oxide adhesive properties is one of the most important problems for the use of these applications. Numerous studies are presented to measure the metal-oxide adhesion, all methods have to face plenty of experimental difficulties.

The interface indentation test, cross-sectional indentation test and blister test are the techniques used in the present study. The blister technique does provide a repeatable and quantitative method to determine the mechanical properties of film and the critical crack extension force of the film/substrate interface (G_c). To compare the blister test with other test method, the cross-sectional indentation test is used and developed. There are more detailed descriptions about those tests in the further chapters.

References

[Dannenberg 1961] H. Dannenberg, "*Measurement of adhesion by a blister method*" Journal of Applied Polymer Science, 5(14), (1961) pp.125-134.

[Dundurs 1969] J. J. Dundurs, "*Elastic Interaction of Dislocations with Inhomogeneities*" Mathematical Theory of Dislocation, (1969) pp.70-115.

[Ernst 1995] F. Ernst., "*Metal-oxide interface*" Materials Science and Engineering R14, No 3, (1995) pp.97-156.

[Evans 1988] A. G. Evans and B. J. Dalgleish, "*The edge cracking and spalling of brittle plates*" Acta Metallurgica et Materialia, Vol.35, No 6. (1988) pp.1333-1341.

[Evans 1993] A. G. Evans and B. J. Dalgleish, "*The fracture resistance of metal-ceramic interfaces*" Materials Science and Engineering A, 162, (1993) pp.1-13.

[Felder 2003] E. Felder, E. Darque-Ceretti, Adhésion et Adhérence, CNRS Edt, Paris, (2003).

[Gdoutos 2005] E. E. Gdoutos, *Fracture Mechanics: An Introduction* (2005), ISBN 1-4020-2863-6.

[Garrison 1980] W. M. Garrison, Jr. and N.R. Moody, "*Ductile Fracture*" Journal of the Physics and Chemistry of solids, Vol. 14, (1980) pp.1035-1074.

[Kanninen 1973] M. F. Kanninen, "*An augmented double cantilever beam model for studying crack propagation and arrest*" International Journal of Fracture, 9 (1973) pp.83-92.

[Knott 1977] J. F. Knott, "*Micromechanisms of Fracture and the Fracture Toughness of Engineering Alloys*" Fracture, Vol 1, ICF4, (1977) pp. 61-91.

[Lacombe 2006] R. Lacombe, *Adhesion measurement methods: Theory and practice* (2006), ISBN 0-8247-5361-5.

[Lee 2005] A. Lee, C. S. Litteken, R.H. Dauskardt, W.D. Nix, "*Comparison of the telephone cord delamination method for measuring interfacial adhesion with the four-point bending method*" Acta Materialia, 53 (2005) pp.609-616.

[Lesage 2001] J. Lesage, D. Chicot. "*Hardness and adhesion of coatings*" Revista de la Facultad de Ingeniería de la U.C.V., Vol. 16, Nº 1, (2001) pp.33 – 38.

[Lieng 1991] H. L. Lieng , *Fundamentals of adhesion* Plenum Press, New York. (1991) ISBN 0-306-43470-9.

[Ma 1996] Q. Ma,"*A four-point bending technique for studying subcritical crack growth in thin films and at interfaces*" Journal of Material Research, 12 (1996) pp.840-845.

[Maugis 1999] D. Maugis. *Contact, Adhesion and Rupture of Elastic Solids* (1999) ISBN 3-540-66113-1.

[Marshall 1984] D. B. Marshall, A. G. Evans, C. Rossington ,"*Measurement of adherence of residually stress thin films by indentation. Ⅱ. Experiments with ZnO/Si*" Journal of Applied Physics, 56 (1984) pp.2639-2644.

[Mittal 1976] K. L. Mittal, "*Adhesion measurement of thin films*" Electrocomponent Science and Technology, 3, (1976) pp.21-42.

[Moon 2002] M. W. Moon, H. M. Jensen, J. W. Hutchinson, K. H. Oh, A. G. Evans. "*The characterization of telephone cord buckling of compressed thin films on substrates*" Journal of the Mechanics and Physics of Solids, 50 (2002) pp.2355-2377.

[Rice 1990] J. Rice, Z. Suo, and J. S. Wang, in M. Rühle, A. G. Evans, M. F. Ashby and J. P. Hirth (eds.), *Metal-Ceramic Interfaces*, Acta-Scripta Materialia Proc. Ser., Pergamon, Oxford, Vol. 4, (1990) pp. 269.

[Sanchez 1999] J. M. Sanchez, S. El-Mansy, B. Sun, T. Scherban, N. Fang, D. Pantuso, W. Ford, M. R. Elizalde, J. M. Martinez-Esnaola, A. Martin-Meizoso, J. Gil-Sevillano, M. Fuentes and J. Maiz. "*Cross-sectional nanoindentation: a new technique for thin film interfacial adhesion characterization*" Acta Materialia, 47, (1999) pp.4405-4413.

[Sinnott 2003] S. B. Sinnott, E. C. Dickey., "*Ceramic/metal interface structures and their relationship to atomic- and meso-scale properties*" Materials Science and Engineering R, 43, (2003) pp.1-59.

[Steinmann 1989] P. A. Steinmann, H. E. Hintermann,"*A review of the mechanical tests of for assessment of thin-film adhesion*" Journal of Vacuum Science and Technology, A7 (3), (1989) pp.2267-2272.

[Sura 1990] V. M. Sura, "*Indentation test for adhesion measurement of polyamide films*" Journal of Adhesion Science and Technology, v4 n3 (1990) pp.161.

[Volinsky 2002] A. A.Volinsky, N. R. Moody, W. W. Gerberich. "*Interfacial toughness measurement for thin films on substrate*" Acta Materialia, 50 (2002) pp.441-466.

[Wilsforf 1983] H. G. F. Wilsforf, "*The Ductile Fracture of Metals: a Microstructural Viewpoint*" Materials Science and Engineering, Vol 59, (1983) pp.1-19.

[Yang 1997] H. S.Yang, F. R. Brotzen, D. L. Callahan et al,"*Electrostatic adhesion testing for the evaluation of metallization adhesion*" Materials Research Society Symo. Proc.473, (1997) pp.63-68.

[Youtsos 1999] A. G. Youtsos, M. Kiriakopoulos, Th. Timke. "*Experimental and theoretical/numerical investigations of thin films bonding strength*" Theoretical and Applied Fracture Mechanics, 31 (1999) pp.47-59.

Chapter II

Interface Adhesion Measurement by Blister Test

1. Introduction 29
2. Development of the blister test 30
3. Mechanical analysis 32
   3.1. Nomenclature 32
   3.2. Criterion for debonding 33
   3.3. Crack extension force 34
   3.4. Near edge loads 45
   3.5. Mode mixity in blister test 47
   3.6. Correction for plastic work 48
4. Conclusions 50
References 51

1. Introduction

The bulge test and blister test are closely related techniques for measuring the mechanical properties and adhesion of films. In the bulge and blister test, a free-standing window of a membrane is bonded to a substrate and is pressurized by pumping fluid into the cavity below the film. For bulge test, a free-standing window is pressurized without debonding the film from the substrate (Figure 2-1 (a)). The applied pressure and resulting film deflection of the window are related to the residual stress and biaxial modulus of the film. As pressure increases, the film will debond from the substrate, forming a circular blister (Figure 2-1 (b)).then, if the pressurizing fluid is incompressible and its injected volume is regulated, the resulting pressure will decrease because of the large volume increment of the blister, and the interfacial crack will grow stably with the fluid injection rate. The crack extension force Gc can be determined from the applied pressure and film deflection of the window, either at the critical point for the first debonding, or along the pressure decreasing variation driving the blister growth.

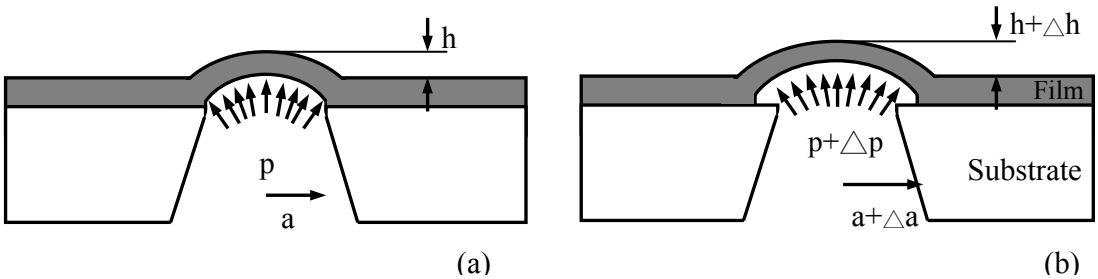

Figure 2-1: Cross-sectional view of the bulge test (a) and the blister test (b).

Figure 2-2 shows a schematic diagram of pressure vs. height data of the bulge and blister test. The square points denote the real experimental results. At first, pressure is too low to induce debonding, and the window simply stretches and deflects upward according to the bulge equation (Bulge test). There is a transition region in which either debonding has initiated but the blister is growing unstably or is poorly behaved (full square dots), or debonding initiation is difficult and needs over-critical loading (open square dots). Once the blister has assumed a circular shape and grows steadily, the blister behaves according to the blister equation (Blister test).

Blister tests are often invalid in the case of ductile films due to film yielding before debonding. Another problem with blister test occurs when the crack does not propagate uniformly along the perimeter of the blister, which makes it difficult to explain the results **[Volinsky 2002]**. Although the blister test has some defects, it seems to be a relatively precise method to determine the amount of energy required to debond the film from its substrate; this quantity characterizes the film adhesion.

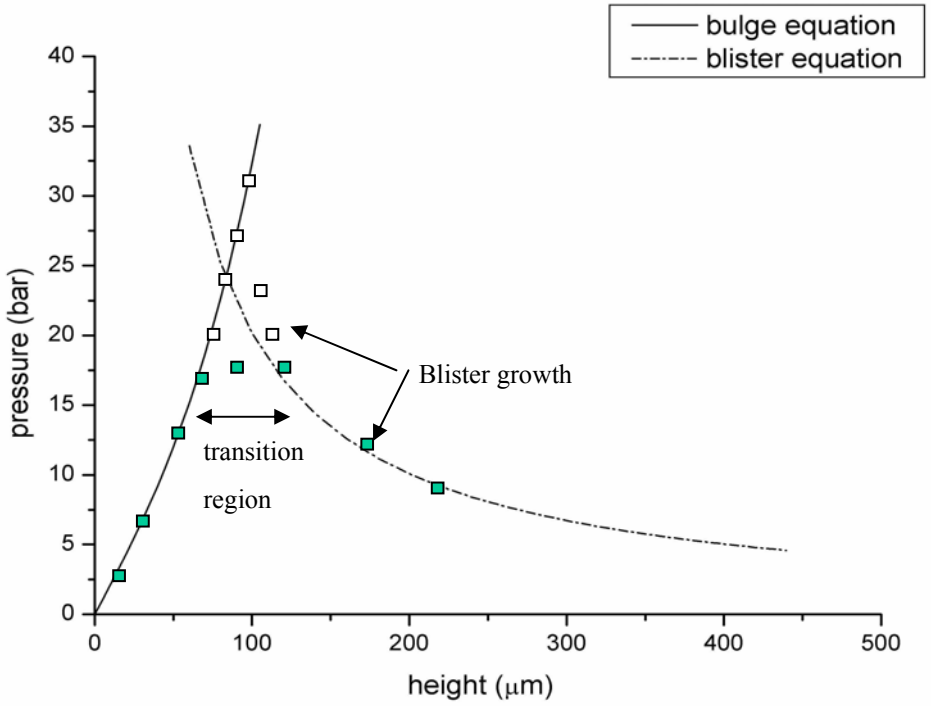

Figure 2-2: Schematic of the data of the bulge and blister test. The square points denote the real experimental results

2. Development of the blister test

For the theoretical modeling development, Dannenberg **[Dannenberg 1961]** was the first to apply this technique to measure adhesion strength of polymer coating. The most noteworthy theoretical modeling analyses of the blister test were carried out by Williams (1969), Bennett *et al*. (1974), Storakers and Andersson (1988). They used the framework of classical fracture mechanics, in these works; the effects of loading and nonlinearity caused by large blister deformations on the energy release rate were investigated.

Jensen **[Jensen 1990]** analyzed the mode mixity of interface fracture mechanics in the blister test for residual stress-free films. He found that the phase angle of loading at the interface crack tip changed significantly during the blister deformation, the mode mixity parameter (Ψ) is typically in the range of -35^o to -60^o.

Allen and Senturia (1988) developed an island blister test; the center of pressurized window is cohered to a central "island", and the debonding proceeds only to the central island (Figure 2-3). The advantage of island blister test is that the crack extension force can be attained at a given pressure. One problem of the island blister test is that it tends to be unstable.

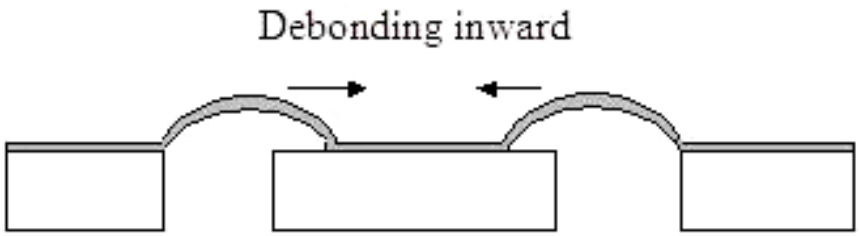

Figure 2-3: Island blister test.

Dillard *et al*. (1991) developed the constrained blister test that decreases the mean film stress while a particular energy release rate G is attained. In this technique a rigid plate fixed over the window and parallel to the substrate forbids the film deflecting beyond a certain distance; the plate supports plenty of the load applied to the film and reduces film mean stress (Figure 2-4).

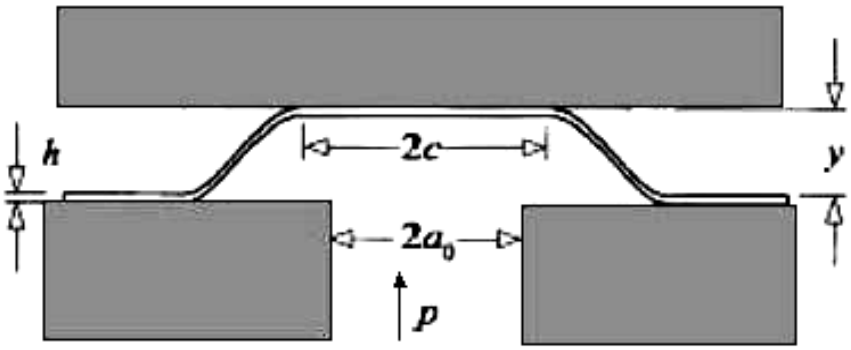

Figure 2-4: Constrained blister test.

Wan **[Wan 2000]** tried to change the constrained blister test. A blind hole is drilled in a substrate then a film is attached to the substrate, so that a fixed amount of gas is trapped in the hole. A plane probe of Thermo-Mechanical Analysis (TMA) meter with a minimum contact load touches the film. When temperature increases the gas pressure increases too, that causes blister to begin and the blister height is recorded by TMA. Arjun and Wan **[Arjun 2005, Wan 1998]** derived the strain energy release rate from first principles for pressured blister test; they showed how energy release rate depends on the loading history. Recently, finite element analysis was used to compare with the present models **[Hbaieb 2005, Guo 2005]**. The report indicated that if bending or bending-to-stretching transition behavior is significant during debonding process, the residual stress must be taken into account to measure the adhesion energy.

For the experimental development, the blister test as a standard test for measuring adhesive strength of thin coating was suggested first by Dannenberg **[Dannenberg 1961]**. Dannenberg used his "blister adherometer", with a machined plate to constrain the blister to grow to an oblong shape, to measure the adhesive strength between thick epoxy resin film and stainless steel substrate, studying the effects of various substrate cleaning process and film thickness on the adhesive strength. The energies were computed directly from the pressure vs. volume data ($G=P_c\triangle V$). Dannenberg recognized that a reinforcing overlayer added onto a film would make it more likely to debond from its substrate before rupturing.

Blister test has been widely applied to determine the adhesion of relatively thick polymer films. Hinkly (1983) studied adhesion of polystyrene thin films to silica substrates. Hinkly observed that the energy required to debond the films was affected by the interaction between the pressurizing fluid and the interface. Gent and Lewandowski (1987) tested the adhesion of thick polymer adhesive tapes to glass. The critical crack extension force (G_c) measured was in the range of 20-150 J/m^2; this may be due to the effect of time-dependent deformation on energy dissipation.

Allen *et al*. (1988) discussed the limitation of blister test and presented another feature (island blister) for adhesion measurements. Briscoe and Panesar (1991) used the blister test to study adhesion of polyurethanes to steel substrates; in 1994 Briscoe also studied the interfacial adhesion of polyurethanes to aluminums.

Presently, blister test is mostly used to determine the adhesion of polymer films **[Wang 1999, Taheri 2000]**. Some authors **[Dupeux 1998, Lee 2006, Zhou 2003, Mougin 2002, Mougin 2003]** tried to use Blister test to determine the adhesion strength of metal/ceramic interface. Due to the difficulty of the sample preparation, blister test is not widely used to obtain interfacial energy release rate between metal and ceramic interface.

3. Mechanical analysis

3.1. Nomenclature

This section discusses the mechanical response of a pressurized membrane and its debonding behaviour. The following variables are used:

Table 2-1: List of variables.

c_1, c_2, c_3	Dimensionless coefficients in bulge equation
c_v	Dimensionless coefficient describing the volume underneath a window
E	Young's modulus

G	Energy release rate
h	Height of deflection (vertical displacement at window center)
M	M=E/(1-ν), phase stress biaxial modulus
t	Thickness of film
R	Film radius of curvature
a	Blister window's radius
p	Pressure
$w(r)$	Vertical displacement of window
$u(r)$	Radial displacement of a point of the window
σ_0	Residual stress
ε_0	Residual strain (=σ_0/M)
ν	Poisson's ratio
σ_T, ε_T	Film stress, strain in transverse direction
σ_l, ε_l	Film stress, strain in radial direction
σ_Ψ	hoop direction stress

3.2.Criterion for debonding

For the blister test, we can assume that the energy changes when the film debonds around the edge of the window. That will increase the window's radius by a tiny increment *da* (Figure 2-5). The increment *da* may be produced by an increment of the injected fluid volume (*dV*). The radius increment causes both the stress in the film and the total area of strained film to increase so the total strain energy of the film also increases ($dU_{strain}>0$). While the corresponding fluid energy ($W_{fluid}=PdV$) is larger than the increase of the film's strain energy, the difference between these two quantities is termed as the energy release rate (G (J/m^2)).

The energy release rate represents the amount of energy available to remove the film from the substrate. For a circular blister, G is given by:

$$G = \frac{1}{2\pi a}\left(\frac{\partial W_{fluid}}{\partial a} - \frac{\partial U_{strain}}{\partial a}\right) \tag{2-1}$$

where $2\pi a$ is the circumference of the circular blister.

If G is equal or greater than the energy required per unit area to separate the film from the substrate, then crack growth could occur thanks to this energies, termed the critical crack extension force (Gc). Gc includes the chemical bonding energy of the interface and energy dissipated during crack propagation by processes such as plastic flow near the crack tip.

Therefore, the film will debond if:

$$G \geq G_c \Rightarrow$$
$$G_c \leq \frac{1}{2\pi a}\left(\frac{\partial W_{fluid}}{\partial a} - \frac{\partial U_{strain}}{\partial a}\right) \tag{2-2}$$

The purpose of the blister test is to measure the critical crack extension force (*Gc*).

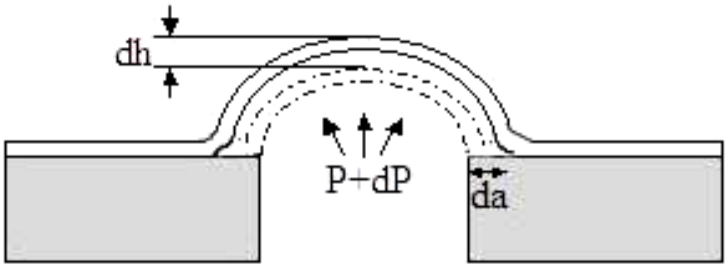

Figure 2-5: Schematic of blister growth

3.3.Crack extension force

At beginning, we assume that the film is perfectly elastic. We use the bulge equation to relate the pressure applied to a window to window's height **[Lee 2003]**:

$$p(h) = c_1 \frac{\sigma_0 t h}{a^2} + c_2 \frac{E t h^3}{a^4} + c_3 \frac{E t^3 h}{a^4} \tag{2-3}$$

Then a volume equation is needed to relate the volume underneath a window to its radius and height:

$$V = c_v a^2 h \tag{2-4}$$

where c_v is a constant.

The strain energy of the pressurized film is the amount of work required to inflate the film from an initially flat state to some final height:

$$U_{strain} = \int_0^h p(h) dV \tag{2-5}$$

The work done on the film by the applied pressure while the blister expands is:

$$\frac{\partial W_{ext}}{\partial a} = \frac{\partial (pV)}{\partial a} \tag{2-6}$$

Inserting (2-5) and (2-6) into (2-2) one arrives at an expression for the energy release rate (*G*). Some solutions reported in literature are described as below:

J. G. Williams.

Williams **[Williams 1997]** assumed that axisymmetric membranes are used in blister test and occur in coating failures. For pressure loading, the radial stress σ_l and hoop direction stress σ_ψ (Figure 2-6) are

$$\sigma_l = \left(\frac{p}{2h}\right)\frac{r}{\psi} \quad \text{and} \quad \sigma_\psi = \frac{d}{dr}(r\sigma_l). \tag{2-7}$$

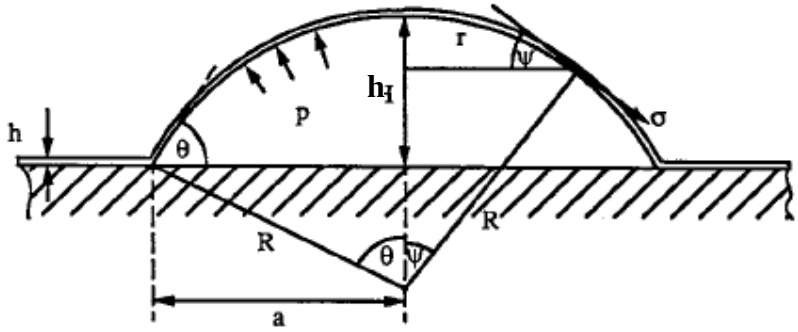

Figure 2-6: The cross-sectional view of blister test ***[Williams 1997]****.*

The strains are

$$\varepsilon_l = \frac{du}{dr} + \frac{\psi^2}{2}, \quad \varepsilon_\psi = \frac{u}{r}. \tag{2-8}$$

Using Hooke's Law, we can obtain

$$E\varepsilon_l = \sigma_l - \nu\sigma_\psi, \quad E\varepsilon_\psi = \sigma_\psi - \nu\sigma_l. \tag{2-9}$$

If residual strains are present in the membrane, they have to be included in ε_l and ε_ψ, in addition to expression (2-8). These six equations above (2-7, 2-8, 2-9) may be expressed as a differential equation

$$\sigma_l^2 \cdot \frac{d}{dr}(r^3 \cdot \frac{d\sigma_l}{dr}) = -(\frac{Ep^2}{8h^2}) \cdot r^3 \tag{2-10}$$

This non-linear equation can be solved as a series solution. It can be expressed in terms of non-dimensional variables

$$\varsigma = \frac{r}{a} \quad \text{and} \quad f = \left(\frac{Ep^2 a^2}{64 t^2} \right)^{-(1/3)} \cdot \sigma_l \tag{2-11}$$

The boundary conditions of zero slope and $\varsigma = 1$ yield the equation

$$f = A_0 (1 - A_0^{-3} \varsigma^2 - \frac{2}{3} A_0^{-6} \varsigma^4 - \frac{13}{18} A_0^{-9} \varsigma^6 - .....) . \tag{2-12}$$

Numerical solutions giving values of A_0 are shown in Table 2-2 **[Williams 1997]**.

Table 2-2: Numerical solutions of A_0

ν	0.3	0.35	0.4	0.45	0.5
A_0	1.724	1.749	1.777	1.808	1.845

Various approximations are used to express the energy release rate as a function of the strain energy u_s stored in the deformed membrane. V is the volume of the blister with radius a. The energy release rate G is given by

$$G = \frac{-dU_s}{2\pi a da} \Big| V const \tag{2-13}$$

On substituting for V and differentiation

$$G = \frac{5}{4} \frac{pV}{\pi a^2} \tag{2-14}$$

The deflection is given by

$$h = a \int_0^1 \psi \varsigma \cdot d\varsigma = 2 \left(\frac{pa^4}{Eh} \right)^{1/3} \cdot \int_0^1 f^{-1} \cdot \varsigma \cdot d\varsigma \tag{2-15}$$

Hence

$$\frac{V}{h} = \pi a^2 \cdot \frac{\int_0^1 f^{-1} \cdot \varsigma^3 d\varsigma}{\int_0^1 f^{-1} \cdot \varsigma \cdot d\varsigma} \tag{2-16}$$

The expression of G becomes

$$\frac{G}{ph} = \frac{5}{4}\frac{\int_0^1 f^{-1}\cdot\varsigma^3 d\varsigma}{\int_0^1 f^{-1}\cdot\varsigma\cdot d\varsigma} \tag{2-17}$$

For any constant value of f

$$\frac{G}{ph} = \frac{5}{4}\frac{\int_0^1 \varsigma^3 d\varsigma}{\int_0^1 \varsigma\cdot d\varsigma} = \frac{5}{8} = 0.625 \tag{2-18}$$

The inextensible case can be derived from a simple model; constant stress and a spherical shape are assumed. Then

$$G = \frac{p}{2\pi a}\cdot\frac{dV}{da} \tag{2-19}$$

The volume V is

$$V = \frac{1}{3}\pi R^3(2-3\cos\theta+\cos^2\theta) \tag{2-20}$$

And the area A is

$$dA = 2\pi a da \quad \text{and} \quad A = 2\pi R^2(1-\cos\theta)\,. \tag{2-21}$$

Proceeding as in the two dimensional case we have

$$G = \frac{pR}{2}(1-\cos\theta) = \frac{1}{2}ph\,, \text{ so } \frac{G}{ph} = \frac{1}{2} \tag{2-22}$$

Gent and Lewandowski

Gent **[Gent 1987]** assumed an energy criterion for debonding, which is that energy ΔW supplied to the system as the circular debond increases in radius by small amount Δa is equated to the sum of energy expended in the debonding process ΔW_1 and elastic energy changes in the membrane ΔW_2.

$$\Delta W = \Delta W_1 + \Delta W_2 \tag{2-23}$$

Where the input energy $\Delta W = p\Delta V$.

ΔW_1 denotes energy expended in debonding

$$\Delta W_1 = 2\pi \cdot a \cdot G_c \cdot \Delta a \tag{2-24}$$

The relation between pressure and film deflection is

$$p(h) = c\frac{Eth^3}{a^4} \quad \text{(c=1.5625 for v=0.3, c=1.748 for v=0.5)} \tag{2-25}$$

and the volume V is

$$V = c_v a^2 h .$$

i.e.

$$c_v\text{=0.5,}\quad h = c_2\left(\frac{pa^4}{Et}\right)^{1/3},\ \text{so}\ \ V = c_v a^2 c_2\left(\frac{pa^4}{Et}\right)^{1/3} \tag{2-26}$$

Input energy ΔW is given by

$$\Delta W \equiv p\left(\frac{\partial V}{\partial a}\right)_p \Delta a = \left(\frac{10pV}{3a}\right)\Delta a \tag{2-27}$$

The amount of elastic energy stored in the inflated membrane is obtained from equations. 2-4 and 2-23 as

$$W_2 = \frac{pV}{4} \tag{2-28}$$

Thus, the radius of the blister increases by an amount Δa, the energy term W_2 changes by an amount

$$\Delta W_2 = p\left(\frac{\partial V}{\partial a}\right)_p \frac{\Delta a}{4} = \frac{\Delta W}{4} \tag{2-29}$$

On substituting from eqs. (2-24), (2-27) and (2-29) in eq. (2-23), the energy release rate *Gc* is obtained as

$$G_c = 0.649ph$$

Hohlfelder and Vlassak

Hohlfelder **[Hohlfelder 1998, 1995, 1996, 1997. Sizemore 1995]** established that the deflection of a pressurized thin window is well-approximated by two dominating terms (Bulge equation)

$$p(h) = c_1 \frac{\sigma_0 t h}{a^2} + c_2 \frac{E t h^3}{a^4} = k_1 \frac{h}{a^2} + k_2 \frac{h^3}{a^4} \tag{2-30}$$

Where k_1 and k_2 are constant, the volume V is the same as mentioned before

$$V = c_v a^2 h$$

Note that the equation (2-30) can be written as

$$h \cdot p(h) = k_1 \left(\frac{h}{a}\right)^2 + k_2 \left(\frac{h}{a}\right)^4 \tag{2-31}$$

Then it is necessary to calculate the energy change that occurs when the radius of a circular blister increases by a differential amount. The strain energy of the pressurized film is the amount of work required to bend the film from the initial flat state to certain height

$$U_{strain} = \int_{h'=0}^{h'=h} p(h')dV = \int_{h'=0}^{h'=h} p(h')\left(\frac{dV}{dh'}\right)dh' = \frac{1}{2} c_v k_1 h^2 + \frac{1}{4} \frac{c_v k_2 h^4}{a^2}$$

$$U_{strain} = \frac{1}{4} c_v k_1 h^2 + \frac{1}{4} pV \tag{2-32}$$

At constant pressure, the derivative of strain energy with respect to blister radius is

$$\left(\frac{\partial U_{strain}}{\partial a}\right)_p = \frac{h c_v \left(\frac{h}{a}\right)\left(4k_1^2 + 11 k_1 k_2 \left(\frac{h}{a}\right)^2 + 5k_2^2 \left(\frac{h}{a}\right)^4\right)}{2\left(k_1 + 3k_2 \left(\frac{h}{a}\right)^2\right)} \tag{2-33}$$

The work done by the applied pressure on the film window while the blister expands is

$$\left(\frac{\partial W_{ext}}{\partial a}\right)_p = \left(\frac{\partial pV}{\partial a}\right)_p = p\left(\frac{\partial V}{\partial a}\right)_p$$

$$\left(\frac{\partial W_{ext}}{\partial a}\right)_p = \frac{2hc_v\left(\frac{h}{a}\right)\left(k_1 + k_2\left(\frac{h}{a}\right)^2\right)\left(2k_1 + 5k_2^2\left(\frac{h}{a}\right)^2\right)}{k_1 + 3k_2\left(\frac{h}{a}\right)^2} \tag{2-34}$$

Inserting equations (2-33) and (2-34) into (2-2), the expression for the energy release rate can be written as

$$G = \frac{4k_1 + 5k_2\left(\frac{h}{a}\right)^2}{4\left(k_1 + k_2\left(\frac{h}{a}\right)^2\right)}\frac{c_v}{\pi}ph \tag{2-35}$$

A new variable is introduced

$$\phi = \frac{k_1}{k_2}\left(\frac{h}{a}\right)^2$$

Equation (2-35) can be rewritten, so-called “blister equation”, as

$$G = g(\phi)\frac{c_v}{\pi}ph \qquad g(\phi) = \left(\frac{4+5\phi}{4+4\phi}\right) \tag{2-36}$$

The factor $g(\phi)$ in (2-36) approaches limiting values in the residual stress dominated regime and modulus dominated regime. In the conditions of high residual stress or small displacements

$$\text{As } \phi \to 0,\ G \to 1.00\frac{c_v}{\pi}ph$$

In the modulus dominated regime, occurring at low residual stress or large displacements

$$\text{As } \phi \to \infty,\ G \to 1.25\frac{c_v}{\pi}ph$$

Since $c_v \approx \pi/2$ for circular window, the blister equation can be expressed approximately true as

$$G \approx g(\phi)\frac{1}{2} ph = C \cdot p \cdot h = (0.5 - 0.625)ph \tag{2-37}$$

The constant *C* for blister equation is plotted in Figure 2-7, it shows that the constant C varies over the range from 0.5 to 0.625.

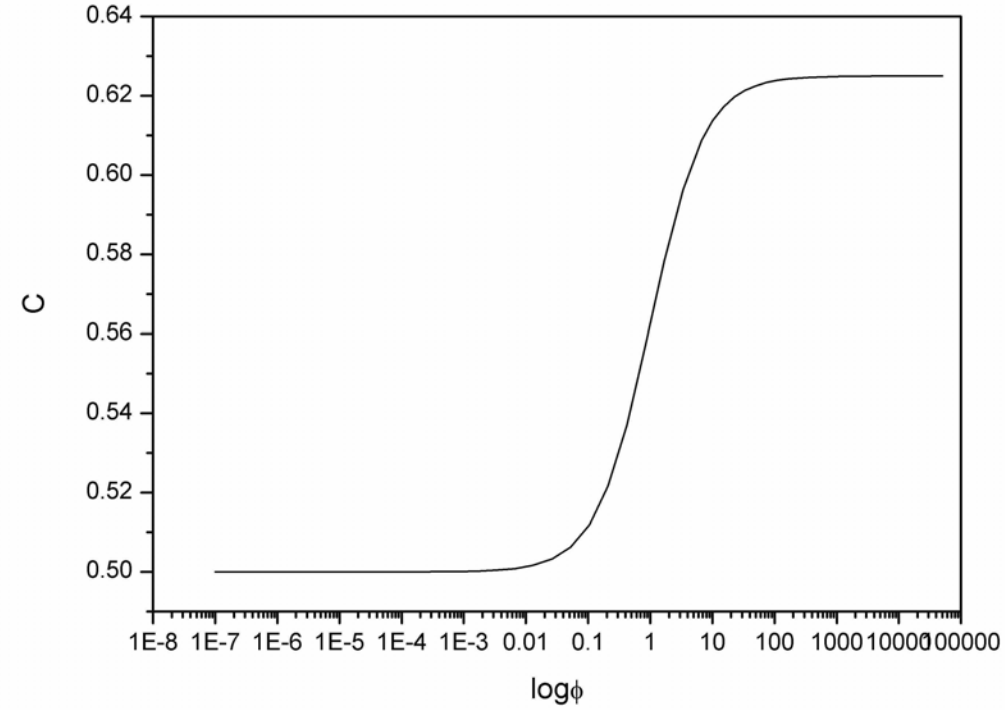

Figure 2-7: The constant C for blister equation

K.T. Wan

Wan *et al* **[Arjun 2005]** studied the mechanical behavior of a blister film under a uniform pressure which changes from a bending plate to a stretching membrane; in another word, he studied the characteristic bulge-to-blister transition. *G* was derived based on the constitutive relation *G=Cph*. The constant *C* is

$$\frac{G}{ph} = \left(\frac{n+2}{n+1}\right)\left(\frac{V_0}{\omega_0}\right) \tag{2-38}$$

where the ω_0 is the normalized blister height and index *n* is the instantaneous value at the final applied pressure *p* throughout the entire loading process.

$$\omega = \frac{h}{t} = \left(\frac{pa^4}{2Dt}\right)\left(\frac{I_0(\beta(r/a)) - I_0(\beta)}{\beta^3 I_1(\beta)} + \frac{1-(r/a)^2}{2\beta^2}\right)$$

$$\omega_0 = \omega(\frac{r}{a} = 0) = \left(\frac{pa^4}{2Dt}\right)\left(\frac{1 - I_0(\beta)}{\beta^3 I_1(\beta)} + \frac{1}{2\beta^2}\right) \tag{2-39}$$

where $D = \frac{Et^3}{(1-\nu^2)}$, $\beta = \left(\frac{\sigma \cdot a^2}{D}\right)^{1/2}$ and $I_n(x)$ denotes the *n*th-order modified Bessel equation of the first kind.

The normalized blister volume V_0 is

$$V_0 = \int_0^1 2\omega(\frac{r}{a})d(\frac{r}{a}) = \left(\frac{pa^4}{2Dt}\right)\left(\frac{2}{\beta^4} + \frac{1}{4\beta^2} - \frac{I_0(\beta)}{\beta^3 I_1(\beta)}\right) \tag{2-40}$$

The constitutive relation is found by invoking the linear stress-strain relationship for a membrane

$$\rho = \frac{2^{1/2}\beta^{11/2} I_1(\beta)}{\left[9\beta I_1(\beta)^2 - 6\beta I_0(\beta) I_1(\beta) - 24 I_1(\beta) I_2(\beta)\right]^{1/2}} \tag{2-41}$$

The constitutive relation $\rho(\omega_0)$ shows a linear behavior in the bending limit and a cubic behavior in the stretching limit.

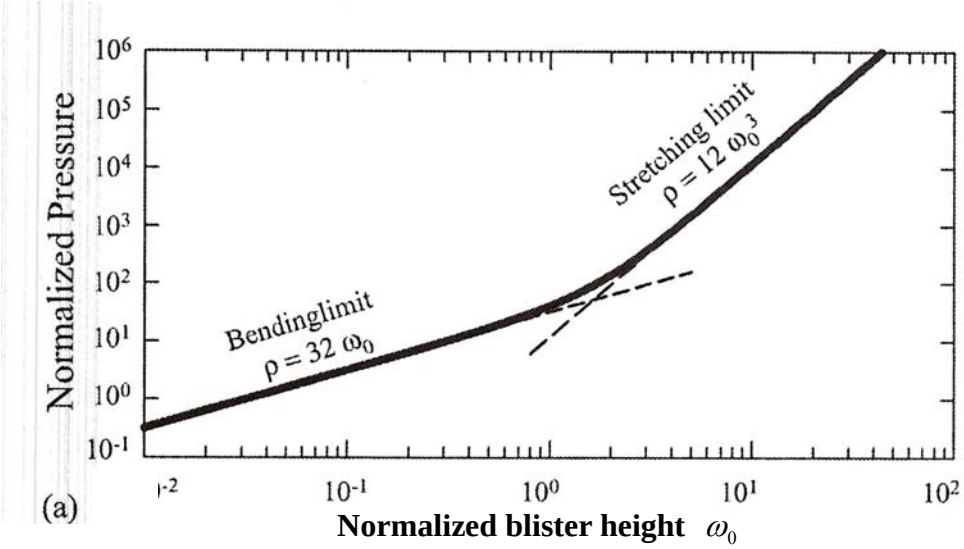

Figure 2-8: The constitutive relation $\rho(\omega_0)$ **[Arjun 2005]**.

The limiting cases of pure bending and pure stretching can be derived from equation (2-38).

As $\omega_0 \to 0$, $G \to \frac{1}{2} ph$ (for small deflection or pure bending)

As $\omega_0 \to \infty$, $G \to \frac{5}{8} ph$ (for large deflection or pure stretching)

The constant C for blister equation is plotted in Figure 2-9 as a function of normalized blister height; it also shows that the constant C varies over the range from 0.5 to 0.625.

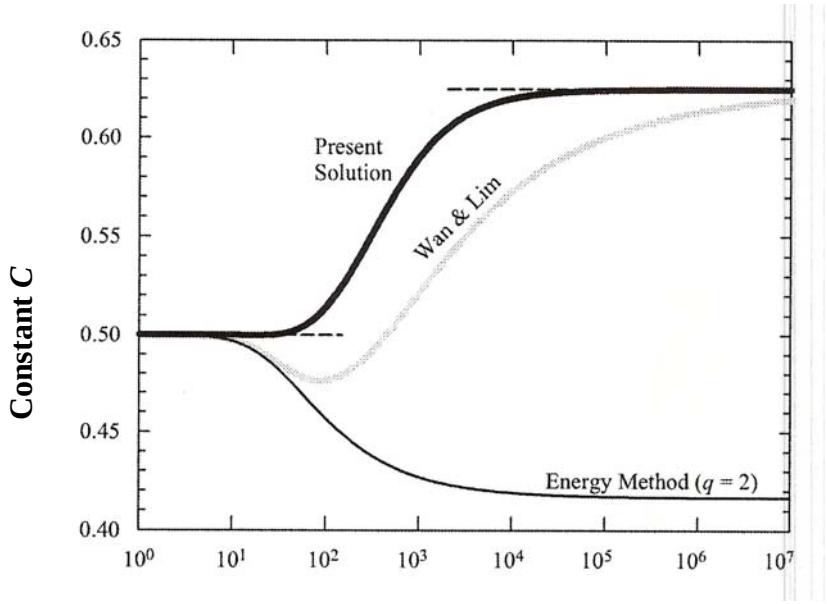

Figure 2-9: The fracture parameter C for various approaches **[Arjun 2005]**.

Cotterell and Chen

The crack extension force G_c could be expressed in terms of the pressure and the maximum deflection by G_c=Cph **[Cotterell 1997]**. When the blister is in transition from plate-like to membrane behavior, the equation for large deflections of plates can be used. The crack extension force factor C is shown in Figure 2-10 as a function of the maximum non-dimensional blister deflection. For non-dimensional blister deflection $\omega_0 > 4$, the crack extension force factor C is

$$C = C_m \left[1 - \exp(-1.35\omega_0^{0.36})\right] \tag{2-42}$$

where the C_m is the membrane crack extension force factor given in Table 2-3.

Table 2-3: the membrane crack extension force factor Cm

ν	0.25	0.35	0.45	0.5
Cm	0.6531	0.6503	0.6472	0.6456

The crack extension force factor for $\omega_0 < 4$ is given by the polynomial

$$C = 0.5 + a_2\omega_0^2 + a_3\omega_0^4 + a_4\omega_0^6 \tag{2-43}$$

where the coefficients are given in Table 2-4.

Table 2-4: the coefficients for crack extension force factor C, for small deflections

ν	a_2	a_3	a_4
0.25	8.34×10^{-3}	-1.04×10^{-4}	-7.18×10^{-6}
0.35	7.87×10^{-3}	-2.89×10^{-5}	-1.07×10^{-5}
0.45	7.40×10^{-3}	1.35×10^{-5}	-1.18×10^{-5}
0.5	7.01×10^{-3}	6.63×10^{-5}	-1.40×10^{-5}

Figure 2-10 shows that the limit of crack extension force factor for large deflection is about 0.65, which depends on the Poisson's ratio. Note that crack extension force factor C varies weakly with Poisson's ratio.

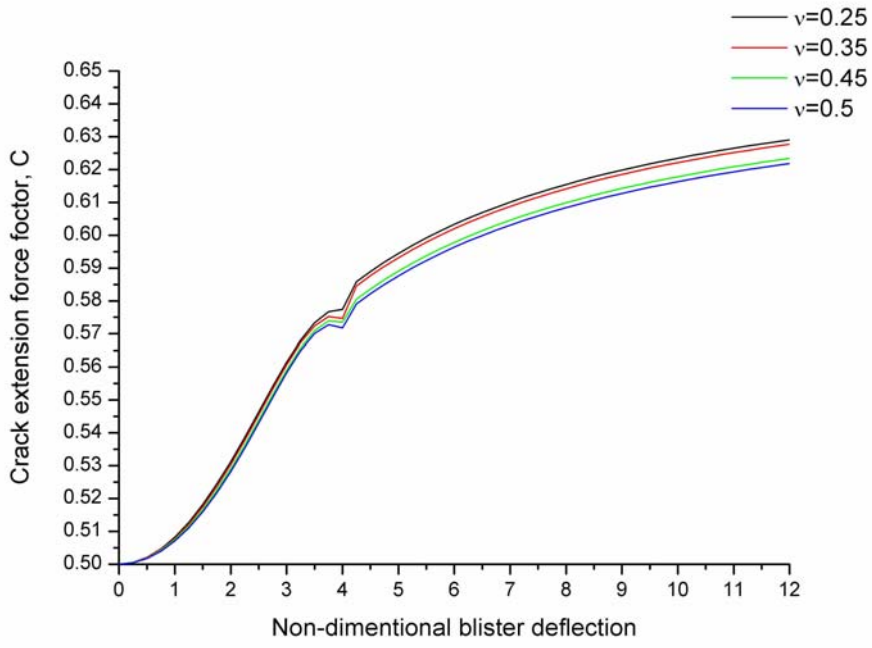

Figure 2-10: The fracture parameter C for various approaches.

Table 2-5 summary of some reported equations of the energy release rate.

Author	Energy release rate equation for blister test
Dannenberg **[Dannenberg 1961]**	$G=p\Delta V$
Hinkley **[Hinkley 1983]**	$G=(ph)/4$
Gent and Lewandowski **[Gent 1987]**	$G=(5Cph)/4$, $C=0.518$ for $\nu=0.3$
J.G. Williams **[Williams 1997]**	$G=\frac{5ph}{4}\frac{\int_0^1 f^{-1}\cdot\varsigma^3 d\varsigma}{\int_0^1 f^{-1}\cdot\varsigma\cdot d\varsigma}$, $\varsigma=\frac{r}{a}$
K.T.Wan **[Wan 1998]**	$\frac{G}{ph}=\left(\frac{n+2}{n+1}\right)\left(\frac{V_0}{\omega_0}\right)$
Shirani and Liechti **[Shirani 1998]**	$G=0.619ph$
Hohlfelder and Vlassak **[Hohlfelder 1998]**	$G=g(\phi)\cdot\frac{c_v}{\pi}ph$, $g(\phi)=\left(\frac{4+5\phi}{4+4\phi}\right)$, $\phi=\frac{c_2 M}{c_1\sigma_0}\left(\frac{h}{a}\right)^2$

Table 2-5 summarizes some reported equations of the energy release rate. From the above analysis, the final expression of G can be approximated as from above solutions:

$$G = C\cdot p\cdot h \tag{2-44}$$

where C is a dimensionless function of the window geometry. C relates to the values of the film residual stress σ_0, film biaxial modulus $E/(1-\nu)$ and the geometrical ratio h/a. During the blister growth, the equilibrium shape of the blister contour is circular and its ratio h/a is almost constant. The value of C may be taken as constant during a given test, and equal to 0.5 for very high values of the residual stress and small deflection or to 0.649 for usual or low residual stresses and large deflection **[Bosseboeuf 1997]**.

3.4.Near edge loads

We have calculated the crack extension force (G) for a circular blister using a global approach, and the crack extension force may also be obtained using a local approach. The crack extension force can be related to the forces in the film at the window edge,

where debonding occurs. The cross section of the edge of the window is illustrated in Figure 2-11.

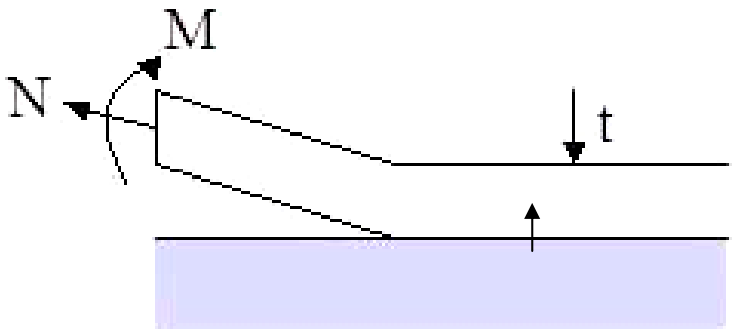

Figure 2-11: Forces at blister edge.

Jensen **[Jensen 1991]** indicated that the energy release rate along the crack front could be shown as:

$$G = \frac{1-\nu^2}{2Et^3}\left(12M^2 + h^2N^2\right) \tag{2-45}$$

where M is the bending moment and N is the normal force.

For a film that has an initial stress, expression (2-45) becomes:

$$G = \frac{6\left(1-\nu^2\right)M^2}{Et^3} + \frac{t\left(1-\nu^2\right)}{2E}\left(\sigma_R - \sigma_0\right)^2 \tag{2-46}$$

where σ_R is the mean radial stress applied to the film ($\sigma_R \times t = N$). The maximum bending stress occurs at the film surfaces and is related to the bending moment M, so (2-46) becomes:

$$G = \frac{t\left(1-\nu^2\right)}{2E}\left[\frac{\sigma_{B-Max}^2}{3} + \left(\sigma_R - \sigma_0\right)^2\right] \tag{2-47}$$

The expressions (2-45) and (2-47) describe the relationship between the crack extension force and stress in the film. The crack extension force that can be obtained during an experiment is limited by the film's acceptable stresses. At high stresses, film may deform plastically which invalidates the assumption of linear elastic deformation.

3.5.Mode mixity in blister test

The mode mixity has been introduced in Chapter 1; here we present the mode mixity solution for the blister test.

Hutchinson and Suo **[Hutchinson 1992]** have obtained a solution for the stress intensity factor:

$$K \cdot t^{i\varepsilon} = -\left(\frac{6(1-\alpha)}{1-\beta^2}\right)^{1/2} \cdot t^{-3/2} \cdot \left(\frac{t^2(\sigma_R - \sigma_0)}{\sqrt{12}} + iM\right) \cdot e^{i\omega} \tag{2-48}$$

where ω is phase factor concerning the Dundur's elastic mismatch parameters α and β. Choosing a characteristic length scale equal to the film thickness, the mode mixity associated with this stress intensity factor is:

$$\tan(\psi) = \frac{\mathrm{Im}\left(Kt^{i\varepsilon}\right)}{\mathrm{Re}\left(Kt^{i\varepsilon}\right)} = \frac{\sqrt{12}M\cos\omega + t^2(\sigma_R - \sigma_0)\sin\omega}{-\sqrt{12}M\sin\omega + t^2(\sigma_R - \sigma_0)\cos\omega} \tag{2-49}$$

The mode mixity of a blister test can be calculated using this expression. For the case of non-residual stress film, (2-49) reduces to a simpler form:

$$\tan(\psi) = \frac{\sqrt{12}M\cos\omega + tN\sin\omega}{-\sqrt{12}M\sin\omega + tN\cos\omega} \tag{2-50}$$

where M is effective bending moment and N means the effective membrane normal forces.

The ratio of tN/M at $r=R$ is given by Jensen **[Jensen 1998]**

$$\frac{tN}{M_{r=R}} = \sqrt{\left(\overline{\varphi}_m\right)^3 48(1-\nu^2)} \cong 1.078 + 0.636\nu \tag{2-51}$$

And

$$\tan(\psi) = \frac{(0.311 + 0.184\nu)\tan\omega + 1}{(0.311 + 0.184\nu) - \tan\omega} \tag{2-52}$$

For small deflections the mode-mixity angle is given by Jensen **[Jensen 1991]**

$$\psi = -(90^0 - \omega) \tag{2-53}$$

Using the tabulated values of ω in Suo and Hutchinson **[Suo 1990]**, the most used range of ω is between 45 and 65. The calculated phase angles vary from roughly –42° to –67°, that indicates the existence of mode Ⅱ stress intensities. Therefore, we can

expect that the interfacial toughness measured by blister test will greater than that obtained for pure mode Ⅰ loading.

A simple, one parameter family of mixed mode fraction criteria can be introduced **[Hutchinson 1992, Suo 1990]**. The parameter λ adjusts the influence of the mode 2 contribution in the criterion. The limit λ=1 denotes the ideally brittle interface (G_c=G_{Ic}) with all mode combination. When λ=0 crack advances only depends on the mode I component.

$$G(\psi) = G_I^c[1 + (\lambda - 1)\sin^2\psi]^{-1} \tag{2-54}$$

The toughness is plotted as a function of phase angles in Figure 2-12. The toughness increases as phase angles are approaching 90^0 (mode II).

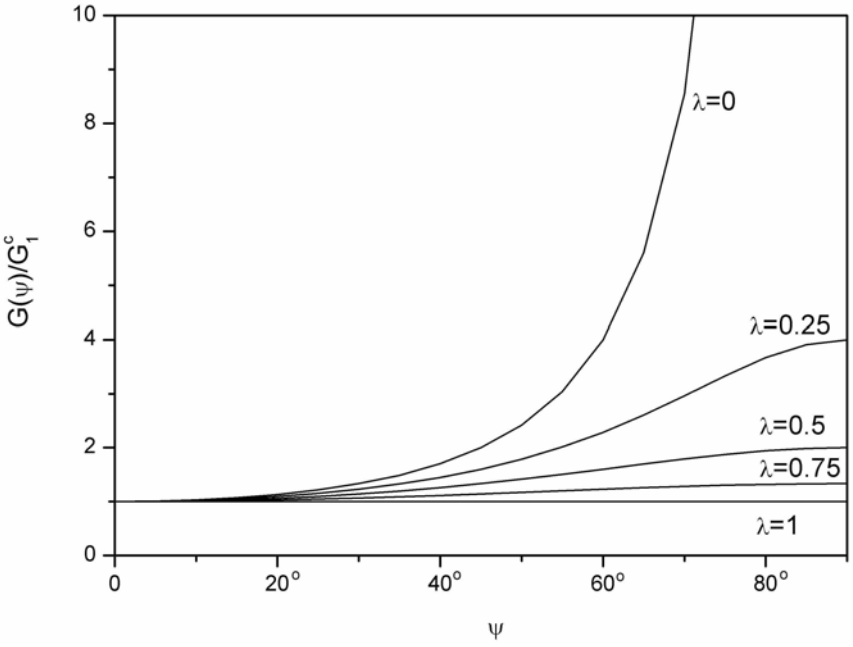

Figure 2-12: A families of interface toughness functions.

3.6.Correction for plastic work

For many film-on-substrate systems, it is usually assumed that the top film deforms elastically since the yield stress of thin film materials increases as the thickness decreases. However, thicker metal coatings in annealed condition may tend to deform plastically during the blister test. Then the strain energy developed during the blister test is composed of the work of elastic deformation and the work of plastic deformation. They have to be separated for adhesion measurement, since only the elastic strain energy is reversible and can be released from the pressurized membrane to cause the interface crack propagation.

Since the film has deformed plastically after previous pressurization, the volume underneath the new free-standing membrane can be related to its previous plastic residual deflection height h_p. The total strain energy of the pressurized film should then be changed to

$$U_{strain} = \int_0^{hp+h} p(h)dV = \int_0^{hp} p(h)dV + \int_{hp}^{h} p(h)dV \tag{2-55}$$

The strain energy contributed by the plastic deformation should be extracted from the total apparent strain energy, to work out the elastic energy release rate which causes crack propagation. A very simple way to correct this plastic bulging of the membrane is to subtract the corresponding residual permanent deflection h_{pi} for each quasi-linear inflation-deflation elastic curve at a critical point for a given specimen, as illustrated on figure 2-13. The critical debonding points then correspond to much smaller values of corrected deflection (h-h_{pi}) just as if the membrane had remained elastic throughout the test, and they are located on such hyperbola $C{\cdot}p{\cdot}(h\text{-}h_{pi}) = G'_i$ with much smaller and more reliable values of debonding energy.

For example, figure 2-14 shows the blister equation fit to the experimental data at the de-bonding point for a specimen with a silver layer fired at 850°C. The uncorrected crack propagation energy was acquired as 11 J/m^2, while the height being corrected as $h = h_{exp} - h_{pla}$, the result diminished to 4.5 J/m^2. Thanks to this very simple procedure, we can subtract the effect of the generalized plastic yielding in the Ag membrane from the total strain energy produced by the pressure application.

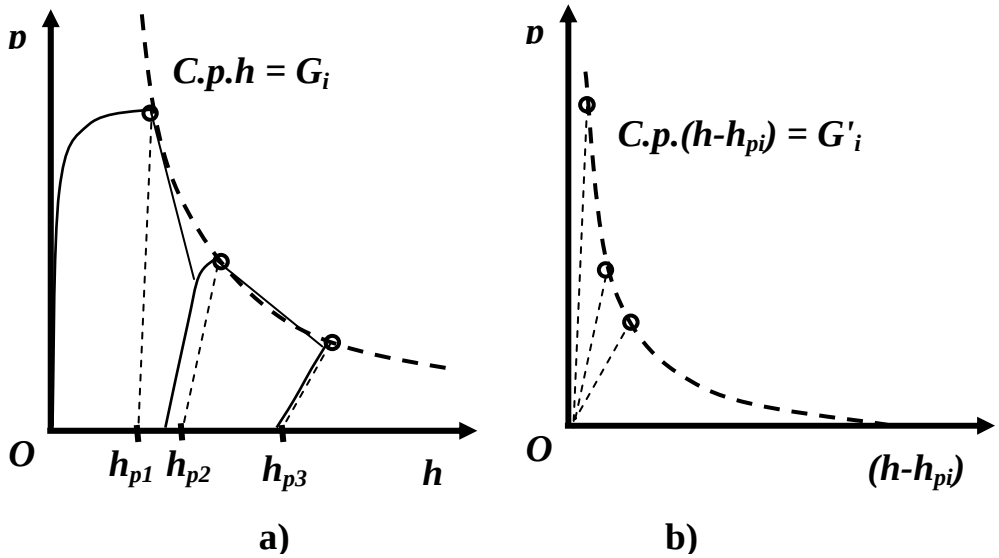

Figure 2-13: schematic of the principle of correction for the effect of the generalized plasticity of the silver membrane on the interfacial debonding energy.

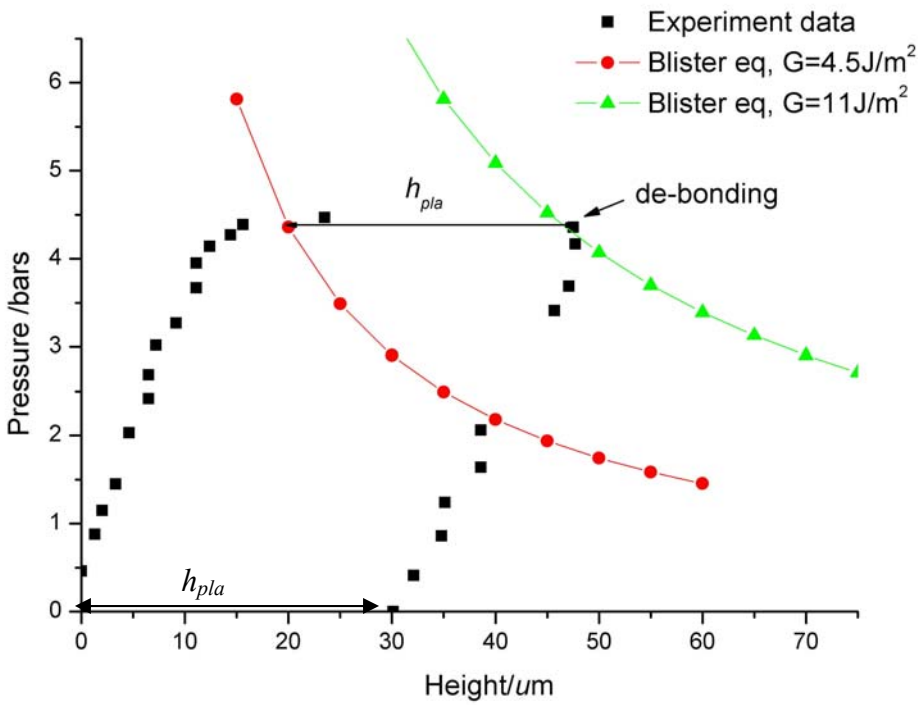

Figure 2-14: Illustration of blister equation fit to experimental data for a specimen fired at 850°C. The uncorrected value G = 11 J/m^2 is adjusted on the experimental debonding point. The corrected value G' = 4.5 J/m^2 is adjusted on the corrected debonding height, according to the schematic of figure 2-13.

4. Conclusions

Blister test is a quantitative technique for measuring interface adhesion strength. The experimental results of blister test can be analyzed be fitting a simple expression, which is approximated by different reporters in literature, as

$$G = C \cdot p \cdot h \tag{2-44}$$

Energy release rate of interfacial crack propagation can be approximated from above equation. C is a dimensionless function of the window geometry and relates to the values of the film residual stress σ_0, film biaxial modulus $E/(1-\nu)$ and the geometrical ratio h/a. The value of C may be taken as constant and equal to 0.5 for very high values of the residual stress and small deflection or to 0.649 for usual or low residual stresses and large deflection.

References

[Arjun 2005] A. Arjun, K. T. Wan, "*Derivation of the strain energy release rate G from first principles for the pressured blister test*" International Journal of Adhesion and Adhesives, 25 (2005) pp. 13-18.

[Bosseboeuf 1997] A. Bosseboeuf, M. Dupeux, M. Boutry, T. Bourouina, "*Bulge and blister test for assessment of coating strength and interfacial adhesion: Experimental challenge and theoretical tools,*" Proceedings of the International Workshop October 13-17, 1997 in Holzhau (Germany), pp.169-181.

[Cotterell 1997] B. Cotterell, Z.Chen, "*The blister test-transition from plate to membrane behaviour for an elastic material*" International Journal of Fracture, 86 (1997) pp.191-198.

[Dannenberg 1961] H. Dannenberg, "*Measurement of adhesion by a blister method,*" Journal of Applied Polymer Science, 5(14), (1961)pp.125-134.

[Dupeux 1998] M. Dupeux, A. Bosseboeuf, "*Application of the blister test to adhesion energy measurements in metal / ceramic film-on-substrate systems*," Interfacial Science in Ceramic Jointing, (1998) pp.319-327.

[Felder 2003] E. Felder, E. Darque-Ceretti, Adhésion et Adhérence, CNRS Edt., Paris, 2003.

[Gent 1987] A.N. Gent, L.H. Lewandowski, "*Blow-off pressures for adhering layers*" Journal of Applied Polymer Science, 33 (1987) pp.1567-1577.

[Guo 2005] S. Guo, K. T. Wan, D. A. Dillard, "*A bending-to-stretching analysis of the blister test in the presence of tensile residual stress*" International journal of solids and structures, 42 (2005) pp.2771-2784.

[Hbaieb 2005] K. Hbaieb, Y.W. Zhang, " *A parametric study of a pressurized blister test for an elastic-plastic film-rigid substrate system*" Materials science and engineering A, 390 (2005) pp385-392.

[Hinkley 1983] J.A. Hinkley, "*A blister test for adhesion of polymer films to SiO_2*" Journal of Adhesion, 16 (1983) pp.115-125.

[Hohlfelder 1995] R. J. Hohlfelder, J. J. Vlassak, W. D. Nix, H. Luo, C. E. D. Chidsey, "*Blister test analysis methods*" Materials Research Society Symp. Proc. 356, (1995) pp.585-590.

[Hohlfelder 1996] R. J. Hohlfelder, W. D. Nix, A. S. Mack, "*Using the blister test to measure interfacial fracture toughness in inorganic film/substrate systems,*" communication at the Materials Research Society Fall Meeting, Dec. 2-6, (1996), Boston (Mass).

[Hohlfelder 1997] R. J. Hohlfelder, H. Luo, J. J. Vlassak, C. E. D. Chidsey, W. D. Nix, "*Measuring interfacial toughness with the blister test*" Materials Research Society Symp. Proc. 436, (1997) pp.115-120.

[Hohlfelder 1998] R.J. Hohlfelder, "*Bilge and Blister testing of thin films and their interfaces,*" Ph.D, Stanford University (1998).

[Hutchinson 1992] J.W. Hutchinson, Z. Suo, "*Mixed mode cracking in layer materials*" Advances in Applied Mechanics, 29 (1992) pp.63-191.

[Jensen 1990] H.M. Jensen, "*Mixed mode interface fracture criteria,*" Acta Metallurgica, 38, (1990) pp.2637-2644.

[Jensen 1991] H. M. Jensen, "*The blister test for interface toughness measurement*", Engineering Fracture Mechanics, Vol. 40, no. 3, (1991) pp. 475-486.

[Jensen 1998] H. M. Jensen, "*Analysis of mode mixity in blister test*", International journal of Fracture, V94, (1998) pp. 79-88.

[Lee 2003] C. Y. Lee, "*Adhesion strength between dielectric and electrode materials*", Master Thesis, National Taiwan University (Taiwan) (2003).

[Lee 2006] C.Y. Lee, M. Dupeux, W.H. Tuan, "*Adhesion strength of Ag/$BaTiO_3$ interface*" Scripta Materialia, 54 (2006) pp.453–457.

[Mougin 2002] J. Mougin, M. Dupeux, A. Galerie, L. Antoni, "*Inverted blister test to mesure adhesion energy of thermal oxide scales on metals or alloys*" Materials Science and Technology, 18, (2002) pp.1217-1220.

[Mougin 2003] J. Mougin, M. Dupeux, L. Antoni, A. Galerie, "*Adhesion of thermal oxide scales grown on ferritic stainless steels measured using the inverted blister test* " Materials Science and engineering A, 359, (2003) pp.44-51.

[Shirani 1998] A. Shirani, K. M. Liechti, "*A calibrated fracture process zone model for thin film blistering,*" International Journal of Fracture, 93 (1-4) (1998) pp.281-314.

[Sizemore 1995] J. Sizemore, R. J. Hohlfelder, J. J. Vlassak, W. D. Nix, "*Measuring the adhesion of diamond thin films to substrates using the blister test*" Materials Research Society Symp. Proc. 383, (1995) pp.197-207.

[Suo 1990] Z. Suo, and J.W. Hutchinson, "*Interface crack between two elastic layers*" International Journal of Fracture, 43, (1990) pp.1-18.

[Taheri 2000] N. Taheri, N. Mohammadi, N. Shahidi, "*An automatic instrument for measurement of interfacial adhesion of polymeric coatings,*" Polymer Testing, 19 (2000) pp.959–966.

[Volinsky 2002] A. A. Volinsky, N. R. Moody, W. W. Gerberich. "*Interfacial toughness measurement for thin films on substrate*" Acta Materialia, 50 (2002) pp.441-466.

[Wan 1998] K.T. Wan, S. C. Lim, "*The bending to stretching transition of a pressurized blister test*" International journal of fracture, 92 (1998) pp.L43-L47.

[Wan 2000] K. T. Wan, "*A novel blister test to investigate thin film delamination at elevated temperature,*" International Journal of Adhesion and Adhesives, 20 (2000) pp.141-143.

[Wang 1999] C. WANG, "*Measurements of Interfacial Strength from the Blister Test*" Journal of Applied Polymer Science, Vol. 73, (1999) pp.1899–1912.

[Williams 1997] J. G.. Williams, "*Energy release rates for the peeling of flexible membranes and the analysis of blister test*" International journal of fracture, 87 (1997) pp.265-288.

[Zhou 2003] Y. C. Zhou, T. Hashida, C.Y. Jian, "*Determination of interface fracture toughness in thermal barrier coating system by blister test*" Transactions of the ASME, V125 (2003) pp.176-182.

Chapter Ⅲ

Interface Adhesion Measurement by Indentation Test

1. Introduction 57
2. Development of the indentation test for measuring interfacial fracture toughness. 59
2.1. Development of the normal indentation test 59
2.2. Development of the interface indentation test 59
2.3. Development of the cross-sectional indentation test 60
3. Mechanical analysis 60
3.1. Normal indentation test 60
3.2. Interface indentation test 61
3.3. Cross-sectional indentation test 63
3.3.1. The Plate model 63
3.3.2. Analytical approximation (Tapered beams model) 64
3.3.3. The model of an elastic plate with elastically restrained edges 68
3.3.4. Point load model 73
4. Mode mixity of cross-sectional indentation test 73
5. Conclusions 75
References 76

1. Introduction

The adhesion determination of coatings faces numerous experimental difficulties. To find a simple test by using a usual apparatus attracts many attentions. Indentation tests are very simple and widely used techniques the results of which can be interpreted in terms of materials mechanical properties, like hardness, toughness and Young's modulus. In the specific case, indentation test can be performed to determine adhesion strength between metal and oxide. In this chapter we present three indentation methods: normal indentation test, interface indentation test and cross-sectional indentation test. In normal indentation test a sharp indenter is thrust into the coating under controlled conditions. A concomitant delamination of the coating can also occur starting at the edge of the indenter (Figure 3-1). Normal indentation test is commonly used to characterize interface adhesion in thin film/substrate systems by nanoindentation. In general, plastic deformation occurs in the proximity of the impressed region for sharp indenters such as Berkovich indenters or Vickers indenters.

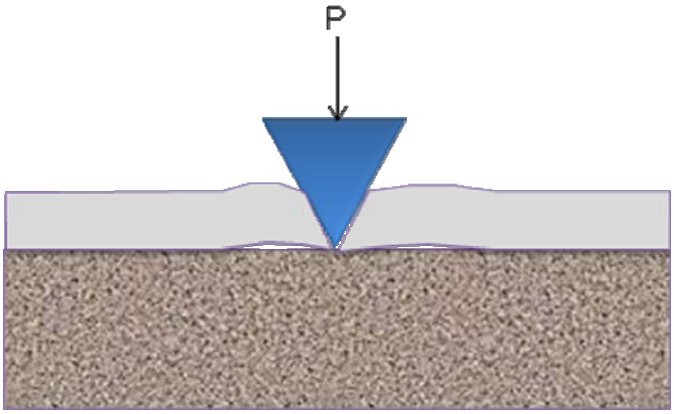

Figure 3-1: Principle of the normal indentation test.

Interface indentation test can create and propagate a crack at the interface between two adhesive materials, both bulk bi-materials and film/substrate system (Figure 3-2). The load necessary to initiate a crack is interpreted in terms of an apparent interfacial toughness which can represent adhesion **[Lesage 2001]**.

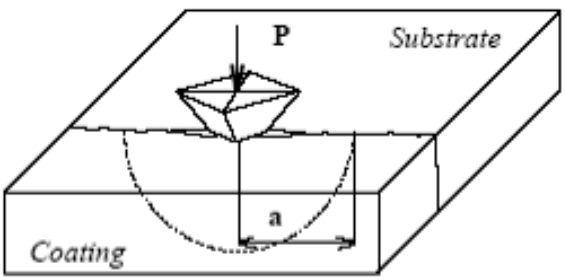

Figure 3-2: Principle of the interface indentation test **[Lesage 1993]**.

Cross-sectional indentation test come from a new test method named Cross-Sectional Nanoindentation test (CSN test). CSN test can be used to measure interface energy release rate between a tough thin film and its brittle substrate by nanoindentation tester. The difference between this indentation technique (CSN) and the two previous ones is that cracks are initiated in the brittle substrate by indenting with a Berkovich diamond tip close to the interface on a cross section of the coated specimen. Cracks propagate from two corners of the indentation to the thin film/ substrate interface (Figure 3-3), that will make part of the substrate separate outside and push the thin film to debond from substrate.

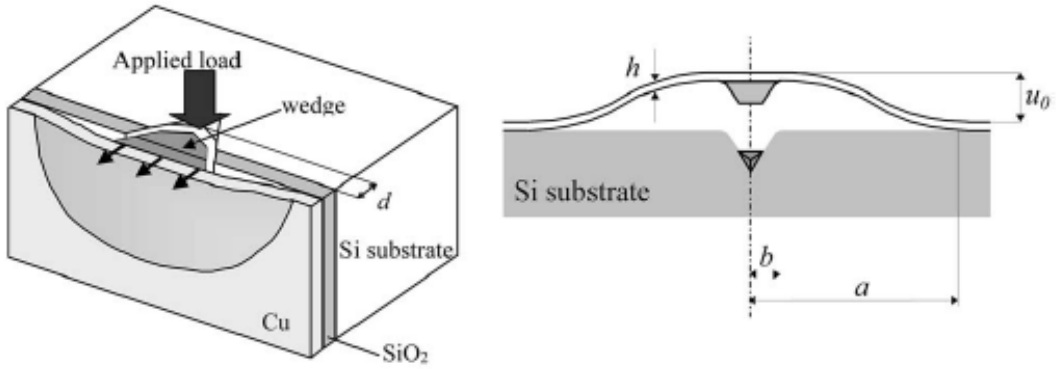

Figure 3-3: Schematic of CSN test configuration **[Sanchez 1999]**.

In this study we try to use Vickers indentation test to carry out similar debonding experiment under larger loads (Figure 3-4). The Vickers test method consists of indenting the test material with a diamond indenter, in the shape of a pyramid with a square base and an angle of 136 degrees between opposite faces. Because Vickers diamond tip is similar to Berkovich diamond tip, we can assume that the model for CSN test can be transferred to our cross-sectional indentation test. More detail description is presented in this chapter.

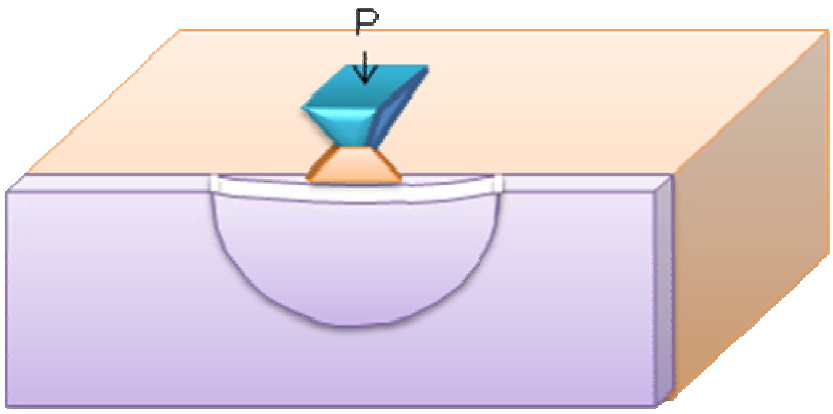

Figure 3-4: Principle of the cross-sectional indentation test.

2. Development of the indentation test for measuring interfacial fracture toughness

2.1. Development of the normal indentation test

Indentation test is used to quantify the thin film interfacial adhesion. An early example of the use of this technique was given by Engle *et al* **[Engle 1983]**. Marshall and Evans **[Marshall 1984]** proposed a fracture analysis of indentation induced delamination of thin films, which is a combination of Linear Elastic Fracture Mechanics (LEFM) and simplified post-buckling theory. Nanoindentation was recently used on a thin film of thickness of micron order on an elastic substrate. It provides a simple, easy, and powerful technique for measuring the interfacial adhesion and fracture toughness **[Volinsky 2002, Bull 2005]** for tough thin coatings (metal films in most cases) with relatively weak adhesion.

2.2. Development of the interface indentation test

In order to measure the fracture toughness of the interface, it is necessary to initiate and propagate a crack at the interface between two materials. Palmqvist *et al* (1957) proposed to use the indentation test on the interface. Several authors have attempted to define either a cracking energy release rate or interface toughness from the indentation test results. Anstis *et al*. used Vickers indentation to evaluate the fracture toughness of bulk brittle materials. An approach was made which involves direct measurement of Vickers-produced radial cracks as a function of indentation load **[Anstis 1981, Chantikul 1981]**. D. Choulier **[Choulier 1998]** tried to find out the equations for interface indentation test, which could provide the interface energy G_c and toughness K_{IC}.

Lesage *et al*. have extended the theoretical and experimental work on interface indentation test **[Lesage 1993, 1999, 2001, Demarecaux 1996, Chicot 1996]**. For experimental development, Latella *et al*. evaluated the interfacial toughness and bond strength of sandwiched silicon structures using interface indentation test **[Latella 2002]**. Richard *et al*. used interface indentation test to study the adhesion of plasma sprayed NiCrAlY coating **[Richard 1996]**. Qi *et al*. tried to measure interfacial toughness of the nickel-nickel oxide system **[Qi 2003]**. Zhang and Lewandowski changed the indentation position from interface to brittle substrate and observed the crack propagation from substrate to interface **[Zhang 1994]**.

2.3. Development of the cross-sectional indentation test

Cross-sectional indentation test has been derived from Cross-Sectional Nanoindentation test (CSN test). Sanchez *et al*. proposed this new mechanical test especially designed for measuring the fracture energy of thin film/substrate interface **[Sanchez 1999, Elizalde 2003]**. Several theoretical models have been proposed to analyze interfacial adhesion. Sanchez *et al*. put forward a one-dimensional model of an assembly of tapered beams. At beginning CSN test was created to be used in an elastic situation. In metal thin film/substrate systems, CSN test will cause plenty of plastic deformation in metal thin film. Therefore, fully elastic model are only approximations in such cases. Models for plastic behavior are complex and not completely developed yet, so some authors used Finite Element Method to analyze and to subtract plastic effects **[Ocana 2006, Molina 2007]**. Scherban *et al*. **[Scherban 2003]** studied the behavior of adhesion of a metal–dielectric interface where plastic deformation is taken into account by means of Finite Element Method. A modified analytical approximation has been suggested by Zheng *et al*. **[Zhen 2004, 2005]**, who employed the bending theory of an anisotropic circular plate instead of that of an isotropic thin plate. Li **[Li 2006]** considered the influences of the material properties of the substrate and proposed a new model.

Chan *et al*. started to measure interface toughness of FeCo thin films on Ti-6Al-4V **[Chan 2006]**. To reduce the plastic deformations is the best solution but it cannot be done in thin film system **[Roy 2006]**. In this chapter, we try to introduce the CSN test models to cross-sectional indentation test, using Vickers indentation in the place of Nanoindentation.

3. Mechanical analysis

3.1. Normal indentation test

Toonder *et al*. **[Toonder 2002]** provide the analysis for the determination of spall of a brittle thin film induced by a Berkovich indentation. The strain energy release rate is:

$$G = 1.42\frac{Eh^5}{L^4}\left(\frac{(a/L)+(\beta_c\pi/2)}{(a/L)+\beta_c\pi}\right)^2 + \frac{h(1-\nu)\sigma_r^2}{E} + \frac{3.36(1-\nu)h^3\sigma_r}{L^2}\left(\frac{(a/L)+(\beta_c\pi/2)}{(a/L)+\beta_c\pi}\right) \tag{3-1}$$

where E is the Young's modulus of the coating; h is the thickness of the coating; v is the Poisson's ratio of the coating; σ_r is the residual stress in the coating . L, a and β_c define the geometry of the chipped piece (Figure 3-5). This equation is very sensitive to the precise values of thickness and crack length measured [**Bull 2005**].

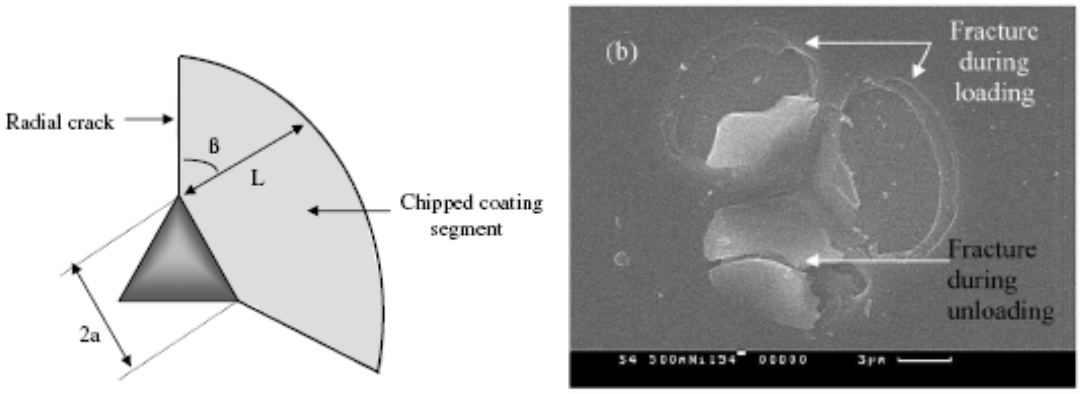

Figure 3-5: Schematic of the geometry of a chipped segment showing the dimensions used in calculating interfacial toughness **[Bull 2005]**.

3.2. Interface indentation test

For brittle materials, toughness deduced from indentation tests can be expressed by a relation involving the material mechanical properties, the load and the corresponding crack length:

$$K_c = \alpha \frac{P}{a_c^{3/2}} \left(\frac{E}{H} \right)^{1/2} \tag{3-2}$$

where α is a material-independent constant for Vickers produced radial cracks, P is the applied load, a is the crack length, E and H mean the Young modulus and Vickers hardness. Constant α is about 0.016 ± 0.004 **[Richard 1996]**.

For interface indentation test, this relation cannot be used directly, because indentation is performed into two different materials. We need to express the contributions of the substrate and the film into ratio (E/H) between the apparent Young modulus and Vickers hardness of the interface. The mean geometrical characteristics of the substrate and the film couple: indent diagonal (d_I) and plastic zone radius (b_I) of the interface can be expressed as:

$$d_I = \frac{(d_F + d_S)}{2}, \quad b_I = \frac{(b_F + b_S)}{2} \tag{3-3}$$

where I, F and S are the indexes of the interface, film and substrate respectively. d_I, d_F and d_S are deduced from the hardness general relation

$$H_v = 1.8544 \frac{P}{d^2} \tag{3-4}$$

and b_I b_F and b_S from Lawn relation which connects the plastic zone to the mechanical properties of a material

$$b_i = \frac{d}{2}\left(\frac{E}{H}\right)^{1/2}\left(\cot^{1/3}\xi\right) \tag{3-5}$$

Equation 3-5 can be written as

$$\left(\frac{E}{H}\right)^{1/2} = \frac{2}{\left(\cot^{1/3}\xi\right)}\frac{b_i}{d_i} = \frac{2}{\left(\cot^{1/3}\xi\right)}\frac{b_F + b_S}{d_F + d_S} \tag{3-6}$$

Replacing d_F, d_S and b_F, b_S by their expression from (3-4) and (3-5), we obtain **[Lesage 1999]**

$$\left(\frac{E}{H}\right)^{1/2} = \frac{\left(E/H\right)_S^{1/2}}{1+\left(H_s/H_F\right)^{1/2}} + \frac{\left(E/H\right)_F^{1/2}}{1+\left(H_F/H_S\right)^{1/2}} \tag{3-7}$$

Substituting Equation (3-7) into Equation (3-2) we can obtain the fracture toughness K_I of the interface.

Consider two isotropic elastic half planes (Material 1 and Material 2) joined with an interfacial crack and subjected to in-plane loading. The Young's modulus and Poisson's ratio of the respective materials are E_i and v_i (i=1, 2). The interface energy release rate for crack growth along the interface can be obtained from the singular stress on the interface along the crack and the displacement of the crack surfaces:

$$G = \frac{\left(1-\beta^2\right)}{E_*}\left(K_I^2 + K_{II}^2\right) \tag{3-8}$$

for the plane strain

$$\beta = \frac{1}{2}\left[\frac{\mu_1(1-2\nu_2)-\mu_2(1-2\nu_1)}{\mu_1(1-\nu_2)-\mu_2(1-\nu_1)}\right],\quad \frac{1}{E_*} = \frac{1}{2}\left(\frac{1-\nu_1^2}{E_1} + \frac{1-\nu_2^2}{E_2}\right)$$

The major fracture mode in interface is mode I, so we can assume that K_{II} is small enough to ignore it. The energy release rate becomes

$$G = \frac{\left(1-\beta^2\right)}{E_*}\left(K_I^2\right) \tag{3-9}$$

3.3. Cross-sectional indentation test

3.3.1. The Plate model

Figure 3-6 shows a sketch of a cross-sectional indentation test. For plate model, it is a circular plate with its edge clamped and an inner ring, at a distance b from the centre, with fixed vertical displacements w_0.The G_{ic} calculation is independent of the distance from the indentation to the interface. The film elastic strain energy is given by

$$U = \int_V \frac{1}{2}\sigma_{ij}\varepsilon_{ij}dV \tag{3-10}$$

Where σ_{ij} is the stress tensor, ε_{ij} is the strain tensor, and V is the volume of the plate. Substituting the stresses and strains into equation 3-10 by their expression as a function of the radial and circumferential bending moments (M_r and M_θ) and taking into account that the twisting moment $M_{r\theta}$=0, because of symmetry, the film elastic strain energy becomes:

$$U = \frac{2\pi}{D\left(1-\nu^2\right)}\int_b^a \left(M_r^2 + M_\theta^2 - 2\nu M_r M_\theta\right) r dr \tag{3-11}$$

Where D is the flexural rigidity of the plate:

$$D = \frac{Eh^3}{12\left(1-\nu^2\right)} \tag{3-12}$$

A semi-circular blister will have approximately one-half of this energy. The debonding energy G is not affected because it is defined by the ratio:

$$G = -\left(\frac{\partial U}{\partial A}\right)_{w_0} \tag{3-13}$$

Where A is the debond area. The area increment is also one-half of a complete circular blister.

Using cylindrical coordinates, equation 3-10 is given by

$$U = \frac{D}{2}\int_A \left(\nabla^2 w\right)^2 r dr d\theta \tag{3-14}$$

For a point load (or displacement w_0) applied at the centre of the plate, the displacement w is

$$w = \frac{w_0}{a^2}\left(2r^2 \ln\frac{r}{a} + a^2 - r^2\right) \tag{3-15}$$

Substituting equation (3-15) into equation (3-14) gives

$$U = \frac{8\pi D w_0^2}{a^2}$$

And then **[Sanchez 1999]**

$$G = -\left(\frac{\partial U}{\partial A}\right)_{w_0} = -\frac{1}{2\pi a}\left(\frac{\partial U}{\partial a}\right)_{w_0} = \frac{8 D w_0^2}{a^4} \tag{3-16}$$

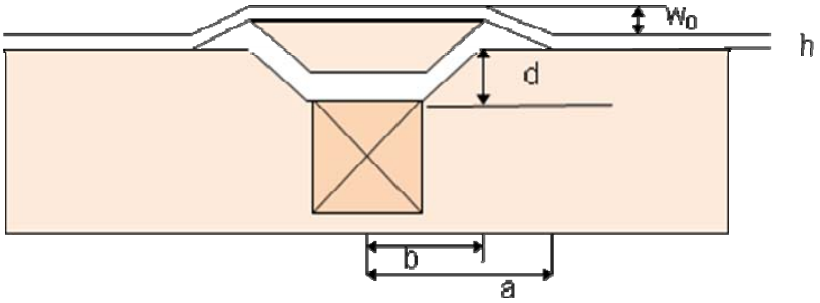

Figure 3-6: sketch of a cross-sectional indentation test.

3.3.2. Analytical approximation (Tapered beams model)

In order to estimate the influence of the partial relaxation of the circumferential stresses in the plate, the plate can be modeled as an assembly of tapered beams when a semi-circular geometry is considered (Figure 3-7). Using the beam bending theory, only radial stresses will be considered in this model and then all the circumferential stresses are neglected **[Sanchez 1999]**.

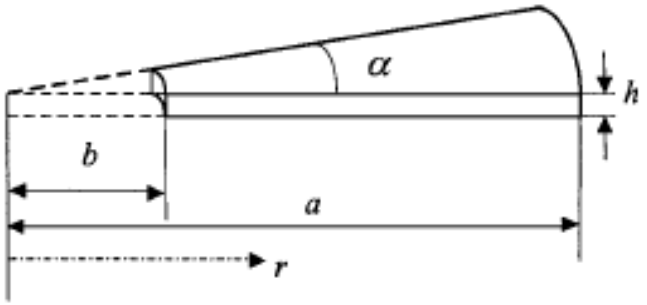

*Figure 3-7: Plate model as an assembly of taped beams **[Sanchez 1999]**.*

The moment of inertia of the cross-section of the beam varies with the radius as

$$I(r) = \frac{r\alpha h^3}{12} \tag{3-17}$$

The displacement w_0 at $r = b$ can be obtained by an unknown bending moment M_0 and an unknown point load F_0 applied at $r = b$.

The bending moment along the beam is given by

$$M(r) = -M_0 + F_0(r-b), \text{ with } b \le r \le a \tag{3-18}$$

And the curvature can be calculated as

$$w'' = \frac{M}{EI} = \frac{12}{E\alpha h^3}\left[-\frac{M_0}{r} + F_0(1-\frac{b}{r})\right] \tag{3-19}$$

The above differential equation can be solved using the boundary conditions: at $r = b$, $w = w_0$ and $w' = 0$. at $r = a$, $w = 0$ and $w' = 0$

Then we can obtain

$$w = \frac{2w_0}{(1+\lambda)\ln\lambda + 2(1-\lambda)}\left[(\ln r - 1)\frac{r}{a} + \frac{\ln\lambda}{2(1-\lambda)}\left(\frac{r}{a}\right)^2 - \frac{\ln(\lambda a^{1-\lambda})}{1-\lambda}\left(\frac{r}{a}\right) + \frac{\ln\lambda}{2(1-\lambda)} + 1\right] \tag{3-20}$$

where $\lambda = \frac{b}{a}$.

Then the curvature is given by

$$w'' = \frac{2w_0}{(1+\lambda)\ln\lambda + 2(1-\lambda)}\left[\frac{1}{ar} + \frac{\ln\lambda}{a^2(1-\lambda)}\right] \tag{3-21}$$

The elastic strain energy stored in the beam can be calculated from

$$U = \frac{E}{2}\int_b^a I(r)w''^2(r)dr \tag{3-22}$$

For a semi-circular plate, we can substitute equations (3-17) and (3-21) into equation (3-22)

$$U = \frac{D(1-\nu^2)\pi \cdot w_0^2}{a^2}F(\lambda) \tag{3-23}$$

where

$$F(\lambda) = \frac{2\ln\lambda + \frac{1+\lambda}{1-\lambda}\ln^2\lambda}{\left[(1+\lambda)\ln\lambda + 2(1-\lambda)\right]^2} \tag{3-24}$$

Then the energy release rate is given by

$$G = -\left(\frac{\partial U}{\partial A}\right)_{u_0} = -\frac{1}{\pi a}\left(\frac{\partial U}{\partial a}\right)_{u_0} = \frac{D(1-\nu^2)\cdot w_0^2}{a^4}(2F(\lambda)+\lambda F'(\lambda)) \qquad (3\text{-}25)$$

where

$$F'(\lambda) = \frac{dF}{d\lambda} = \frac{\frac{2}{\lambda}+\frac{2(1+\lambda)\ln\lambda}{(1-\lambda)\lambda}+\frac{\ln^2\lambda}{1-\lambda}+\frac{(1+\lambda)\ln^2\lambda}{(1-\lambda)^2}}{(2(1-\lambda)+(1+\lambda)\ln\lambda)^2} - \frac{2(-2+\frac{1+\lambda}{\lambda}+\ln\lambda)(2\ln\lambda+\frac{(1+\lambda)\ln^2\lambda}{1-\lambda})}{(2(1-\lambda)+(1+\lambda)\ln\lambda)^3} \qquad (3\text{-}26)$$

Figure 3-8 shows the function $2F(\lambda)+\lambda F'(\lambda)$ calculated by aspect ratio $\lambda = b/a$. For small value of λ, λ<0.1, the value of $2F(\lambda)+\lambda F'(\lambda)$ increases while λ increases, it means that the displacement w_0 at the central part of deflected film will decrease when λ increases. Figure 3-9 shows the condition in 0<λ<1. When λ=1, the value of the function $2F(\lambda)+\lambda F'(\lambda)$ diverges to very large values. If the energy release rate of interface is fixed then λ=1 will mean small displacement u_0, which makes measuring precise values of displacement difficult. The result of energy release rate cannot be accurately calculated from equation (3-25) due to the imprecise displacement measurement when λ is near 1.

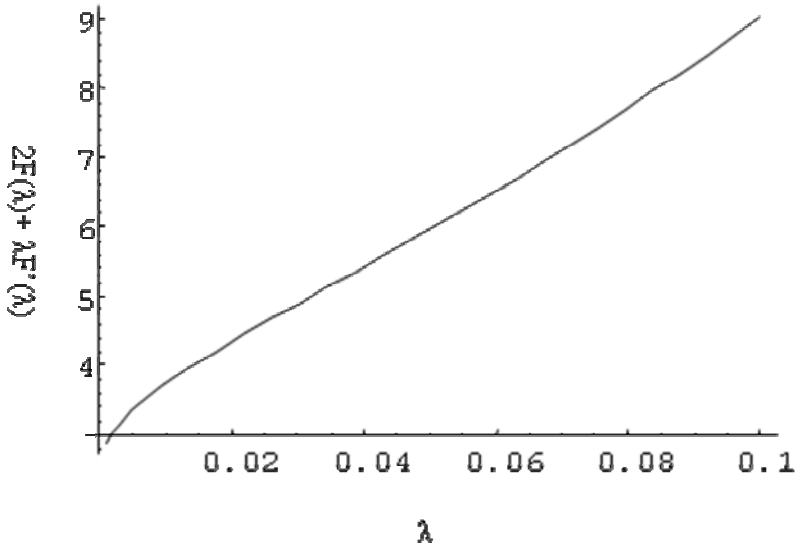

Figure 3-8: The function $2F(\lambda)+\lambda F'(\lambda)$ calculated for small aspect ratio $\lambda = b/a$ (λ<0.1).

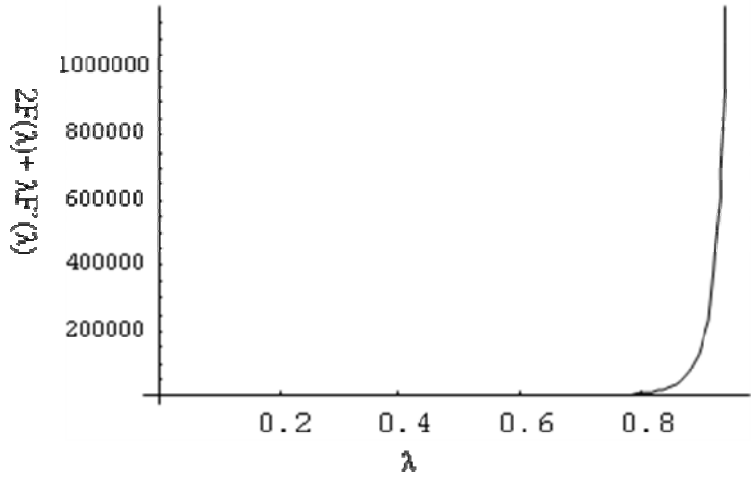

Figure 3-9: The function $2F(\lambda)+\lambda F'(\lambda)$ *calculated for aspect ratio* $\lambda = b/a$ *(λ<1).*

The energy release rate can be given by another form; the elastic strain energy stored in the beam could be directly differentiated with regards to *a*.

$$G = -\frac{1}{\pi a}\left(\frac{\partial U}{\partial a}\right)_{u_0} = -D(1-\nu^2)\cdot w_0^2\left(\frac{1}{a}\left(\frac{\partial U}{\partial a}\right)_{u_0}\right) = D(1-\nu^2)\cdot w_0^2 F(a,b) \qquad (3\text{-}27)$$

Figure 3-10 shows the function *F (a, b)* at assumed indentation size *b* and crack length *a* (both in meter). If the vertical displacement w_0 or indentation size *b* is fixed, it is obvious that the energy release rate of the interfacial cracks decrease with the increase of crack length.

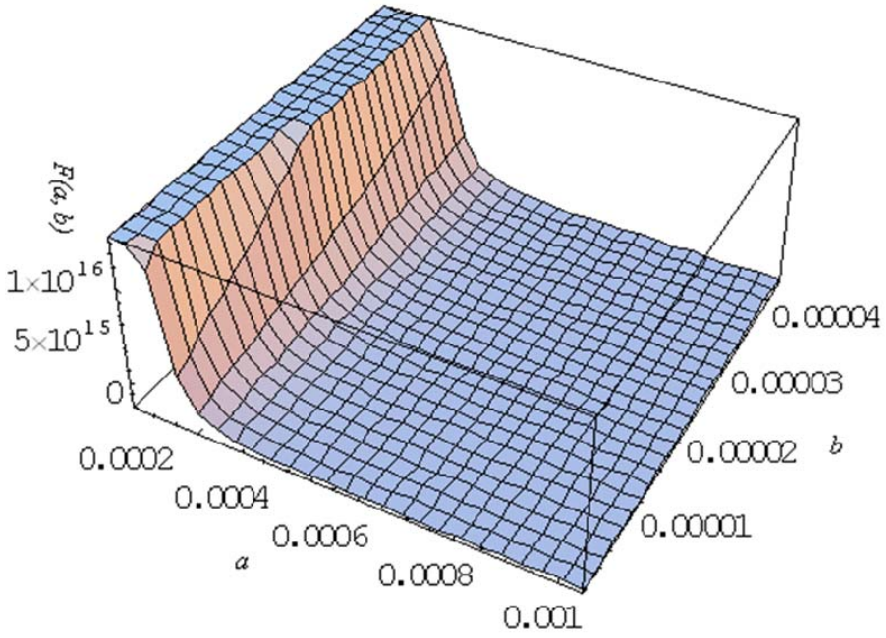

Figure 3-10: The relationship of function F(a, b) and indentation size b and crack length a (both in meter).

3.3.3. The model of an elastic plate with elastically restrained edges

The interfacial adhesion is not only dependent on the material properties of the film but also the material properties of the substrate. Li proposed recently a novel theoretical model of the CSN technique **[Li 2006]**. The interface debonding between a thin film and an elastic substrate is modeled as the elastic bending of an elastic plate with elastically restrained edges, and the influence of the elastic substrate is described by two elastic constants K_1 and K_2 (Figure 3-11).

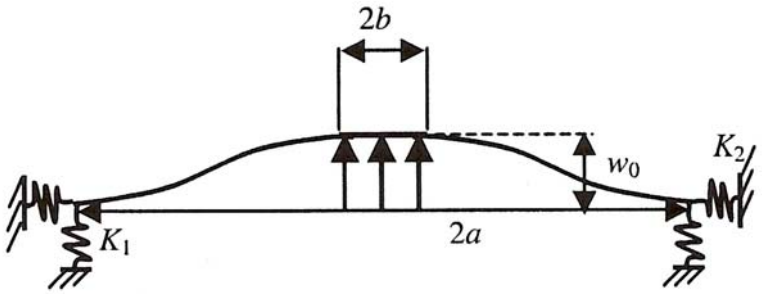

Figure 3-11: The model of an elastic plate with elastically restrained edges ***[Li 2006].***

The boundary conditions at the inner edge are

$$w(b) = w_0, \qquad \left.\frac{dw}{dr}\right|_{r=b} = 0.$$

An assumption is made that the bonding between the thin film and the substrate is perfect. Consequently, the influence of the elastic substrate on the interfacial adhesion cannot be completely neglected; the following elastically supported boundary conditions are adopted at the outer edge

$$D\frac{d}{dr}\left(\frac{d^2w}{dr^2}+\frac{1}{r}\frac{dw}{dr}\right)\Bigg|_{r=a} = K_1 w|_{r=a}.$$

$$D\frac{d}{dr}\left(\frac{d^2w}{dr^2}+\frac{\nu}{r}\frac{dw}{dr}\right)\Bigg|_{r=a} = -K_2\left.\frac{dw}{dr}\right|_{r=a}. \tag{3-28}$$

K_1 and K_2 are the translational and rotational flexibility parameters, the dimensions of which are N/m^2 and N respectively. If K_1 and K_2 tend to infinity, the above boundary conditions reduce to

$$w(a) = 0, \qquad \left.\frac{dw}{dr}\right|_{r=a} = 0.$$

For a one-dimensional bending beam, the basic governing equation is equation (3-19)

$$w''(r) = \frac{M(r)}{EI(r)} \tag{3-19}$$

By inserting the boundary conditions at $r=b$ and conditions at $r=a$ into equation (3-19), a closed form of deflection can be obtained as

$$w = \frac{2w_0}{(1+\lambda)\ln\lambda + 2(1-\lambda)}\left[\frac{\ln\lambda}{2(1-\lambda)}\left(\frac{r}{a}\right)^2 + \frac{r}{a}\left(\ln\frac{r}{a} - 1\right) - \frac{\ln\lambda}{(1-\lambda)}\left(\frac{r}{a}\right) + \frac{\ln\lambda}{2(1-\lambda)} + 1\right] \tag{3-29}$$

According to the bending theory of elastic plate, the transverse deflection of the elastic plate, w, obeys the following differential equation

$$\left(\nabla^2\right)^2 w = 0 \tag{3-30}$$

where ∇ is the two-dimensional Laplace operator and a general solution is readily found to be

$$w = A_0\left(\frac{r}{a}\right)^2 \ln\frac{r}{a} + B_0\left(\frac{r}{a}\right)^2 + C_0\left(\frac{r}{a}\right) + D_0 \tag{3-31}$$

where A_0, B_0, C_0 and D_0 are unknown and need to be determined. To substitute the above general solution into the given four boundary conditions leads to

$$w_0 = A_0\lambda^2 \ln\lambda + B_0(\lambda)^2 + C_0(\lambda) + D_0$$

$$A_0(2\lambda\ln\lambda + \lambda) + 2B_0(\lambda) + C_0 = 0$$

$$4K_1A_0 - B_0 - (K_1+1)C_0 - D_0 = 0$$

$$\left[K_2(3+\nu)+1\right]A_0 + 2\left[K_2(1+\nu)+1\right]B_0 + (K_2\nu+1)C_0 = 0 \tag{3-32}$$

This set of linear algebraic equation can be solved for the values of A_0, B_0, C_0, D_0 according to the classical mathematical procedure. When $K_1, K_2 \to \infty$

$$A_0 = \frac{2}{1-\lambda^2+2\lambda\ln\lambda}$$

$$B_0 = -\frac{1-\lambda-2\lambda\ln\lambda}{(1-\lambda)(1-\lambda^2+2\lambda\ln\lambda)}$$

$$C_0 = -\frac{4\lambda \ln \lambda}{(1-\lambda)(1-\lambda^2+2\lambda \ln \lambda)}$$
$$D_0 = \frac{1-\lambda+2\lambda \ln \lambda}{(1-\lambda)(1-\lambda^2+2\lambda \ln \lambda)} \tag{3-33}$$

The energy release rate for the interface crack propagation can be determined by,

$$G = -\left(\frac{\partial U}{\partial A}\right)_{w_0} \tag{3-13}$$

The stored energy can be expressed in terms of the transverse deflection w as follows

$$U = \frac{1}{2}\left\{\frac{\pi D}{2}\int_b^a \left[(w'')^2 + 2\nu r^{-1} w'' w' + (r^{-1}w')^2\right] r dr + \frac{\pi a}{2} K_1 w(a)^2 + \frac{\pi a}{2} K_2 w'(a)^2\right\} \tag{3-34}$$

To substitute the result of w in equation (3-33) into equation (3-34), and after some algebra we can get

$$U = \frac{4\pi D w_0^2}{a^2} F(\lambda) \tag{3-35}$$

For the case of an elastic plate with clamped edges, the energy release rate is given by

$$G = -\frac{1}{\pi a}\left(\frac{\partial U}{\partial a}\right)_{w_0} = \frac{4 D w_0^2}{a^4}(2F(\lambda) + \lambda F'(\lambda)) \tag{3-36}$$

where

$$F(\lambda) = \frac{1-\lambda^2+4\lambda \ln \lambda - \dfrac{2\lambda^2 \ln^3 \lambda}{(1-\lambda)^2}}{\left[1-\lambda^2+2\lambda \ln \lambda\right]^2}, \text{ and}$$

$$F'(\lambda) = \frac{4-2\lambda+4\ln\lambda - \dfrac{6\lambda \ln^2 \lambda}{(1-\lambda)^2} - \dfrac{4\lambda \ln^3 \lambda}{(1-\lambda)^2} - \dfrac{4\lambda^2 \ln^3 \lambda}{(1-\lambda)^3}}{\left[1-\lambda^2+2\lambda \ln \lambda\right]^2}$$
$$- \frac{2(2-2\lambda+2\ln\lambda)(1-\lambda^2+4\lambda \ln \lambda - \dfrac{2\lambda^2 \ln^3 \lambda}{(1-\lambda)^2})}{\left[1-\lambda^2+2\lambda \ln \lambda\right]^3}$$

Figure 3-12 and 3-13 show the function $2F(\lambda)+\lambda F'(\lambda)$ calculated versus aspect ratio $\lambda = b/a$. Figure 3-14 shows the relationship of function *F(a, b)* and indentation size *b* and crack length *a* (both in meter). All figures demonstrate the same trend as for tapered beams model. We can observe that the energy release rate calculated by elastically restrained edges model will be equivalent to the one obtained by plate model as λ approaches zero. While $\lambda \to 1$, the G_c will be thousand times larger than G_c obtained by plate model.

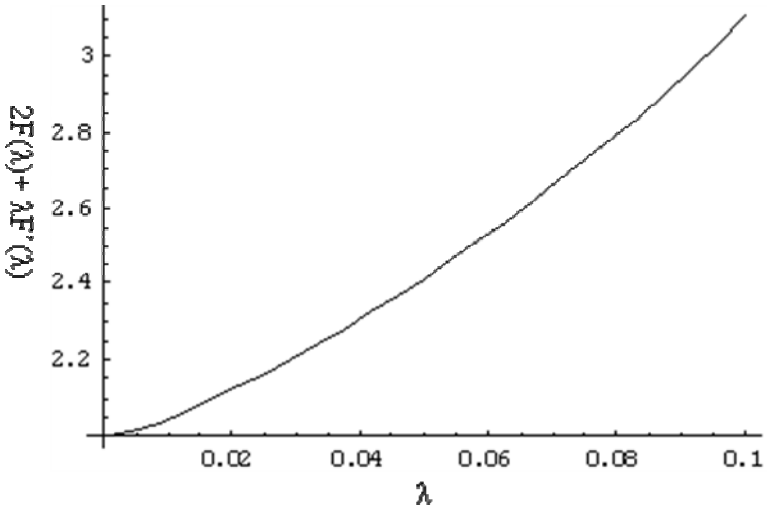

Figure 3-12: The function $2F(\lambda)+\lambda F'(\lambda)$ calculated for small aspect ratio $\lambda = b/a$ (elastically restrained edges model).

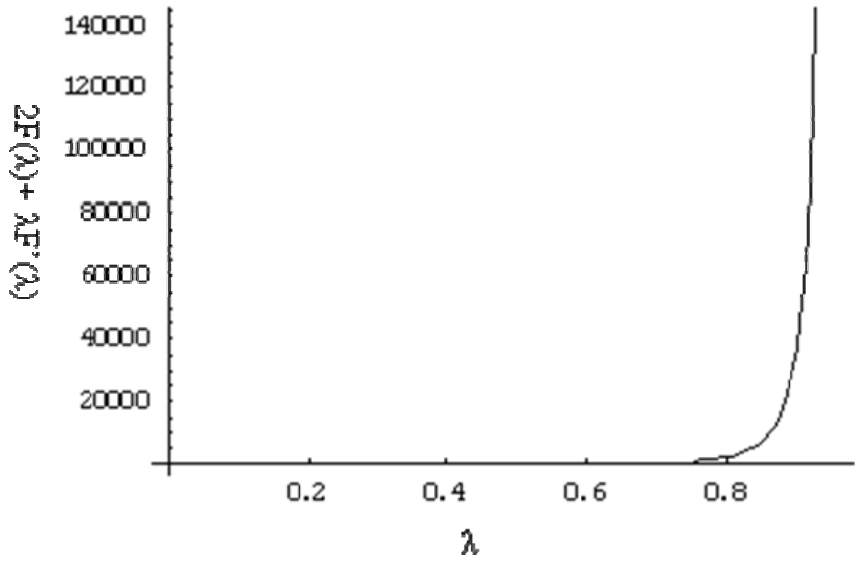

Figure 3-13: The function $2F(\lambda)+\lambda F'(\lambda)$ calculated for aspect ratio $\lambda = b/a$ (elastically restrained edges model).

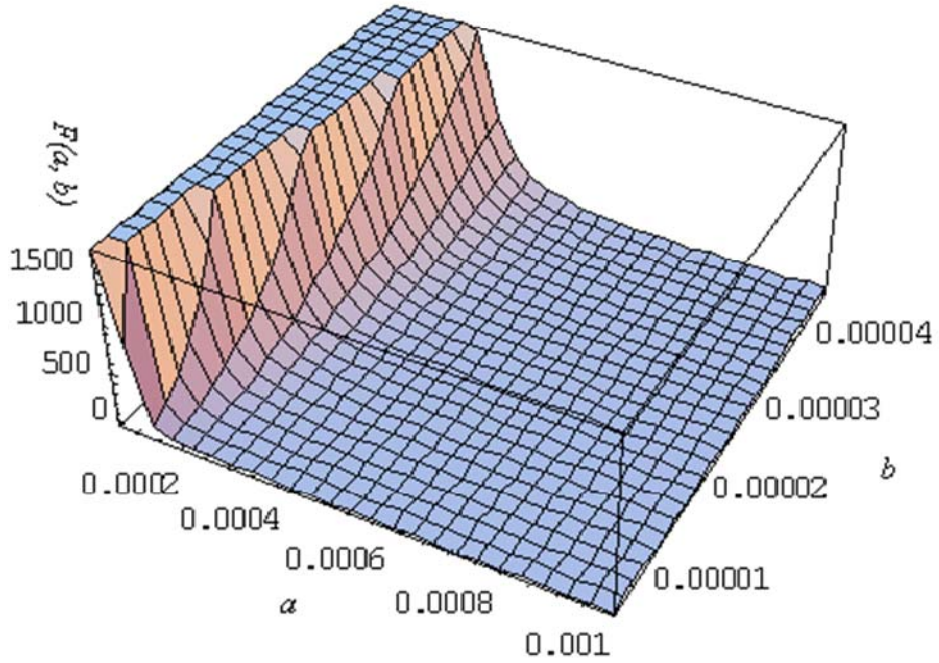

Figure 3-14: The relationship of function F(a, b) and indentation size b and crack length a (both in meter) (elastically restrained edges model).

To compare the elastically restrained edges model with tapered beams model, Figure 3-15 gives a comparison of their resultss. G1 means the interfacial energy release rate of elastically restrained edges model and G2 comes from tapered beams model with Poisson's ratio equal to 0.3. The result express by equation (3-36) dividing equation (3-25) gives $(1-\nu^2)/8$ when $\lambda \to 1$, dependent on the Poisson's ration.

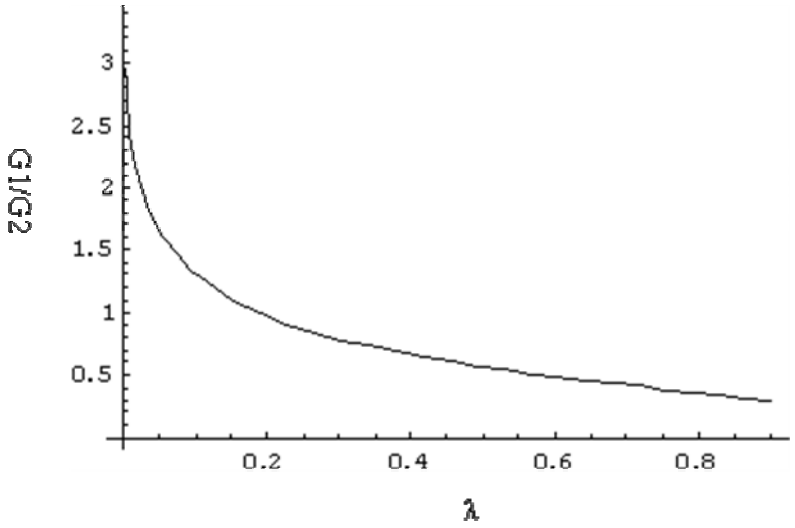

Figure 3-15: Comparison of energy release rate calculated by elastically restrained edges model and tapered beams model.

3.3.4. Point load model

We propose a new model by considering the applied force. For an isotropic film and substrate, the debond zone is semi-circular in cross-sectional indentation test. If indentation size b is small, we can assume that $a\text{-}b \approx a$. since b is small so we can suppose that film separates from substrate by a point load P. Point load comes from indent force F and can be expressed as

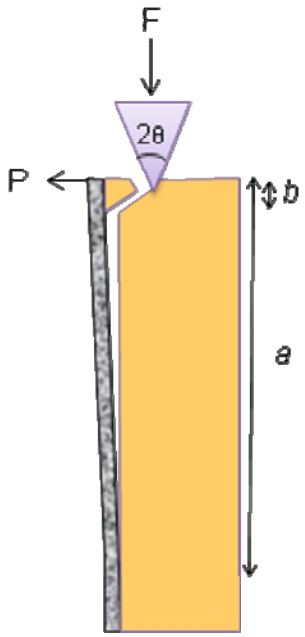

$$P = F\cos\theta\sin\theta \tag{3-37}$$

A simple theory, valid for small deflections w_0 of a thin plate, gives the energy release rate G for the interface crack

$$G = \frac{Pw_0}{2\pi a^2} \tag{3-38}$$

for a point load circular blister **[Jensen 1991]**. It is assumed that the debond zone has spread out several times the thickness. For thick coating, the deflection w_0 is usually smaller than coating thickness t in cross-sectional indentation test. Therefore, interfacial energy release rate for semi-circular can be expressed as

$$G = \frac{F\cos\theta\sin\theta w_0}{\pi a^2} \tag{3-39}$$

For Vickers indentation the angle θ is 68^0.

4. Mode mixity of cross-sectional indentation test

The mode mixity of cross-sectional indentation test is discussed in this section. A measure of the mode mixity at the crack tip is defined as (2-58)

$$\tan(\psi) = \frac{\sqrt{12}M\cos\omega + tN\sin\omega}{-\sqrt{12}M\sin\omega + tN\cos\omega}$$

where ω is phase factor concerning the Dundur's elastic mismatch parameters α and β. Most interfaces have $\beta=0$ or $\beta=\alpha/4$ as a good approximation. The variation of $\omega(\alpha, \beta)$ is shown in Figure 3-16 for $\beta=0$ or $\beta=\alpha/4$ using the results of ref. **[Hutchinson 1992]**. The values of ω in most case of interest is $45^o<\omega<65^o$ **[Suo 1990].**

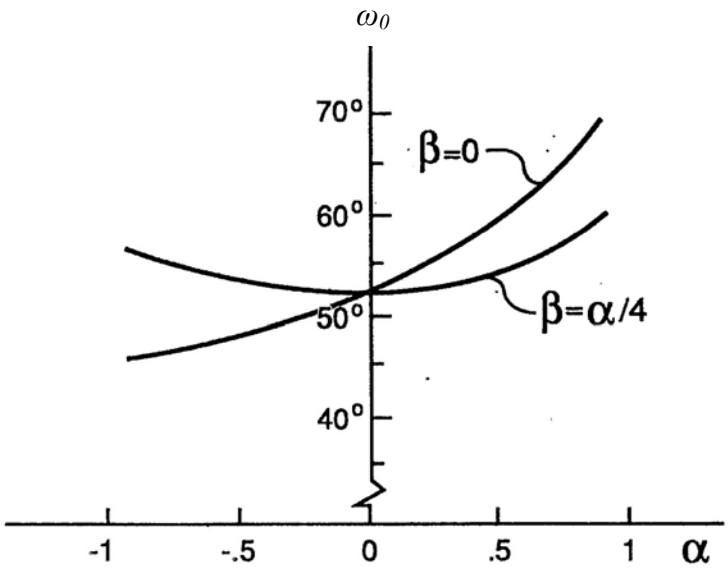

Figure 3-16: The variation of ω(α, β) for β=0 or β=α/4 ***[Hutchinson 1992]***.

In this study we focus on the thick metal coatings attached on oxide substrate. Due to the poor adhesion of metal/oxide interface, the thick metal film can be supposed to be elastic (except for possible confined plasticity at the crack point); we can assume that the film deflection will be smaller than film thickness ($w_0<t$) as seen during experiment (chapter 5). Another assumption is that indent size b is much smaller than crack length a ($a>>b$), so the force to separate the membrane can be regarded as a point load. For small deflection in cross-sectional indentation test, the membrane stress N can be assumed as 0 for point load perpendicular to the membrane. The mode mixity parameter is expressed in the form

$$\tan(\psi) = -\cot\omega \Rightarrow \psi = -(\frac{\pi}{2} - \omega) \qquad (3\text{-}40)$$

As we mentioned before, the values of ω is between 45° to 65^o, the mode mixity for small deflection ($w_0<<t$) of cross-sectional indentation test can be calculated from equation (3-40) and be from 25° to 45°.

For small indent size b, the assumption to regard it as a point load is acceptable. When the ratio b/a increases, the mode mixity of cross-sectional indentation test will need more study to be understood. Figure 3-17 gives the mode mixity of interface crack tip for several levels of elastic mismatch for a blister under a point load.

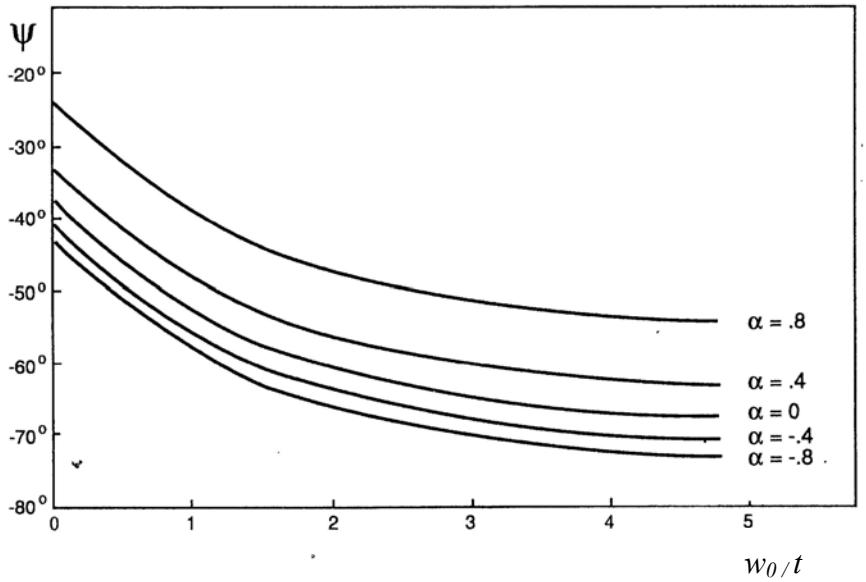

Figure 3-17: the mode mixity of interface crack tip for several levels of elastic mismatch for a blister under a point load ***[Hutchinson 1992]****.*

5. Conclusions

The interfacial adhesion and debonding between a film and a substrate can be analyzed by using indentation test. Three indentation tests for measuring interface adhesion strength are introduced in this chapter. Normal indentation test is commonly used in thin film/substrate system by using nanoindentation; the difficulty in analyzing normal indentation test is that both elastic and plastic deformation fields are produced by indentation. Interface indentation test meets some theoretical and experimental difficulties; the accuracy of this technique is not correctly defined. Cross-sectional indentation test comes from Cross-Sectional Nano-indentation (CSN) test. The theoretical analysis of CSN is almost completed; we can simply apply CSN models into cross-sectional indentation test with larger loads for energy release rate calculation. Cross-sectional indentation test is a new and developing technique of adhesion strength measurement; it seems to be an appropriate technique to measure metal/oxide interface adhesion.

References

[Anstis 1981] G. R. Anstis, P. Chantikul, B. R. Lawn, D. B. Marshall, "*A critical evaluation of indentation technique for measuring fracture toughness: I. Direct crack measurements*" Journal of the American Ceramic Society, Vol. 64, No. 9, (1981) pp.533-538.

[Bull 2005] S. J. Bull, "*Nanoindentation of coatings*" Journal of Physics D: Applied Physics, 38 (2005) pp.393-413.

[Chantikul 1981] P. Chantikul, G. R. Anstis, B. R. Lawn, D. B. Marshall, "*A critical evaluation of indentation technique for measuring fracture toughness: II. Strength method*" Journal of the American Ceramic Society, Vol. 64, No. 9, (1981) pp.539-543.

[Chan 2006] K. S. Chan, H. Ji, X. Wang, S. J. Hudak Jr, B. R. Lanning, "*Mechanical properties and interface toughness of FeCo thin films on Ti-6Al-4V*" Materials Science and engineering A, 422 (2006) pp.298-308.

[Chicot 1996] D. Chicot, P. Demarecaux, J. Lesage "*Apparent interface toughness of substrate and coating couples from indentation tests*" Thin Solid Films, 283 (1996) pp.151-157.

[Choulier 1998] D. Choulier, "*Contribution à l'étude de l'adhérence de revetements projetés à la torche à plasma. Modélisation et utilisation d'un test d'indentation à l'interface*" Thése de doctorat, Université de Technologie de Compiégne (1998).

[Demarecaux 1996] P. Demarecaux, D. Chicot, J. Lesage, "I*nterface indentation test for the determination of adhesive properties of thermal sprayed coatings*" Journal of Materials Science Letters, 15 (1996) pp.1377-1380.

[Engle 1983] P. A. Engle, G. C. Pedroza, "*Indentation-debonding test for adhered thin polymer layers*" Adhesion Aspects of Polymeric Coatings, K. L. Mittal, Ed. (Plenum Press, New York, 1983) pp.583.

[Elizalde 2003] M. R. Elizalde, J. M. Sanchez, J. M. Martinez-Esnaola, D. Pantuso, T. Scherban, B. Sun, G. Xu, "*Interfacial fracture induced by cross-sectional nanoindentation in metal-ceramic thin film structures*" Acta Materialia, 51, (2003) pp.4295-4305.

[Hutchinson 1992] J.W. Hutchinson, Z. Suo, "*Mixed mode cracking in layer materials*" Advances in Applied Mechanics, 29 (1992) pp.63-191.

[Jensen 1991] H. M. Jensen, "*The blister test for interface toughness measurement*", Engineering Fracture Mechanics, Vol. 40, no. 3, (1991) pp. 475-486.

[Latella 2002] B. A. Latella, T. W. Nicholles, D. J. Cassidy, C. J. Barbé, G. Triani, "*Evaluation of interfacial toughness and bond strength of sandwiched silicon structure*" Thin Solid Films, 411 (2002) pp.247-255.

[Lesage 1993] J. Lesage, P. Demarecaux, O. Bartier, G. Mesmacque, "*détermination de l'adhérence par le test d'indentation interfaciale*" La Revue de métallurgie-CIT/Science et Génie des matériaux, (1993) pp.1655-1663.

[Lesage 1999] J. Lesage, D. Chicot, D. Judas, M. Zampronio, P. Araujo, P. E. V. de Miranda, "*Mesures par indentation interfaciale de l'adhérence de revetements NiCr projetés thermiquement*" Matériaux et Techniques, 9-10 (1999) pp.29-34.

[Lesage 2001] J. Lesage, D. Chicot, "*Hardness and adhesion of coating*" Revista de la Facultad de Ingenieria de la U.C.V., Vol. 16, No. 1 (2001) pp.33-38.

[Li 2006] X. F. Li, "*Effects of an elastic substrate on the interfacial adhesion of thin films*" Surface and Coatings Technology, 200 (2006) pp.5003-5008.

[Marshall 1984] D. B. Marshall, A.G. Evans, "*Measurement of adhesion of residually stressed thin films by indentation. I. Mechanics of interface delamination*" Journal of Applied Physics, 56(10) (1984) pp.2632-2638.

[Molina 2007] J. M. Molina-Aldareguia, I. Ocana, D. Gonzalez, M. R. Elizalde, J. M. Sanchez, J. M. Martinez-Esnaola, J. Gil-Sevillano, T. Scherban, D. Pantuso, B. Sun, G. Xu, B. Miner, J. He, J. Maiz, "*Adhesion studies in integrated circuit interconnect structures*" Engineering Failure Analysis, 14 (2007) pp.349–354.

[Ocana 2006] I. Ocana, J. M. Molina-Aldareguia, D. Gonzalez, M. R. Elizalde, J. M. Sanchez, J. M. Martinez-Esnaola, J. Gil Sevillano, T. Scherban, D. Pantuso, B. Sun, G. Xu, B. Miner, J. He, J. Maiz, "*Fracture characterization in patterned thin films by cross-sectional nanoindentation*" Acta Materialia, 54 (2006) 3453–3462.

[Qi 2003] Y. H. Qi, P. Bruckel, P. Lours, "*Interfacial toughness of the nickel-nickel oxide system*" Journal of Materials Science Letters, 22 (2003) pp.371-374.

[Richard 1996] C. S. Richard, G. Béranger, J. Lu, J. F. Flavenot, "*The influences of heat treatments and interdiffusion on the adhesion of plasma-sprayed NiCrAlY coatings*" Surface and Coating Technology, 82 (1996) pp. 99-109.

[Roy 2006] S. Roy, E. Darque-Ceretti, E. Felder, H. Monchoix, "*Mesure de l'adhérence de couches minces de la microélectronique par nanoindentation sur coupe et nano-rayure*" Communication au colloque, Féderation Française des matériaux Dijon (France) 13-17 Nov. 2006.

[Sanchez 1999] J. M. Sanchez, S. El-Mansy, B. Sun, T. Scherban, N. Fang, D. Pantuso, W. Ford, M. R. Elizalde, J. M. Martinez-Esnaola, A. Martin-Meizoso, J. Gil-Sevillano, M. Fuentes, J. Maiz. "*Cross-sectional nanoindentation: a new technique for thin film interfacial adhesion characterization*" Acta Materialia, 47, (1999) pp.4405-4413.

[Scherban 2003] T. Scherban, D. Pantuso, B. Sun, S. El-Mansy, J. Xu, M. R. Elizalde, J. M. Sanchez, J. M. Martinez-Esnaola, "*Characterization of interconnect interfacial adhesion by cross-sectional nanoindentatioin*" International Journal of Fracture, 119/120 (2003) pp.421-429.

[Suo 1990] Z. Suo, and J.W. Hutchinson, "*Interface crack between two elastic layers*" International Journal of Fracture, 43, (1990) pp.1-18.

[Toonder 2002] J. der Toonder, J. Malzbender, G. de With, R. Balkenende, "*Fracture toughness and adhesion energy of sol-gel coatings on glass*" Journal of Materials Research, 17 (2002) pp.224-233.

[Volinsky 2002] A. A. Volinsky, N. R. Moody, W. W. Gerberich, "*Interfacial toughness measurements for thin films on substrates*" Acta Materialia, 50 (2002) pp.441–466.

[Zhang 1994] J. Zhang, J. J. Lewandowski, "*Interfacial fracture toughness measurement using indentation*" Journal of Materials Science, 29 (1994) pp.4022-4026

[Zhen 2004] X. J. Zheng, S. F. Deng, Y. C. Zhou, X. Tan, P. Jiang, "*Plate model to evaluate interfacial adhesion of anisotropy thin film in CSN test*" Journal of Materials Science Letters, 39 (2004) pp.4013-4016.

[Zhen 2005] X. J. Zheng, Y. C. Zhou, "*Investigation of an anisotropic plate model to evaluate the interface adhesion of thin film with cross-sectional nanoindentation method* " Composites Science and Technology, 65 (2005) 1382–1390.

Chapter Ⅳ

Experiments

1. Materials 81

1.1. Barium Titanate 81
1.2. Metals 82

2. Blister test 84

2.1. Blister test apparatus 84
2.1.1. Sample mounting 85
2.1.2. Data acquisition system 86
2.1.3. Theory of fringe projection method: 88
2.2. Sample preparation for Blister test 93
2.2.1. Silver (Ag)/Barium Titanate ($BaTiO_3$) 93
2.2.2. Nickel (Ni)/Barium Titanate ($BaTiO_3$) 96
2.2.3. Nickel (Ni)/Silver (Ag)/ Barium Titanate ($BaTiO_3$) 97
2.2.4. Silver (Ag)/Nickel (Ni) 98

3. Indentation test 98

3.1. Indentation test apparatus 98
3.2. Sample preparation for indentation test 98
3.2.1 Interface and cross-sectional indentation test 98
3.2.2 Normal indentation test 99

4. Conclusions 100

References 101

1. Materials

The metal/ceramic laminates are employed in many electronic components to increase their volume efficiency, such as multilayer ceramic capacitors (MLCC). Ceramic laminates and electrode films are stacked mutually to form a laminated construction. Barium titanate is the most used dielectric material in MLCC because of its high dielectric constant and the electrode materials are usually silver (Ag), nickel (Ni), palladium (Pd) or Ag/Pd alloys. Therefore, we employ silver, nickel and barium titanate as material systems in this investigation. Some intrinsic properties of those materials are listed in Table 4-1.

Table 4-1: The intrinsic properties of the materials used in this study.

	$BaTiO_3$	Ag	Ni
Crystal structure	Tetragonal	Face Centred Cubic	Face Centred Cubic
Density ($g.cm^{-3}$)	6.02	10.49	8.88
Modulus of Elasticity (GPa)	178	76	207
Poisson Ratio	0.25-0.35	0.367	0.312
Shear Modulus (GPa)		27.8	76
Melting point (℃)	1650	961.9	1453

1.1. Barium Titanate

The raw material for oxide substrate is the powder of Barium Titanate made by FERRO Corporation, U.S.A. (series number: 52909.). The purity of the $BaTiO_3$ powder is higher than 99.6% and the average particle size is 1.1 μm. The basic information and compositions of the $BaTiO_3$ powder are shown in Table 4-2. Figure 4-1 shows the phase diagram of BaO/TiO_2.

Table 4-2: The characteristics of $BaTiO_3$ powder used in the present study.

$BaTiO_3$	TICON NEB 52909 FERRO Corporation, U.S.A.
BaO/TiO_2	1.000±0.002
Crystal Form	Tetragonal
BET (m^2/g)	3.0
Density (g/cm^3)	6.02
Particle size D50(μm)	1.1

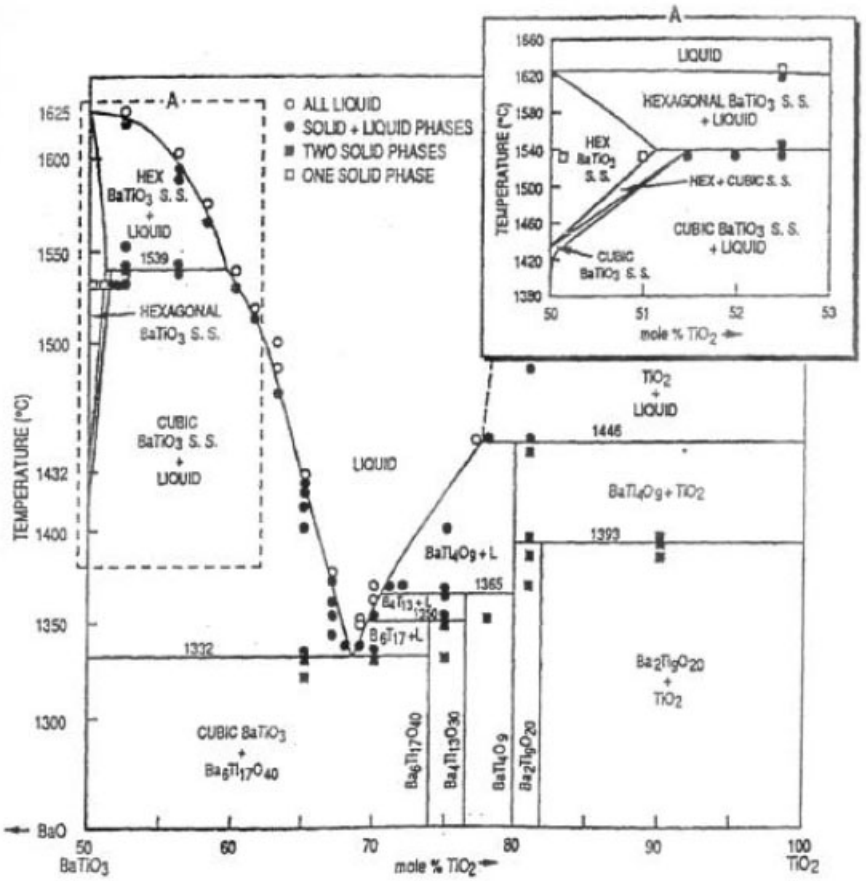

Figure 4-1:The phase diagram of BaO/TiO_2.

1.2. Metals

The raw materials for metal membrane are the powder of silver made by FERRO Corporation, U.S.A. (series number: C200ED) and the powder of nickel (UMP 0600, Umicore Canada Inc.). The basic information and compositions of the metal powder are shown in Table 4-3 and 4-4. Figure 4-2, 4-3, 4-4 are the phase diagrams of Ag/O, Ni/O and Ag/Ni.

Table 4-3: The characteristics of silver powder used in the present study.

Ag powder	C200ED FERRO Corporation, U.S.A.
Crystal Form	Face Centred Cubic
BET (m^2/g)	0.76
Particle size (μm)	1.05
Tap density (g/cm^3)	3.2
Lost at 538℃ in air (%)	0.65

Table 4-4: The characteristics of nickel powder used in the present study.

Ni powder	UMP 0600 Umicore Canada Inc.
Crystal Form	Face Centred Cubic
BET (m^2/g)	1.3
Particle size (μm)	1.3
Tap density (g/cm^3)	3.4

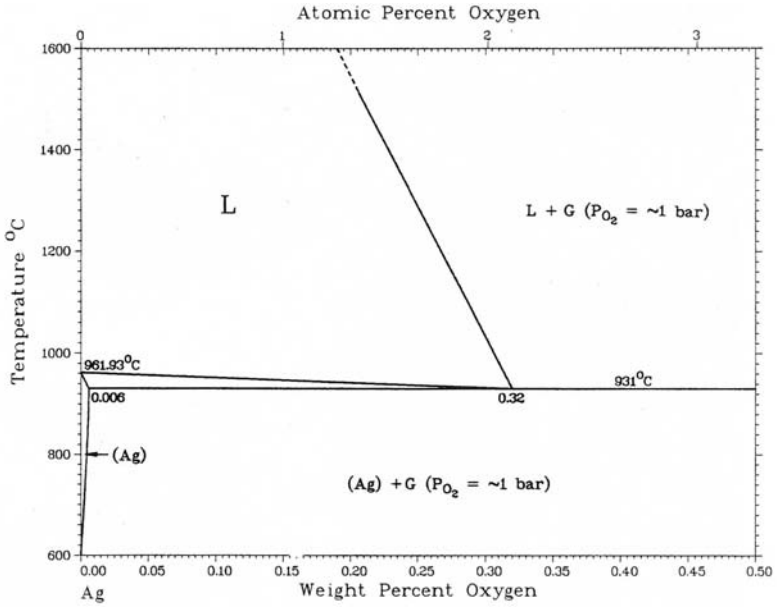

Figure 4-2: The phase diagram of Ag/O[1]

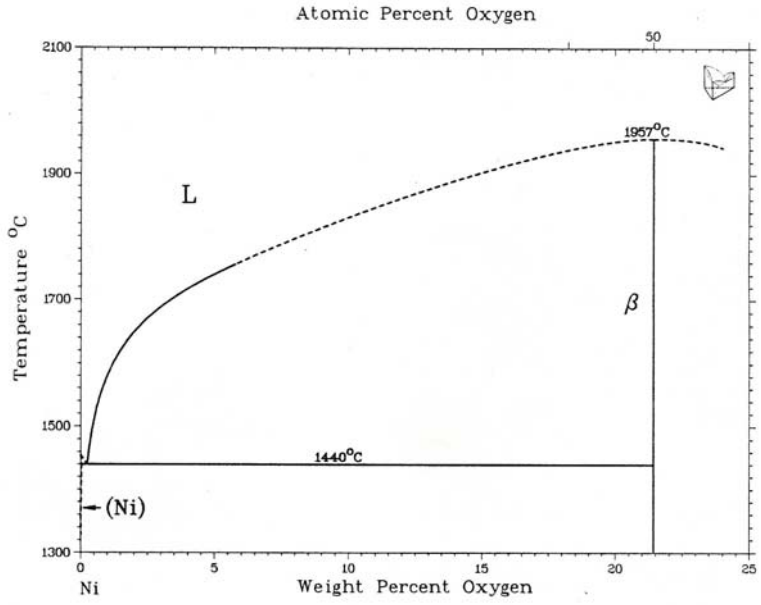

Figure 4-3: The phase diagram of Ni/O[2]

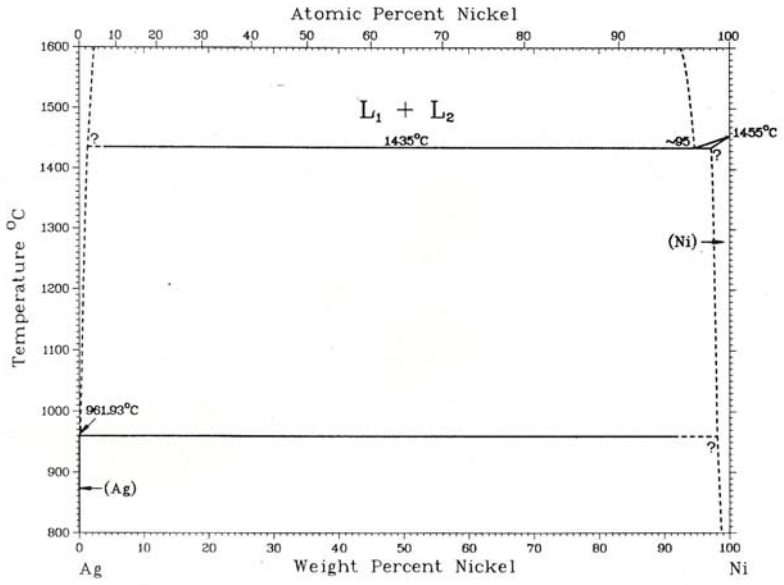

Figure 4-4: The phase diagram of AgNi

2. Blister test

2.1. Blister test apparatus

The basic layout of the apparatus we used for blister test consists of a quadrilateral metal block, in which holes and four components are located: sample mounting fixture, pressure sensors, syringe pump and piston for manual pressurizing.

We use metal as the body of the apparatus because of its rigid characteristic. The basic layout is described in Figure 4-5 and 4-6.

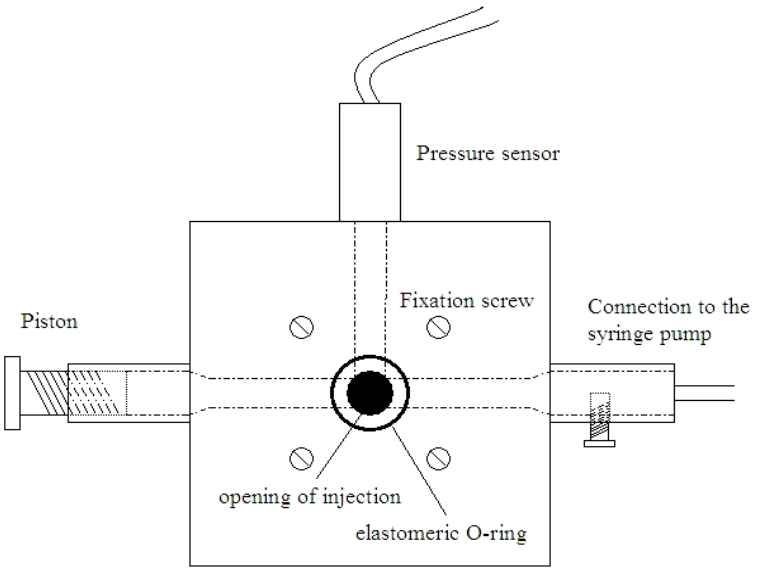

Figure 4-5: blister test apparatus

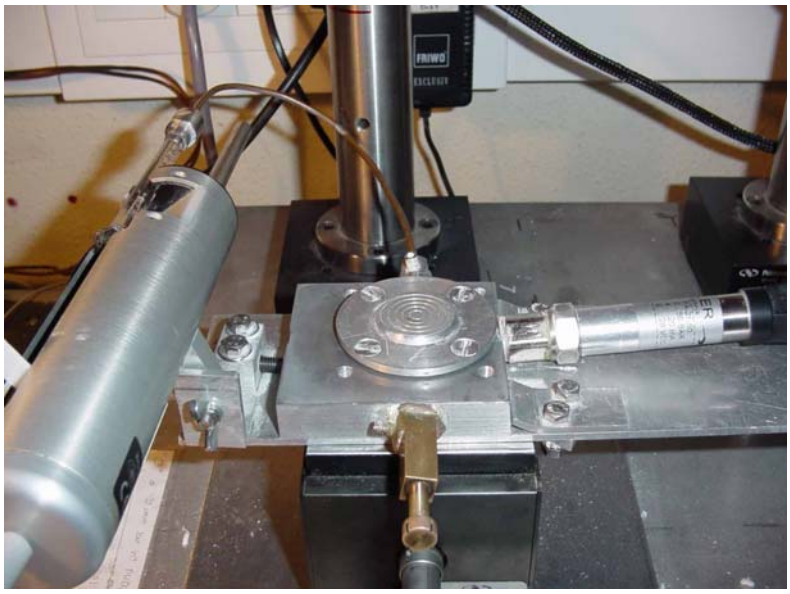

Figure 4-6: Photograph of the blister apparatus.

2.1.1. Sample mounting

A frustum of a cone made of metal is used as the direct support on which the sample is glued. A hole drilled through the axis of the support allows liquid to pressurize the sample. We use a metallic ring and four screws around the ring to fix the support to the apparatus. The injection opening in the block is surrounded by an elastomeric O-ring in order to ensure the sealing between the block and the support. Sample mounting is depicted in Figure 4-7.

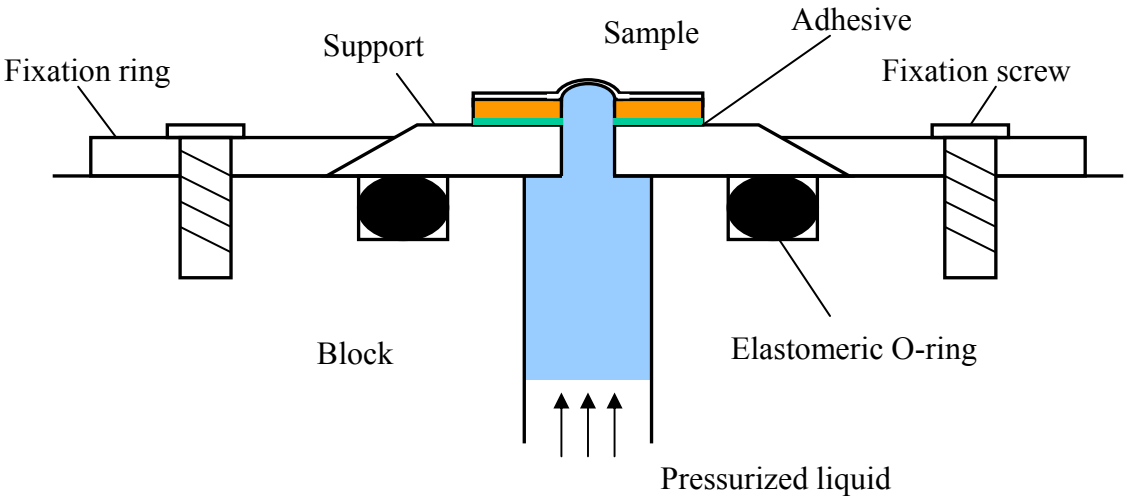

Figure 4-7: Sample mounting

A pressure sensor (Keller, type: PA-21-50, output: 4-20mA, power supply: 8-28VDC) is used to acquire the relative pressure, which ranges between 0-50 bars with 1% resolution.

A piston is made of a waterproof micrometer screw, which permits us to relieve the pressure as samples are bonded and de-bonded. We can also control the injection by rotating the screw to pressurize or to release the pressure.

The syringe pump is more accurate than the manual system as a pressurizing system with a constant injection rate. However, in our case, because the blister takes place within a very short time, the syringe pump seems unable to release the pressure promptly, which may cause the film to break, moreover, the fluid injection rate is unlikely to have a strong influence on our research. Therefore, we used manual system to pressurize the fluids.

2.1.2. Data acquisition system

There are several requirements for the system of to measure the deformation during the blistering: precise, non-contact, rapid and able to measure both the altitude and the diameter of the blister, which grows from the substrate surface. In general, the laser interferometer is an equipment frequently used to measure the displacement in bulge and blister test **[Hsu 2002, Wang 1999, Taheri 2000]**. In this study we used an other technique: fringe projection method.

A laser beam is separated in two beams, which are combined to produce a set of parallel interference fringes. These two projected, under a certain angle, on the top of the blister apparatus. The laser source is a 20.18 mW diode laser with a wavelength of 673.5nm (Laser 2000 S.A., model: DLSC-500-685-30).

A CCD camera (Charge Coupled Device camera, Sony XC-75, resolution: 768x498) is fixed above the blister apparatus to take a top view of the image of the fringes on the specimen surface, which will be analyzed by a computer.

The image is transmitted from CCD camera to the photo-detector (Matrox, Frame grabber), which can detect the images instantaneously and translate it into the digital signal. Then the photo-detector pass the image signal to the data acquisition board. Finally, the software (HOLO 3: Fringe Analysis ®) is used to analyze the results. The system is illustrated in Figure 4-8.

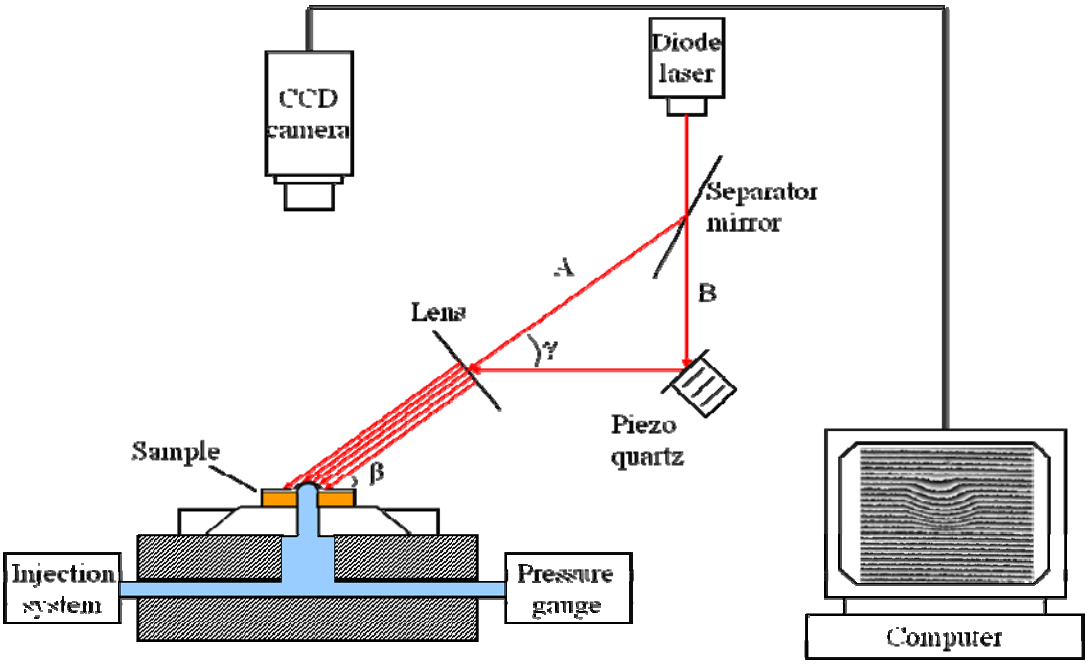

Figure 4-8: Illustration of the complete blister system

The main purpose of the equipment for data acquisition is to control the tests and record data, which are analyzed after the tests. Two major data are the film maximum deflection for each value of pressure, to obtain the interfacial energy release rate. Figure 4-9 shows the photograph of the complete system.

Figure 4-9: Photograph of the complete blister system

2.1.3. Theory of fringe projection method:

The parallel laser beams interference fringes are projected on the sample under a certain angle. If the surface of the sample is flat, the fringes observed from the top are parallel and equidistant (See Figure 4-10 (a)). When this surface undergoes a deformation, due to the geometric module of the fringes, the fringes observed on the top do not appear any more parallel and equidistant (See Figure 4-10 (b)). Taking the fringe networks of the plane initial surface as a reference (Figure 4-11 (a)), this can be compared with the fringe networks of the deformed surface (Figure 4-11 (b)). For mere black and white fringe contrast, the altitude of each point at a fringe on the deformed surface can be easily calculated from the lateral shift of the fringe position Δx, knowing the angle of projection ϕ (see figure 4-15)

$$h = \frac{\Delta x}{\tan \phi} \tag{4-1}$$

In our case, for sinusoidal fringe contrast as generated by interference fringes, a better accuracy can be obtained by calculating the local phase value at each pixel of the image.

We can get the phase displacement, and then the geometric qualities of the deformation can be calculated. While this can be calculated manually, using software to analyze can be more accurate and faster. The software we used in this study is Fringe Analysis ®, Version 2.5 by HOLO 3 **[Fringe 2000]**.

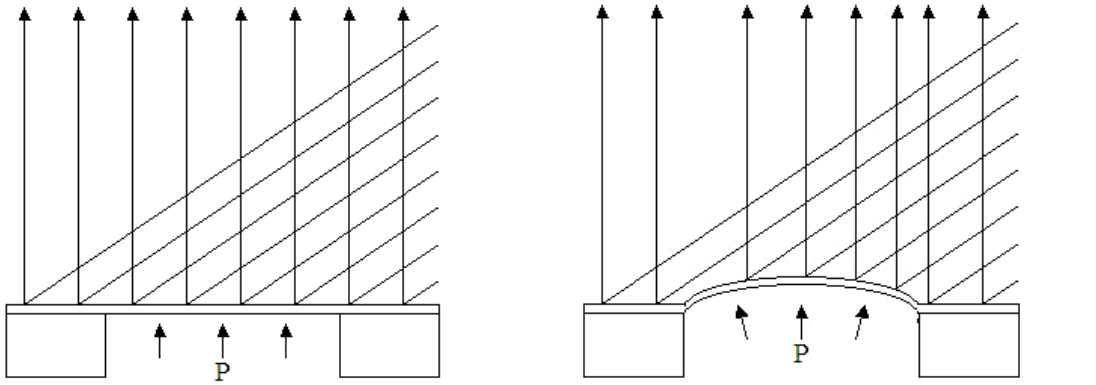

Figure 4-10: Cross-sectional view of the fringe projection with (a) equidistance and (b) non-equidistance.

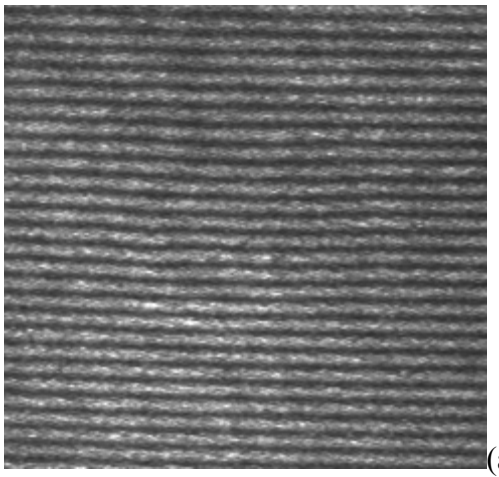
(a)
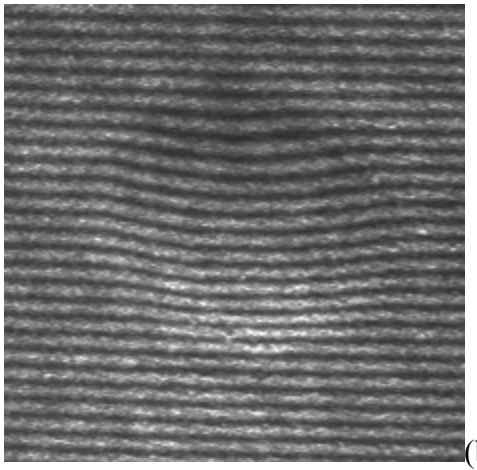
(b)

Figure 4-11: Images with (a) equidistance and (b) non-equidistance

Linear fringe patterns can be modified by the phase shifting interferometry. The concept of the phase shifting interferometry is that a time-varying phase shift is introduced between the reference wavefront and the sample wavefront in the interferometer. A time varying signal is then produced at each measurement point in the interferogram, and the relative phase between the two wavefronts as a function of location is encoded in these signals. The resulting intensity pattern is:

$$I(x,y,t) = I'(x,y) + I''(x,y)\cos[\phi(x,y) + \delta(t)] \tag{4-2}$$

To make a phase shift, at first, the laser beam goes through a beam expander to enlarge the laser beam. Then it passes through beam splitters to be separated into two beams. One of them is translated with a piezoelectric transducer of the mirrors or optical surfaces (Figure 4-10 and 4-12). Introducing an optical frequency difference between the two beams can produce a continuous phase shift. If the two optical frequencies are v and $v+\Delta v$, the frequency difference gives rise to a linear phase shift between the two beams:

$$\delta(t) = 2\pi \cdot \Delta\nu \cdot t \tag{4-3}$$

Since even a small optical frequency shift can result in a large frequency difference, this phase shifting method is very useful for the situations where dynamic measurements are required. In these situations the phase shift must occur faster than the changes that are being monitored **[Greivenkamp 1992]**. For this reason, we use this method to make fringe projection in our experiment as shown in Figure 4-8.

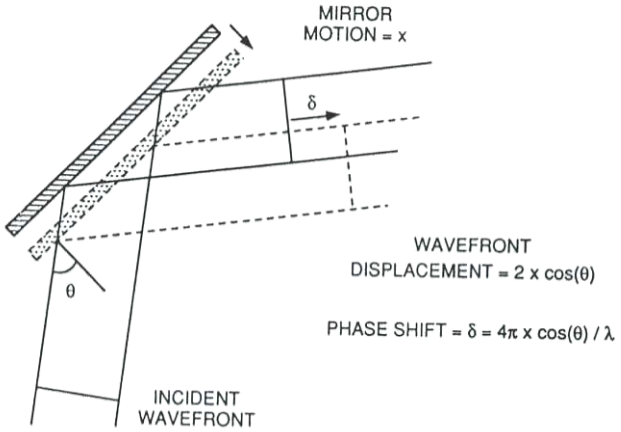

Figure 4-12: The induced phase shift due to a mirror translation at non-normal incidence ***[Greivenkamp 1992]****.*

In the digital image processing, we can store an image of interferogram into a computer and carry out the operation on the individual pixels later. A general expression for the record intensity in an interferogram is:

$$I(x,y) = a(x,y) + b(x,y)\cos\phi(x,y) \tag{4-4}$$

where *a(x,y)* is the mean intensity, b*(x, y)* the amplitude of periodic variation written as *V=b(x,y)/a(x,y)* and φ is the phase difference between the interfering waves. The visibility or contrast can be written as *V=b(x, y)/a(x, y)*, this expression is useful because pixels with too low visibility can result in invalid data **[Gasvik 1995]**.

To start the phase measurement interferometry technique, the following expression for the interferogram intensity is used:

$$I = a + b\cos(\phi + \rho) \tag{4-5}$$

where ρ is the additional phase term which is introduced and controlled experimentally through the piezoelectric transducer. 5 images of the surface with 5 different values of ρ are grabbed in a 1 second time. The local initial phase shift for the first image is then computed by the software HOLO3 Fringe Analysis **[Fringe 2000].** Then a complete phase image of the surface can be obtained, as seen on figure 4-13 and 4-14, from which the altitude of each point can be completed.

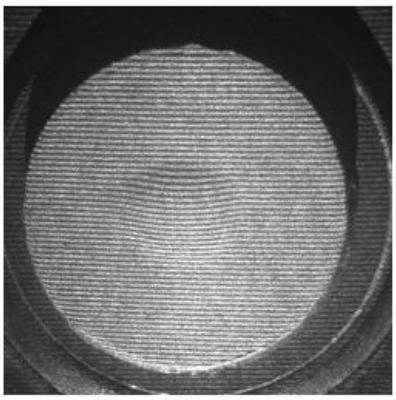

Figure 4-13: Real Image in the CCD

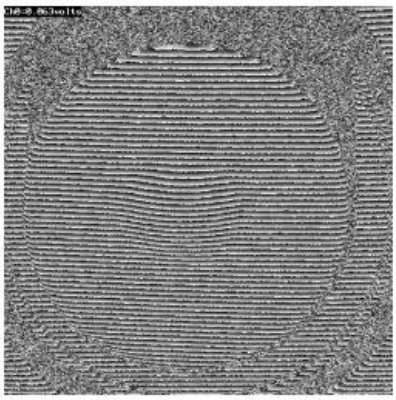

Figure 4-14: Image of calculated phase analyzed by four phase-stepping.

The optical geometry for the calculation of optical phase and deflection height is recalled in Figure 4-13. Height *h* of point A in the object at a distance x from origin C is given from triangulation principal by the relation

$$h(x) = \frac{\Delta x}{\tan\phi} = \frac{N(x)P_0}{\tan\phi} \tag{4-6}$$

Where ϕ is the angle of illumination, P_0 is the pitch of the fringe pattern of the object surface captured in CCD camera, and $N(x)$ is the unwrapped fringe number (Figure 4-15).

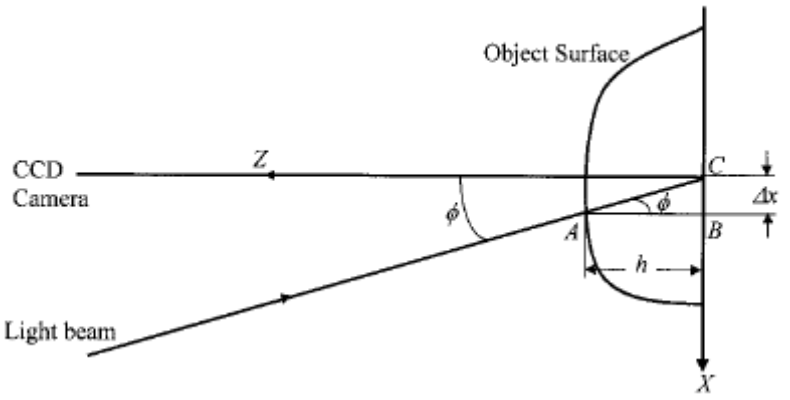

Figure 4-15: Fringe projection geometry. ***[Wang 2002]***.

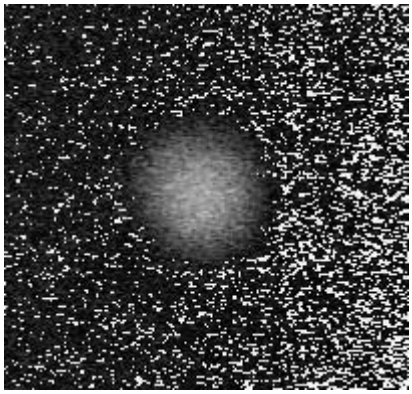

Figure 4-16: Subtraction of 2 images {reference (Fig.4-7(a))-deformed (Fig.4-7(b))}.

Figure 4-16 shows the phase of the deformed surface image subtracted from the reference one. It includes a lot of image noise, which will influence the precision of deformation measurement. To restrain the noise, the noise suppression method been used in our experiment is median filtering. This is a noise reduction technique whereby a pixel is assigned the value of the median to some local neighborhood (3×3, 5×5 or more) according to computing time availability. Figure 4-17 shows the image computed by median filtering, the image appears much smoother than Figure 4-16.

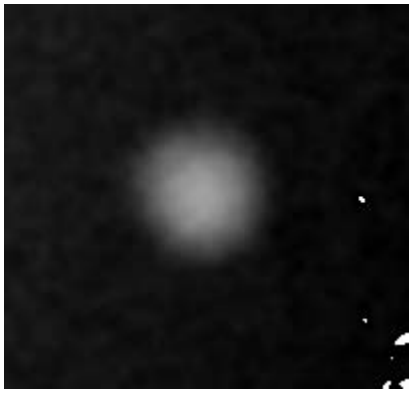

Figure 4-17: Filtered image of Fig. 4-16.

By applying the software HOLO3 Fringe Analysis **[Fringe 2000]**, we can complete all procedures in computer and acquire accurate quantitative results from figures (Figure 4-18). We can even obtain a 3D image as shown in Figure 4-19.

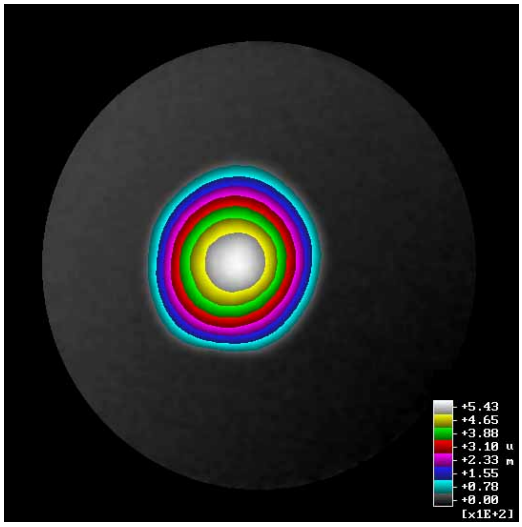

Figure 4-18: Measurement of the deformation of the blister test.

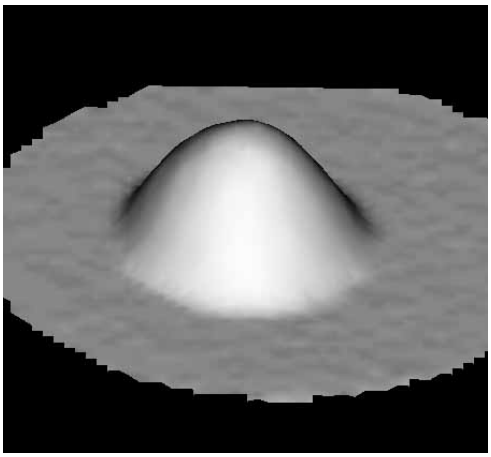

Figure 4-19: 3D image of the deformation of the blister test.

2.2. Sample preparation for Blister test

The blister test is a powerful technique, but the sample preparation for blister test is difficult. How can we fabricate free-standing windows? Recently, a deposited thin film adherent to a Si substrate or an adhesive polymeric tape glued to a substrate have been commonly used **[Hohlfelder 1997]**. Those methods have their advantages and intrinsic limits, such as the need of expensive semiconductor processing equipments. We use another method to fabricate free-standing windows in metal-oxide systems, which is described in this section.

2.2.1. Silver (Ag)/Barium Titanate ($BaTiO_3$)

Discs of $BaTiO_3$ (25 mm in diameter and 2.5 mm in thickness) are prepared by die-pressing at 50 MPa. The discs are first pre-fired at 1100 °C for 1 h to obtain a handling strength. A hole with 3 mm diameter is then machined into the center of the

pre-fired discs by using a steel drill. The discs are then sintered at 1350 °C and 1440 °C for 2 h. The diameter of the hole shrank to 2.1 mm after firing. The relative density of $BaTiO_3$ is then > 98 %. Finally the discs are ground with fine SiC particles to achieve a flat smooth surface. The final substrate surface roughness R_a is about 0.2 μm, as measured with a profilometer. Figure 4-20 shows the flow chart for the preparation of $BaTiO_3$ substrate.

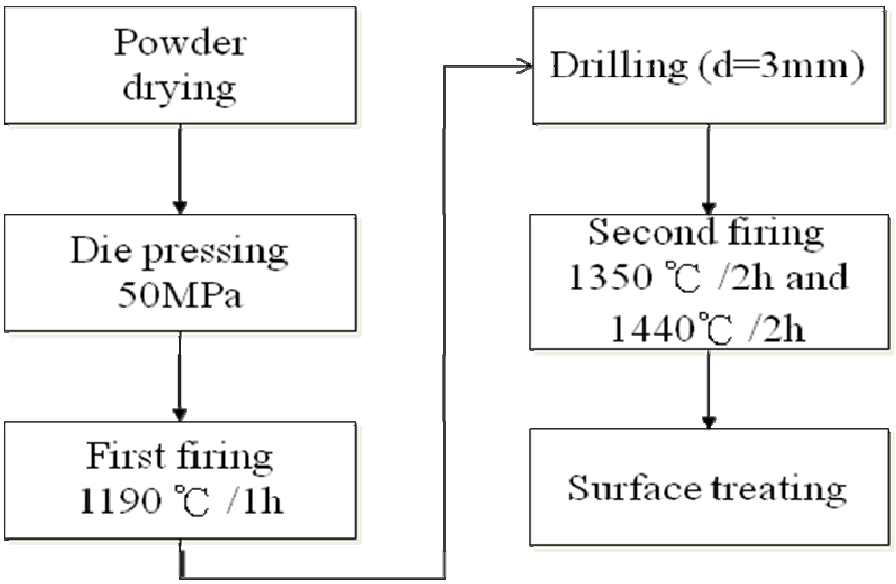

Figure 4-20: The flow chart for the preparation of $BaTiO_3$ substrate. The heating and cooling rate are 3 ℃/min in both firing stages.

To bond metal and ceramic together, metal powder is treated with organic binder and a small amount of glass to form metal paste. A silver paste composing of silver particles, binder and glass particles is prepared for screen printing. A silver powder showed in Table 4-3 is used. The silver powder/glass frit ratio is 98.75/1.25 in weight. The powder/organic vehicle ratio is 80/20 in weight. All are mixed and milled with the help of a media mill. Screen-printing is used to apply the Ag paste onto the flat surface of the $BaTiO_3$ discs.

Round adhesive tape patches with 3 mm in diameter are applied on a $BaTiO_3$ plate to make silver patches. To fabricate these silver circular plates, the Ag layer is screen printed over the whole $BaTiO_3$ disc surface and patches, and then the $BaTiO_3$ disc with Ag layer and adhesive tape patches is fired at 500 °C for 1 h to remove the adhesive tape. Therefore, we could obtain several pre-fired silver membranes with 10 μm thickness and 3 mm diameter, which are used to cover the central hole of the substrate discs as free-standing Ag membranes (Figure 4-21).

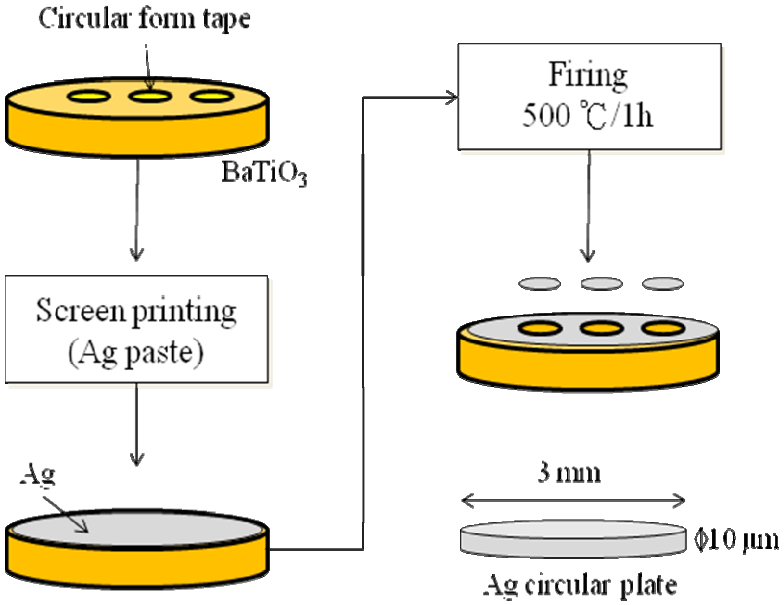

Figure 4-21: The flow chart for the preparation of silver membrane use to cover the central hole of the substrate discs. The heating and cooling rate are 3 ℃/min.

The discs including these free-standing membranes over the holes are then screen printed with Ag electrode for several times until the desired thickness of Ag layer is achieved and fired at 600, 700, 800 or 850 °C for 1 h (Figure 4-22).

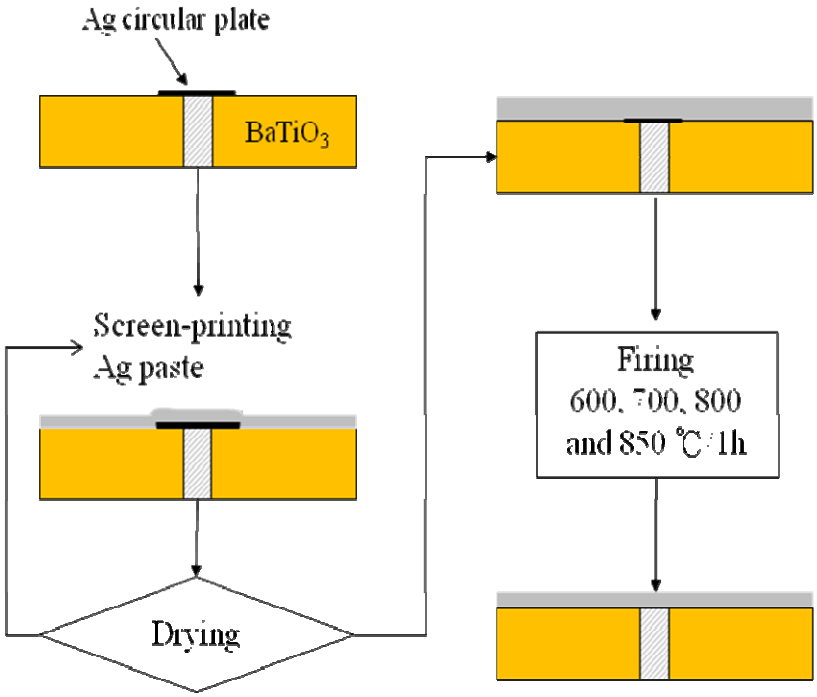

Figure 4-22: The flow chart for the preparation of blister test sample (Ag/$BaTiO_3$). The heating and cooling rate are 3 ℃/min.

2.2.2. Nickel (Ni)/Barium Titanate ($BaTiO_3$)

The procedure of fabricating the barium titanate substrate is mentioned in 1.3.1. A nickel paste is prepared for screen printing. A nickel powder with average particle size of 2.8 μm is used. The nickel powder, glass frit and organic vehicle are mixed and milled with the help of a media mill. A thick nickel circular film (diameter 2mm, thickness 125 um, purity 99.99 %) are used to cover the central hole of the discs as free-standing nickel membranes. The discs including these free-standing membranes over the holes are then screen printed with nickel paste for several times.

To avoid nickel oxidization these specimens should be fired under reduction atmosphere. Nickel and barium titanate are co-fired under 5 % hydrogen/95 % nitrogen atmosphere. Figure 4-23 shows the specimen after firing, the nickel film can't attach to substrate and separate totally. We changed the fire procedure. Due to the oxide can enhance surface wetting, the specimen are first fired at low temperature in Ar atmosphere with air mixed to obtain thin nickel oxide on nickel surface, which will enhance adhesion of nickel/barium titanate substrate, then nickel and barium titanate are co-fired under 5 % hydrogen/95 % nitrogen atmosphere at 1200 °C for 1h to reduce nickel oxide to nickel. After firing we can fabricate the specific specimen for blister test (Figure 4-24).

Figure 4-23: After firing, the nickel film separates totally from the substrate.

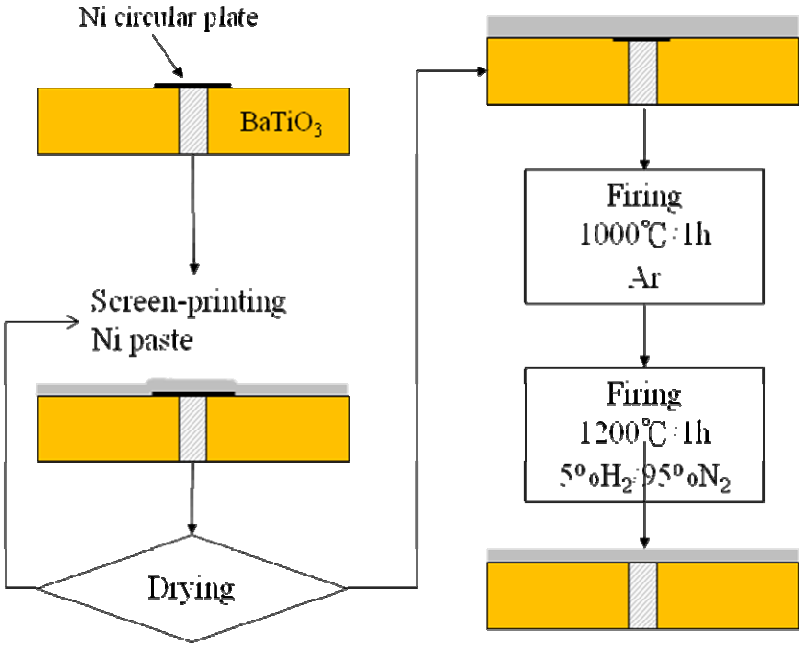

Figure 4-24: The flow chart for the preparation of blister test sample ($Ni/BaTiO_3$). The heating and cooling rates are 3 ℃/min.

2.2.3. Nickel (Ni)/Silver (Ag)/ Barium Titanate ($BaTiO_3$)

Silver/barium titanate specimens are fired at 850 °C for 1 h in air first, the procedure is showed in Figure 4-24, and then nickel paste is screen printed on silver/barium titanate specimens of blister test to make a sandwich structure (Ni)/ (Ag)/ ($BaTiO_3$). After screen printing the specimens are co-fired at 850 °C for 1 h under argon atmosphere to make nickel dense and attach to the silver film (Figure 4-25).

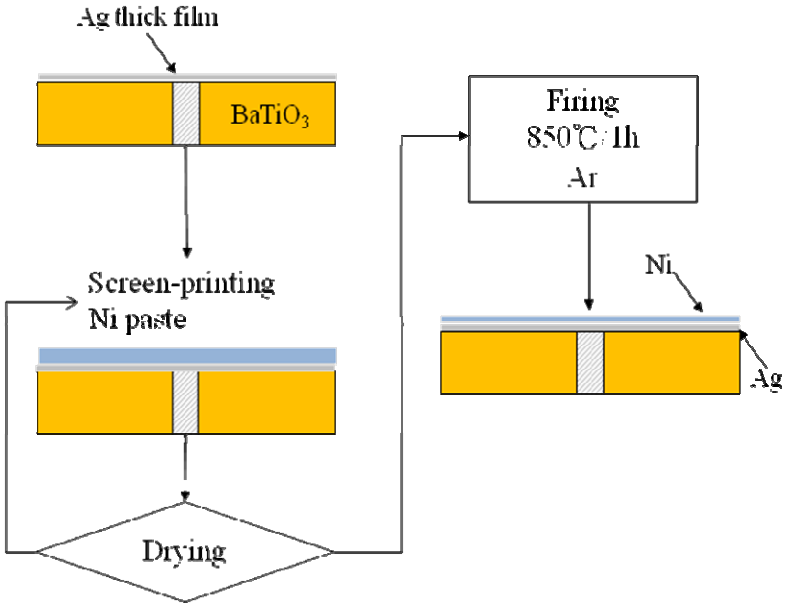

Figure 4-25: The flow chart for the preparation of blister test sample ($Ni/Ag/BaTiO_3$). The heating and cooling rate are 3 ℃/min.

2.2.4. Silver (Ag)/Nickel (Ni)

A pure bulk nickel is cut into geometry of 2 cm×2 cm×0.5 cm. A hole with 2 mm diameter is then machined into the center of the nickel plates by using a drill. The method of free-standing window fabrication, which is mentioned in section 1.3.1, and screen printing are performed to put silver paste on bulk nickel. Firing condition is set to 850 °C for 1 h under argon atmosphere (Figure 4-26).

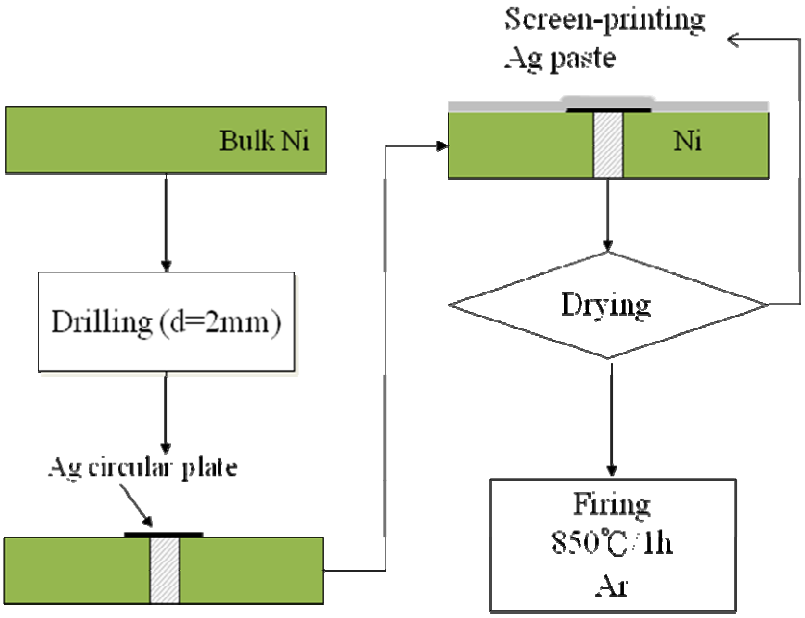

Figure 4-26: The flow chart for the preparation of blister test sample (Ag/Ni). The heating and cooling rate are 3 ℃/min.

3. Indentation test

3.1.Indentation test apparatus

An apparatus for micro-Vickers hardness test is used for interface and cross-sectional indentation test. The cross-sectional microstructure and crack in interface are observed by scanning electron microscopy. Crack length is measured by scanning electron microscopy and optical microscopy.

3.2.Sample preparation for indentation test

3.2.1 Interface and cross-sectional indentation test

To compare the experimental results of blister test with those of indentation test, the specimens of blister test are used in interface and cross-sectional indentation test. The cross-section of the specimen must be revealed to perform the cross-sectional indentation test. Directly cutting would damage the metal/oxide interface and make

films separate from substrate. A way to reveal the sample cross-section without damage is necessary for this test. In this study, the specimens are placed into molds and filled with resin for cold mounting, and then the specimens are ground and polished to show the cross-section. Cold mounting could protect the specimens from damage during the grind procedure.

We don't need to remove specimens from cold mounting in interface indentation test, but for cross-sectional indentation test the cold mounting would restrict the films to deform, so we need to take the resin away. Therefore, the polished sample is flipped to dip into acetone about 5 mm depth for 12 h. The cold mounting resin will melt into acetone along the interface of sample/resin, so we can obtain the unstrained metal film in certain length. The rest resin can be used as the base of specimen during cross-sectional indentation test (Figure 4-27).

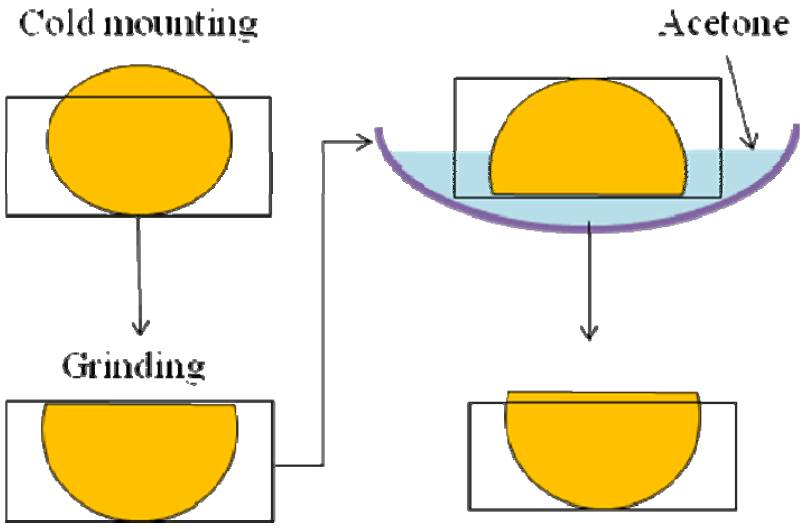

Figure 4-27: The flow chart for the sample preparation of cross-sectional indentation test ($Ag/BaTiO_3$).

3.2.2 Normal indentation test

A 400 nm thin Ni or Ag layer is deposited by thermal evaporation onto the $BaTiO_3$ substrate surface. The oxide substrate is described in section 1.3.1. The support boat is fabricated by W, the source is 99.9% Ni or 99.9% Ag and working pressure is about 5 x 10-7 torr.

4. Conclusions

The blister test is the major technique used in our investigation. The apparatus for blister test and analytical methods are introduced in detail in the previous sections. For indentation test an equipment of micro Vickers indentation was used. Appropriate specimen preparation techniques have been developed for both of these tests, with silver and nickel coatings on barium titanate substrates.

References

[Fringe 2000] *Fringe Analysis*, Version 2.5, HOLO 3, Centre régional d'Innovation et de Transfert de Technologies, Saint Louis, France (2000).

[Gasvik 1995] K. J. Gasvik, "*Optical Metrology*" ISBN 0-471-95528-0 (1995).

[Greivenkamp 1992] J. E. Greivenkamp, J. H. Bruning, "*Phase Shifting Interferometry*". Optical shop testing, second edition, edited by Daniel Malacara. ISBN 0-471-52232-5 (1992).

[Hohlfelder 1997] R. J. Hohlfelder, H. Luo, J. J. Vlassak, C.E.D. Chidsey, W.D.Nix, "*Measuring interfacial toughness with the blister test*" Materials Research Society Symp. Proc. 436, (1997) pp.115-120.

[Hsu 2002] Y. J. Hsu, Y. H. Chang, Y. L. Chai, G. J. Chen, "*Residual stress and thermal stability of the Fe – Ni – Cr/Invar bimetal membrane used for micro-actuation,*" Thin Solid Films, 418 (2002) pp.189 – 196.

[Taheri 2000] N. Taheri, N. Mohammadi, N. Shahidi, "*An automatic instrument for measurement of interfacial adhesion of polymeric coatings,*" Polymer Testing, 19 (2000) pp.959–966.

[Wang 1999] C. Wang, "*Measurements of Interfacial Strength from the Blister Test*" Journal of Applied Polymer Science, Vol. 73, (1999) pp.1899–1912.

[Wang 2002] S. H. Wang, C. J. Tay, C. G. Quan, H. M. Shang, "I*nvestigation of membrane deformation by a fringe projection method*" Applied Optics, v.22 n.1 (2002) pp.101-107.

Chapter V

Results and Discussion

1. Blister test 105
1.1. Silver (Ag)/Barium Titanate ($BaTiO_3$) 106
1.1.1. Influence of different silver film firing temperature 107
1.1.2. Influence of different substrate roughness 116
1.1.3. Influence of different substrate firing temperature 120
1.2. Nickel (Ni)/Barium Titanate ($BaTiO_3$) 122
1.3. Nickel (Ni)/Silver (Ag)/ Barium Titanate ($BaTiO_3$) 126
1.4. Silver (Ag)/Nickel (Ni) 128
2. Indentation test 129
2.1. Normal indentation test 129
2.2. Interface indentation test 132
2.3. Cross-sectional indentation test 135
3. Comparison between blister and indentation test 139
3.1. Comparison between G_{ci} from normal indentation test with the values from blister test 139
3.2. Comparison between G_{ci} from interface indentation test with the values from blister test. 139
3.3. Comparison between G_{ci} from cross-sectional indentation test with the values from blister test 140
4. Conclusions 140
4.1. Silver (Ag)/Barium Titanate ($BaTiO_3$) 140
4.2. Nickel (Ni)/Barium Titanate ($BaTiO_3$) 141
4.3. Nickel (Ni)/Silver (Ag)/ Barium Titanate ($BaTiO_3$) 141
4.4. Silver (Ag)/Nickel (Ni) 141
References 142

1. Blister test

Experimentally, when conducting the blister test for determination of metal/oxide interface adhesion, a increasing volume of incompressible liquid is injected to make the metal layer blister and separate from its substrate. After increasing during the bulge period, the pressure reaches a maximum value and even decreases when debonding occurs. The injection is withdrawn progressively and the p vs h curve generally falls down along a linear path and shows a residual deflection h_p, proving that the film has been plastically deformed. After the first pressurization and de-bonding, as long as the system is stable we can re-inject liquid to make blistering occur again and then release the pressure again. Therefore, each repeated pressurization can be used to determine the adhesion energy of the interface by fitting a hyperbolic curve to the debonding threshold points according to equation (2-52). At each pressurization, since we record successive 3-D contours of the complete blister, we can check the diameter values to determine as accurately as possible the point when the blister begins to grow and the interfacial crack begins to propagate. Figure 5-1 shows an example of images of blister growth captured by CCD camera. We defined this point as the critical point (Figure 5-1(2)) to be used for G_c determination. In many cases, we can obtain several debonding points on one specimen till the metal layer is broken or totally de-bonded. Since the metal (Ag or Ni) membrane behaviour is likely to be dominated by residual stress (due to thermal contraction mismatch between metal and ceramic after firing) rather than by high Young's modulus and stiffness, we used C = 0.516 in equation (2) for result analysis in this study **[Dupeux 1998]**.

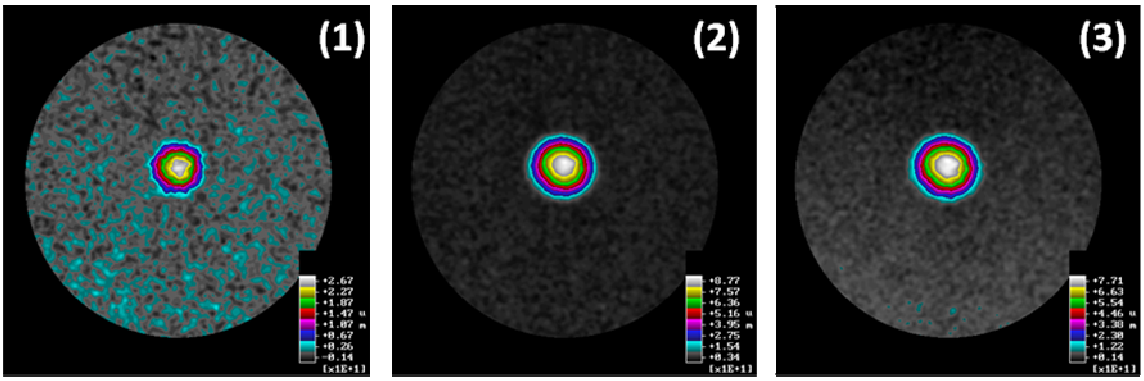

Figure 5-1: The images of blister growth captured by CCD camera. (1) Free standing window begins to bulge without film separation. (2) Film starts to separate from substrate at critical pressure. (3) Film continues separating from substrate with pressure decrease.

1.1. Silver (Ag)/Barium Titanate ($BaTiO_3$)

The metal–ceramic system of interest here cannot be considered as a very reactive one. The specimens of $Ag/BaTiO_3$ were fired to fabricate silver paste film on barium titanate substrate in air atmosphere. The oxidation of metal is not considerable, because of the chemical reaction at high temperature at interface is $2Ag + 1/2O_2 \rightarrow Ag_2O$ and Ag_2O will be promptly decomposed at room temperature **[Sugihara 1990]**. This means that no reaction layer exists at $Ag/BaTiO_3$ interface. Ag_2O is a barrier layer to stop Ag diffusing into the $BaTiO_3$ at high temperature. Figure 5-2 shows the X-ray diffraction pattern of both surfaces (noncontact or contact with $BaTiO_3$) of silver film fired at 850 ℃ and all peaks in Figure 5-2 indicate that no Ag oxide exist in Ag film.

The coincident between the observed diffraction peaks and the exact position where they are expected from the lattice parameter values of pure silver also indicates that the level of residual stresses in the silver layer remains very low after firing.

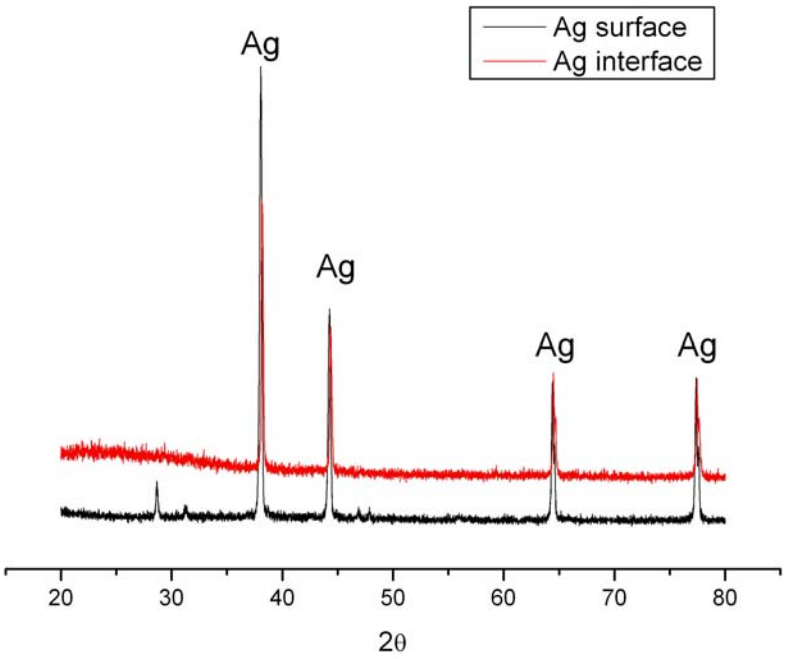

Figure 5-2: The X-ray diffraction pattern of both surfaces (noncontact or contact with $BaTiO_3$) of silver film.

Figure 5-3 shows the surface microstructure observations of silver films sintered at different temperature. All silver films present porous microstructure and the porosity of silver film decreases while sintering temperature increases.

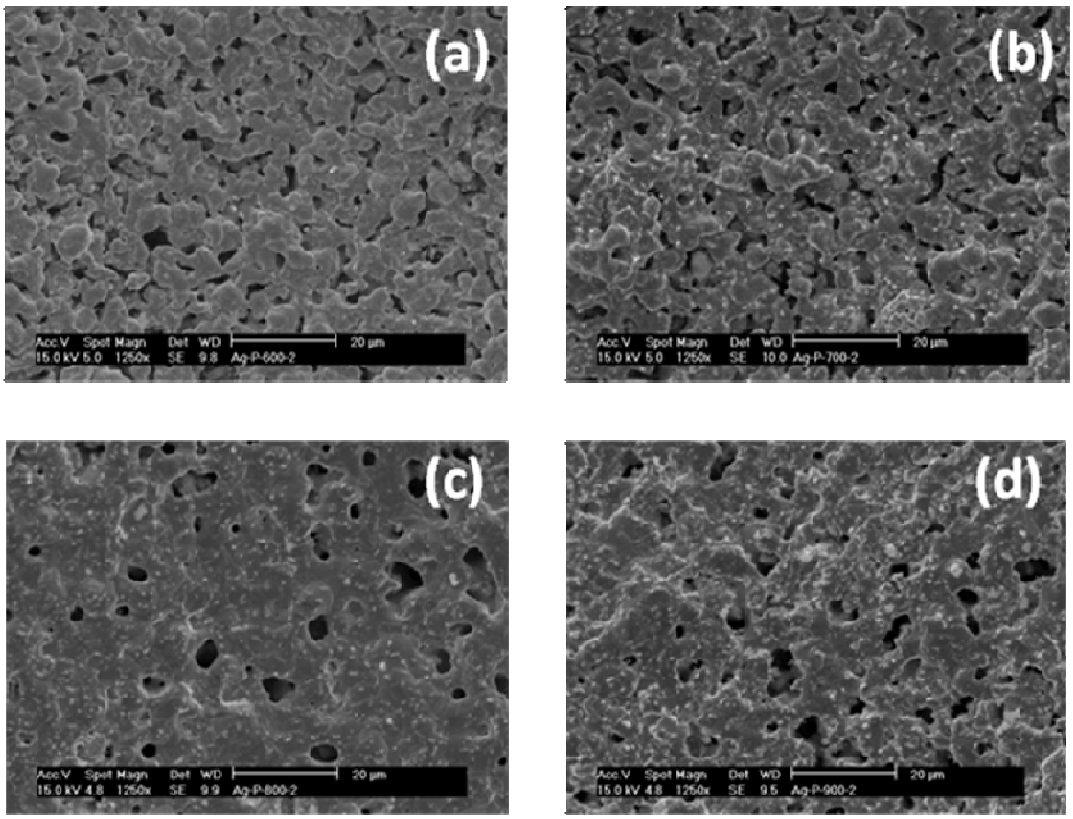

Figure 5-3: SEM micrographs of silver film sintered at (a) 600℃ (b)700℃ (c)800℃ (d)900℃ for 1 hour.

1.1.1. Influence of different silver film firing temperature

Figure 5-4 shows the cross-sections of the specimens after sintering. The Ag/$BaTiO_3$ interface appears to be relatively smooth and abrupt at the magnification we used. The thickness of the silver layer has been changed between 55 μm and 130 μm. It has been measured after sintering by micrometer screw gauge, with reference to the initial substrate thickness. For each substrate and substrate with film, five points were measured and the average was taken as thickness.

Figure 5-4(a) shows the Ag layer fired at 600 °C for 1 h. The pores within the sintered metal are interconnected and the average porosity is 11 %, which is calculated by an image analyze software: ImageJ **[ImageJ]**. Figure 5-4(b) shows the silver film fired at 700 °C. It can be observed that most of the pores are no longer interconnected and the average porosity is 10 %. When the firing temperature was raised to 800 °C (Figure 5-4(c)), the average porosity of Ag film became 8 %. The shrinkage rate of Ag film from 700 °C to 800 °C is higher than that between 600 °C and 700 °C. Figure 5-4(d) shows the silver film fired at 850°C and the average porosity in the silver film is 7 %. The size of the pore within the Ag film is increased after the treatment at 850 °C, though their volume fraction is more or less the same as that in the film fired at 800 °C.

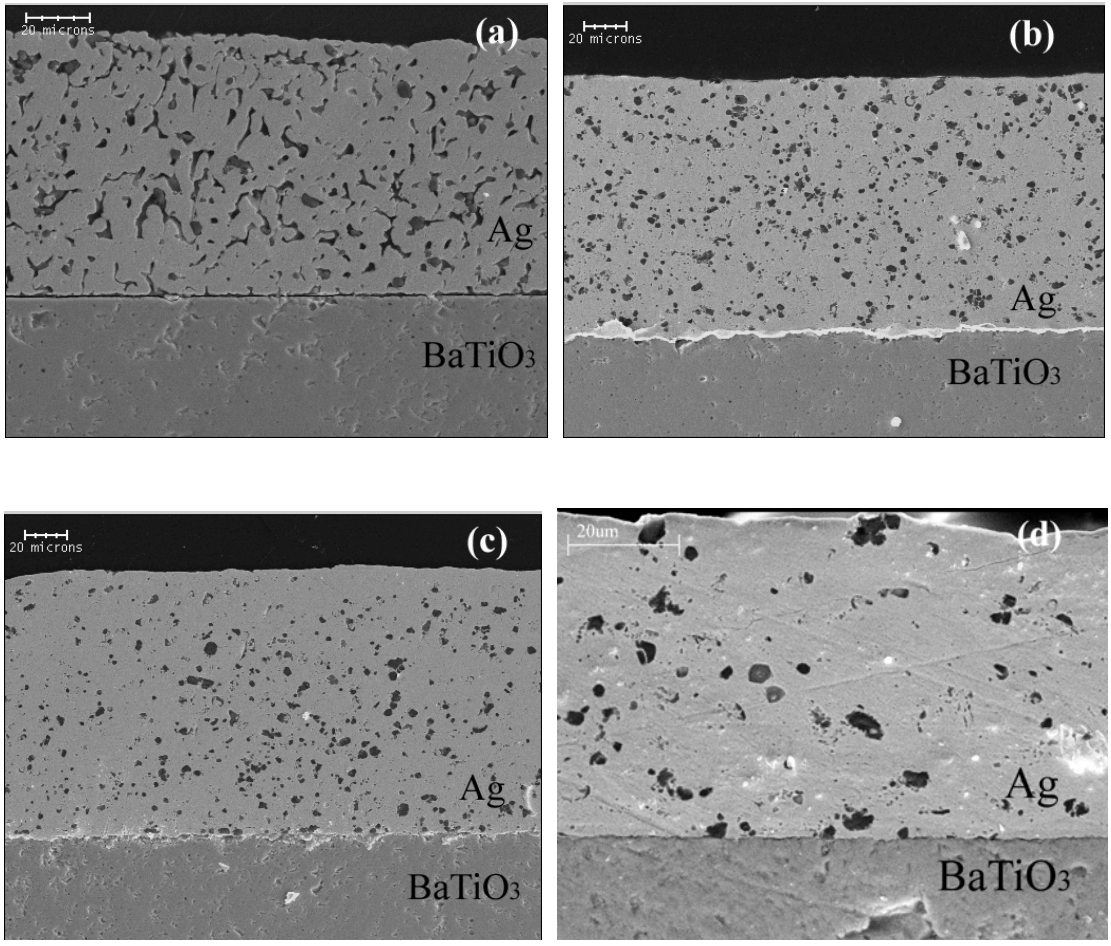

Figure 5-4: Cross-section views of Ag/$BaTiO_3$ interfaces. Ag films were fired at (a) 600 ℃ (b) 700℃ (c) 800℃ (d) 850 ℃ for 1 hour.

For our purpose of adhesion measurement, the porosity within the Ag/$BaTiO_3$ interface is very likely to have a strong influence on the interfacial crack propagation energy, but it is very difficult to determine experimentally from optical or SEM observations. In the following, we take the interface porosity (defined as the ratio of the non-contacting area to the total interface area) as equal to the internal porosity in the bulk of the silver layer.

The resulting critical energy release rates G_{ci} of the $BaTiO_3$/Ag interfaces for each Ag paste sintering temperature are listed in Table 5-1. As explained before, these values are corrected by removing the influence of generalized plastic deformation of the membrane, but they still include the contribution of the confined plasticity which is likely to occur at the crack tip during the propagation of the interfacial crack, just like cohesive crack propagation energy in any ductile homogeneous metal.

Table 5-1: The resulting critical energy release rates Gci of the $BaTiO_3$/Ag interfaces for each Ag paste sintering temperature

Firing temperature	Gc(J/m^2)of successive pressurizations	Sample no. 1	2	3	4	5	6	7	Average	Porosity
600(℃)	G_{c1}	5	5	5.5	3.5	4				
	G_{c2}	4								
	Average	4.5	5	5.5	3.5	4			4.5±0.71	11%
	Thickness(μm)±10	108	75	125	68	109				
700(℃)	G_{c1}	5.5	5	5	3	5	6			
	G_{c2}			3	4	5	5			
	Average	5.5	5	4	3.5	5	5.5		4.75±0.95	10%
	Thickness(μm)±10	73	84	67	97	86	114			
800(℃)	G_{c1}	5	6	8	6	5	6			
	G_{c2}	5		8	5	5				
	G_{c3}	3.5			5					
	G_{c4}				5					
	Average	4.5	6	8	5.25	5	6		5.8±1.21	8%
	Thickness(μm)±10	95	128	83	74	71	117			
850(℃)	G_{c1}	6	8	6	4.5	6	7	6		
	G_{c2}		9	7	7		8	7		
	G_{c3}			6.5	7		6			
	G_{c4}				5					
	G_{c5}				5					
	Average (J/m^2)	6	8.5	6.5	5.7	6	7	6.5	6.60±1.16	7%

Table 5-1 also shows the thicknesses of specimens fired at 600 °C, 700 °C and 800 °C. Theoretically speaking, thick films will contain more defects, and these defects may make plastic deformation occurs more easily during film deflection. However, since we correct the results for general plastic deformation of the membrane, this should not have a strong influence on the corrected results.

Indeed, at the same firing condition, the influence of the film thickness on interface strength seems to be smaller than the experimental dispersion of the energy values. Therefore, it will not be considered in the following discussion of results.

The values of G_{ci} for specimens which are fired at 600 ℃, vary from 3.5 to 5.5 J/m^2. Figure 5-5 illustrates the experimental data acquired from blister test and the fitting blister equation ($G=cph$). The blister equation is calculated with average critical energy release rate of Ag/$BaTiO_3$ interface after correcting for the generalized plastic deformation of the specimen. Therefore, most of the experimental raw curves go farther pass the blister curve in p vs h coordinates.

The average G_{ci} for various sintering temperatures is also listed in Table 5-1. As we mentioned before several results can be acquired for one specimen by repeating injection and release of hydraulic pressure. Only one or two result of G_{ci} have been obtained from specimens sintered at 600 ℃. Some of the pores in silver film are interconnected, that may make water pass through the film and cause hydraulic pressure down. Consequently only six pressurization results have been considered as valid.

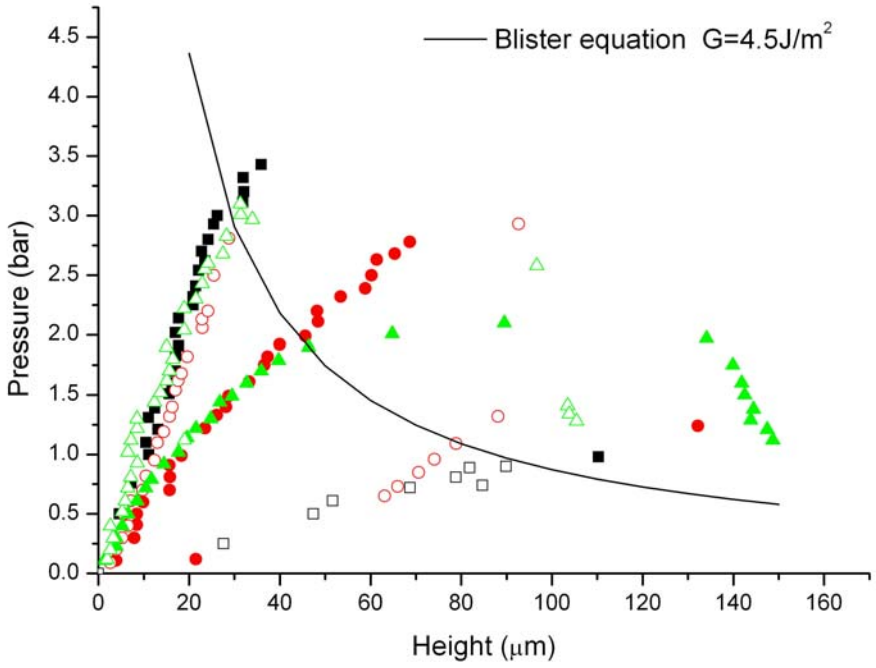

Figure 5-5: The experimental data acquired from blister test, Ag fired at 600℃, and the fitting blister equation, for 4.5 J/m^2.

The values of G_{ci} for interfaces fired at 700 °C vary from 3 to 6 J/m^2, which is close to the result for 600 °C. The inter-particle contact area for sintered powders increases while firing temperature increases from 600 °C to 700 °C, (Figure 5-4(a), 5-4(b)). It seems that the subsequent decrease of porosity does not affect much the interface strength at this stage. Figure 5-6 shows the experimental data acquired from blister test and the fitting blister equation, where the average energy release rate is 4.75 J/m^2.

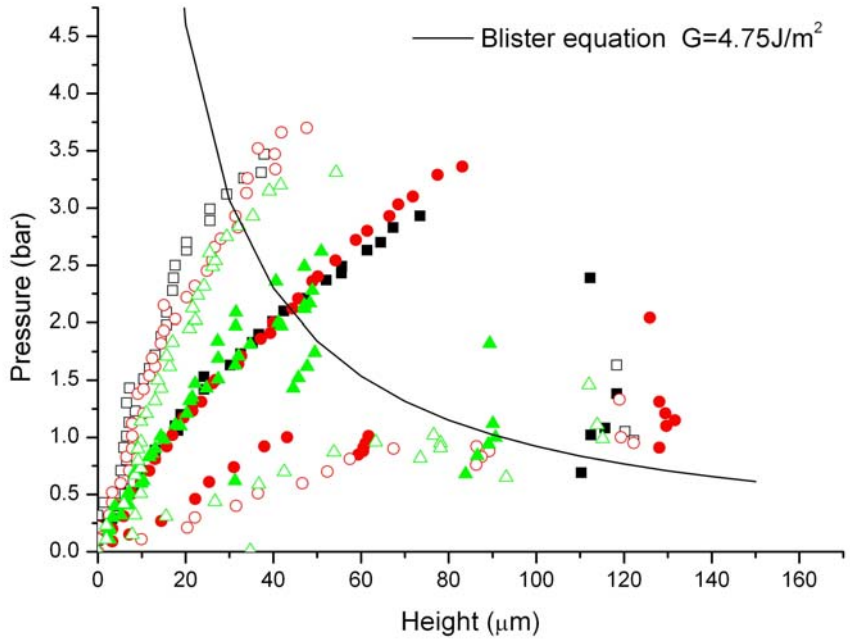

Figure 5-6: The experimental data acquired from blister test, Ag fired at 700℃, and the fitting blister equation, for 4.75 J/m^2.

The values of G_{ci} fired at 800 °C vary from 3.5 to 8 J/m^2, with an overall average value around 5.8 J/m^2 (Figure 5-7). At 850°C the critical energy release rate of interface cracks ranges from 4.5 to 9 J/m^2 (Figure 5-8).

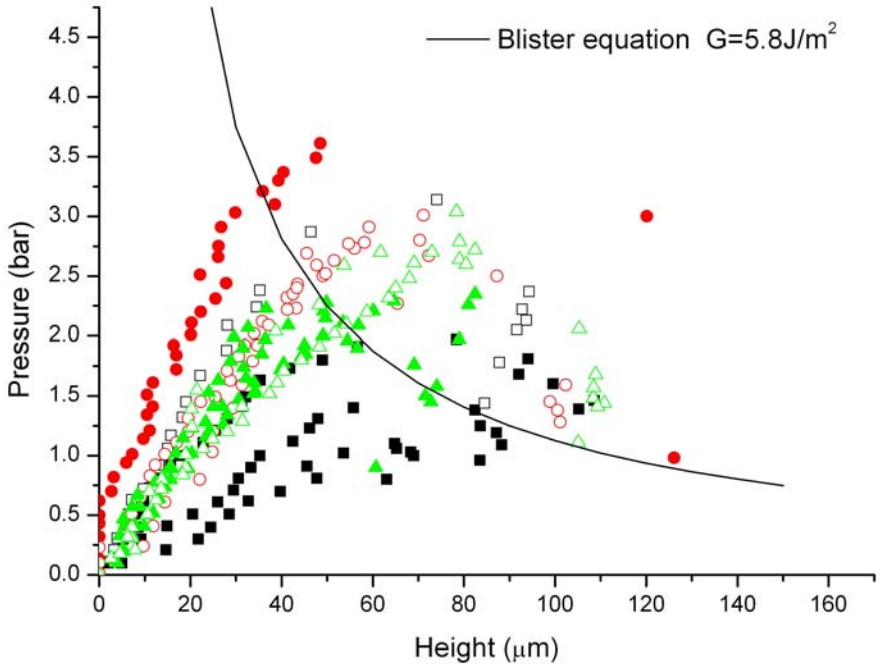

Figure 5-7: The experimental data acquired from blister test, Ag fired at 800℃, and the fitting blister equation, for 5.8 J/m^2.

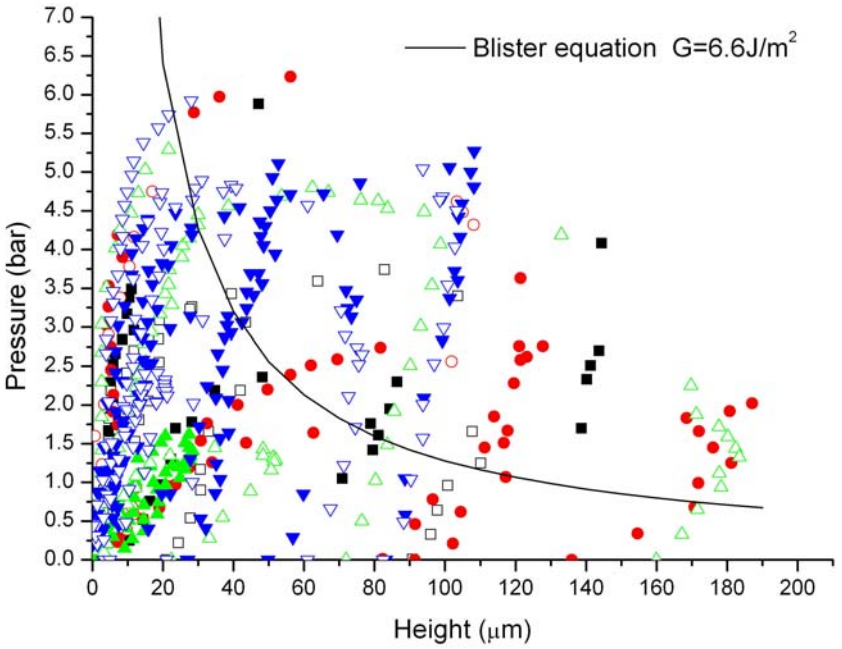

Figure 5-8: The experimental data acquired from blister test, Ag fired at 850℃, and the fitting blister equation, for 6.6 J/m^2.

Weibull parameter M is commonly used to describe the strength distribution. According to the Weibull equation:

$$(1-F)=\exp[-\left(\frac{\sigma}{\sigma_0}\right)^M] \tag{5-1}$$

where F is the distribution function of failure results, σ is the applied load, σ_0 is a reference load and exponent M is called the Weibull modulus.

A plot of lnln(1/(1-F)) versus lnσ will give the Weibull parameter M as the slope of a straight line. High Weibull modulus M means a more consistent material and a narrower probability curve of the strength distribution. It also means that uniform defects are distributed throughout the entire material. We can regard interfacial energy release rate as interface strength in Weibull modulus determination. Weibull moduli for our four silver sintering temperatures were calculated and are showed in Figure 5-9.

The values of M are 5.06, 3.58, 3.66 and 3.73 respectively. Compared to the common value for ceramics (around 10) or metal (from 10 to 100), we can observe that the strength distribution is widely dispersed in this research. Fracture starts and runs along defects existing in materials and bimaterial interfaces usually contain more defects than bulk materials. It is very difficult to fabricate uniform interfaces due to the misfit of material properties, with wider possible chemical contamination and variation in elaboration condition. Therefore, failure tends to occur even more easily in interface and with wider strength distribution wide.

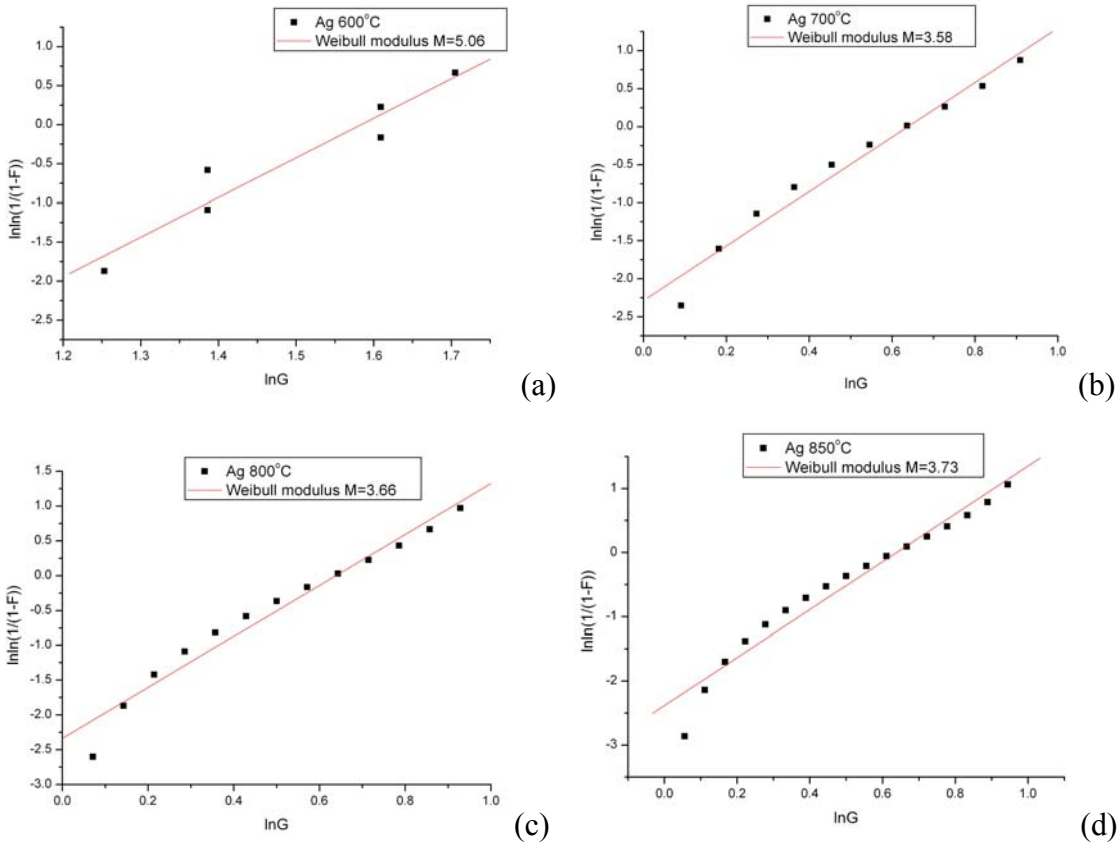

Figure 5-9: Weibull modulus plots of four silver sintering temperatures (a) 600℃ (b)700℃ (c)800℃ (d)850℃.

The relation between average G_{ci} and sintering temperature is shown in Figure 5-10, even taking into account the wide dispersion interval for each value. The critical energy release rate of interface crack increases when firing temperature increases, especially in the range of 700°C to 800°C. The changes in the pore volume through the metal membrane and similarly along the interface, is likely to be an important factor to cause this variation.

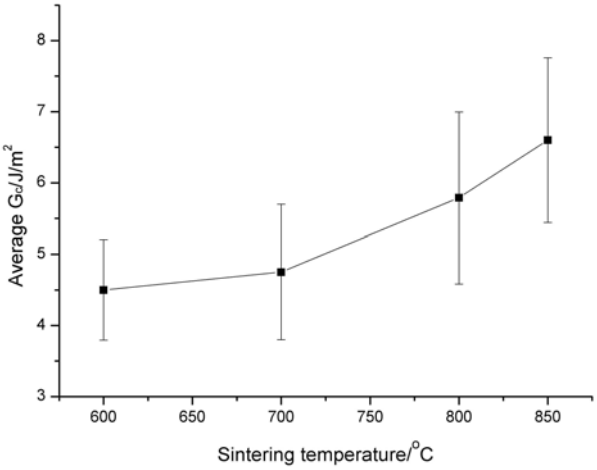

Figure 5-10: Average G_{ci} of interface versus sintering temperature of Ag membrane.

Figure 5-11 shows the critical energy release rate G_{ci} of Ag/$BaTiO_3$ interfaces versus the porosity of the Ag film. The silver paste used in this study was named as G-1. Within the range of membrane porosity from 11% to 7%, the G_{ci} of the interface between porous silver membrane and $BaTiO_3$ substrate is almost a linear function of the porosity of the membrane. It is obvious that smaller contact areas across the metal/ceramic interface will reduce the interface strength. But for a given interface porosity, the size and shape of interface cavities must also play a role. Indeed, large round-shape cavities might blunt interface cracks and rather tend to prevent their propagation, while small fine-dispersed elongated cavities should cause high interface embrittlement. Some authors have reported finite element analysis simulation of a crack growth along the interface between a porous ductile material and a rigid substrate **[Radi 2001]**. But very few models nor experimental data for interfacial crack propagation between porous metal film and ceramic substrate are available in literature, maybe because of the difficulty to characterize the interface porosity, as mentioned before and even less under the form of quantitative adhesion measurement to be compared to our results. Thus the relation between the critical energy release rate of interface cracks and interface contact area is still not clear now. Some work in progress on this topic is described in Appendix 1. Based on very simple geometrical and physical assumptions, it demonstrates how a non fully linear relation may exist between the overall critical energy release rate and the fraction of contact area in a porous interface. A first application of this simple model has been made to our results in Appendix 1.

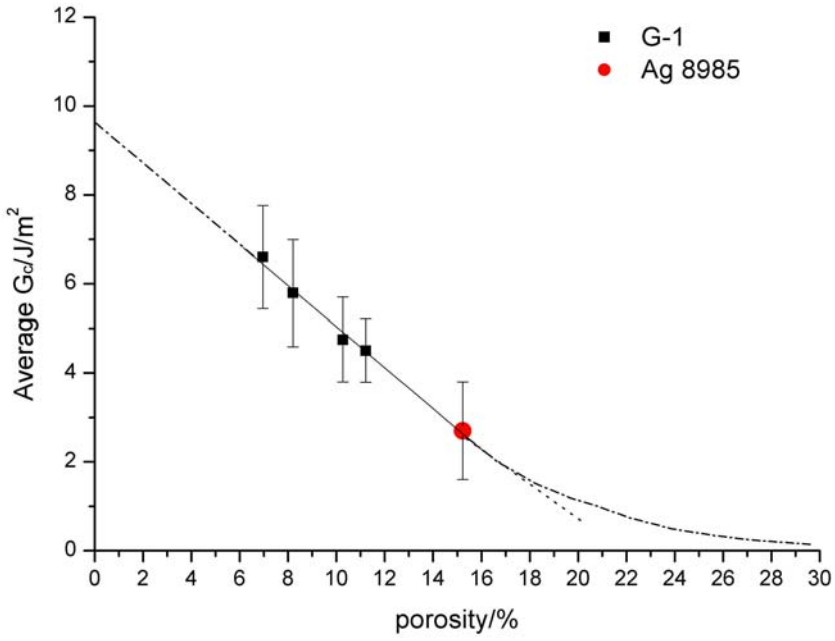

Figure 5-11: Average fracture energy of interface versus average porosity of silver membrane. ■ Silver paste fabricated by ceramic matrix composite laboratory (NTU); ● Commercial silver paste ***[Lee 2006]****.*

Comparing the results of commercial silver paste fired at the same sintering temperature, where the values of G_{ci} vary from 1.3 to 4.2 J/m^2 for Ag/$BaTiO_3$ interfaces, the results in the present work are much higher. The major differences between both studies are Ag powder particle size and chemical composition of Ag pastes. Both factors are likely to change the porosity of the film after firing and altogether the value of the thermodynamical interfacial work of adhesion itself. In figure 5-11, the values of the present work are plotted together with the reported adhesion strength of other silver paste (Ag 8985) to barium titanate **[Lee 2006]**, with the porosity measured using the same procedure. Both silver layer pastes contained some glass mixed with organic solvent and binder. From figure 5-11 we can observe that the chemical composition of the silver paste did not seem to influence much on interface adhesion. Contact area seems to play a more important role in the interface adhesion, since the same linear dependence of G_{ci} on porosity appears to be valid for both Ag pastes.

Such a linear relationship is actually the simplest assumption which may be made to account for the dependence of interfacial crack propagation energy on interfacial porosity. Extrapolating the linear fit of Figure 5-11 to a zero porosity value would lead to crack propagation energy about 10 J/m^2 for a full-contact Ag/$BaTiO_3$ interface, which is a rather reasonable value for metal/ceramic interface adhesion **[Felder 2003]**. On the reverse, a linear extrapolation of our results to higher porosity rates would lead to null crack propagation energy far before 100% porosity, which is not physically acceptable. So, another extrapolation law should apply for porosity higher than about 15%, compatible with complete loss of adhesion only for 100% interfacial porosity. Another possible cause for this discrepancy is that our assumption taking the interfacial porosity equal to the bulk porosity in Ag is grossly wrong, which is difficult to verify, but looks unlikely as close as we could observe our metal/ceramic interfaces. More experiments with better accuracy and a wider range of Ag membrane porosity will be necessary to clear these points.

The main contribution to the incertitude for our results may be attributed to the difficulty in determining the accurate critical de-bonding points and subtracting the plastic strain contribution. Anyway, our crack propagation energy values are higher than the usual estimates of the thermodynamical work of adhesion of metal/ceramic interfaces alone, around 1 J/m^2. This difference can easily be explained by the various contributions of dissipative mechanisms which operate during interfacial crack propagation, so that strongly adherent systems (like metal/metal or metal/adhesive interfaces) may reach interfacial crack propagation energies as high as hundreds of J/m^2 **[Felder 2003]**.

Indeed, the basic thermodynamic property of an interface between silver and $BaTiO_3$ is its free energy per unit area $\gamma_{Ag\text{-}BT}$. In experimental measurement, a different quantity can be determined: the true work of adhesion W_a which is the amount of energy

required to create free surfaces from bonded materials. The true work of adhesion is the intrinsic property that depends on the type of the bonds at the interface and the level of contamination on the initial surfaces. In the specific case of Ag/BaTiO3 interfaces, the contact angle in the $Ag/BaTiO_3$ is about 90 **[Sugihara 1990]** while the surface energy of silver is 1.25 J/m^2 **[Skriver 1992]**. Thus, W_a of $Ag/BaTiO_3$ interface can be estimated to be around 1.25 J/m^2 by the true work of adhesion. But the practical crack propagation energy G_{ci} is always higher than W_a. As seen in Chapter I, this difference, which has been extensively discussed in literature [**Volinsky 2002]**, is usually explained by the various contributions of three multiplicative factors:

The first one is the non-equilibrium thermodynamic state of the newly created fracture surfaces, and is estimated between 1 and 10. The second one is the effect of interface roughness, which causes the true contact area to be larger than its projected measurable value. This factor is generally only slightly larger than 1. The third factor is the energy dissipation through confined plastic deformation of materials at the interfacial crack tip. Therefore, the G_{ci} usually exceeds W_a by two or even three orders of magnitude and reach values as high as hundreds of J/m^2. In our case, the first factor is certainly partly responsible for the difference between W_a=1.25 J/m^2 and G_{ci}= 10 J/m^2 for a full-contact $Ag/BaTiO^3$ interface. But, even if we managed to subtract the energy contribution of generalized plastic deformation of the silver membrane, it is very likely that an important amount of confined plastic flow occurs at the crack tip on the side of the silver component, which is known as a very ductile material. This contribution of confined plasticity cannot be subtracted, and is actually inherent in the crack propagation phenomenon, and thus contributes to the mechanical strength of the interface.

1.1.2. Influence of different substrate roughness

The $BaTiO_3$ discs were ground with fine SiC and diamond particles to prepare difference surface roughness. $BaTiO_3$ is fired at two temperatures, 1350 ℃ and 1440 ℃ for 2 h. For $BaTiO_3$ fired at 1440 ℃, the roughness of the substrate of the discs which were ground with fine SiC particles, which is marked as 1440S, is about 0.15 μm. The roughness of the discs which were ground with diamond particles, which is marked as 1440D, is about 0.21 μm. Table 5-2 shows the results of critical energy release rates G_{ci} of the $BaTiO_3$/Ag interfaces for different substrate surface roughness, for $BaTiO_3$ substrates fired at 1440℃ and Ag paste fired at 850 ℃ for 1 h for bonding to the $BaTiO_3$ discs. The average G_{ci} of 1440D is about 3.7 J/m^2 and that of 1440S is about 6.5 J/m^2.

Table 5-2: The resulting critical energy release rates G_{ci} of the $BaTiO_3$/Ag interfaces for different substrate surface roughness (the firing temperature of $BaTiO_3$ is 1440°C for 2 h).

Substrate roughness	G_c (J/m^2) of successive pressurizations	Sample no. 1	2	3	4	5	6	Average
0.21(μm)	G_{c1}	6	2	5	3	1	9	
	G_{c2}	8	1.5	5.5	7	2	4	
	G_{c3}	2.5	1.5	3	3	2.5	4	
	G_{c4}	4		3	3		3	
	G_{c5}	3			3			
	Average (J/m^2)	4.7	1.67	4.13	3.8	1.83	5	3.73
0.15(μm)	G_{c1}	8.5	8	7	6	8	9	
	G_{c2}	9	6		7	5.5	6	
	G_{c3}	7	5.5			5.5	5.5	
	G_{c4}	8.5	7			6.5	6	
	G_{c5}		4			5.5	4.5	
	G_{c6}		4			6		
	Average (J/m^2)	8.25	5.75	4.5	6.5	6.17	6.2	6.48

Figure 5-12 and 5-12 show the experimental results of 1440S and 1440D respectively, both figures demonstrate the fitting blister equation of average interface energy release rates.

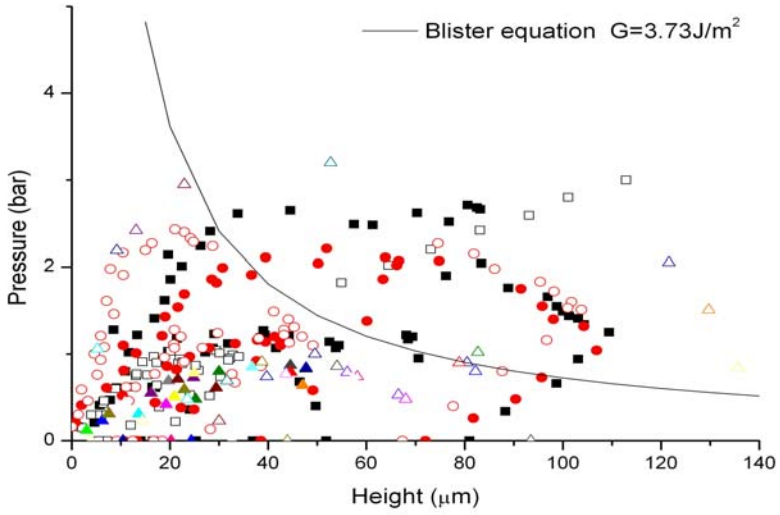

Figure 5-12: The experimental data acquired from blister test and the fitting blister equation, for G_{ci}= 3.73 J/m^2. Ag is fired at 850℃ and $BaTiO_3$ is fired at 1440℃. The average surface roughness of $BaTiO_3$ substrate is 0.21μm.

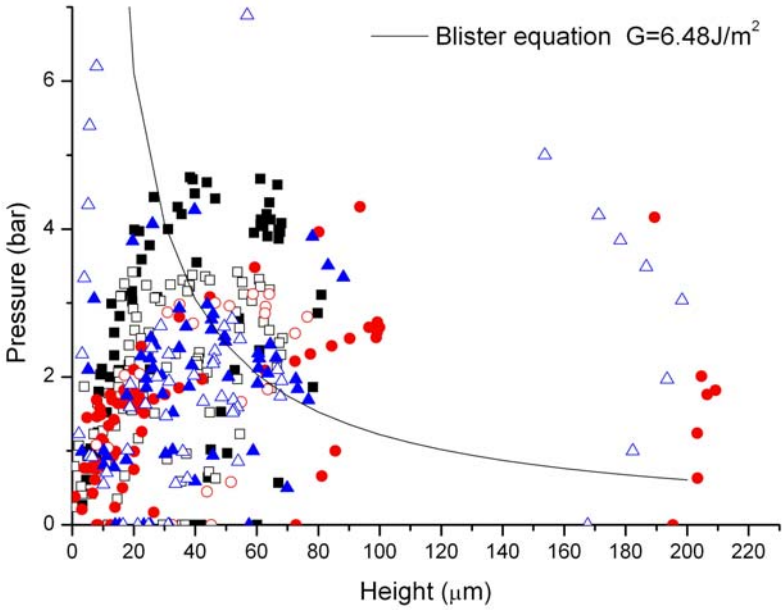

Figure 5-13: The experimental data acquired from blister test and the fitting blister equation, G_{ci}= 6.48 J/m^2. Ag is fired at 850℃ and $BaTiO_3$ is fired at 1440℃. The average surface roughness of $BaTiO_3$ substrate is 0.15 μm.

In general, larger surface roughness enhances adhesion strength of coatings. This effect is attributed to so called mechanical anchoring due to interface asperities. This can be interpreted as a large value of the interfacial crack propagation energy because of the longer and more tortuous crack path along the interface.

Our experimental results in the present research appear to be contrary. We may moderate this conclusion by considering the Weibull moduli. The Weibull modulus of 1440D is about only 2, see Figure 5-14, which means that the strength distribution is very wide. The Weibull modulus of 1440S is 4, which is similar to the results discussed above because the grinding procedure is the same. The results of energy release rate vary from 1 to 9 J/m^2 for 1440D. Although the substrate average roughness are not very different, in this case, a different surface preparation resulting in a larger surface roughness may mean that there are many large defects on the substrate surface.

Since we cannot control defect to be distributed uniformly on the surface, the local roughness may have a wide range on substrate. One may also presume that many more unbonded, undetectable nano-cavities may be present at the rougher interface. The crack propagation being governed by the larger defects on the crack path, this might explains the difference between 1440S and 1440D and the wide scattering of results in the second case.

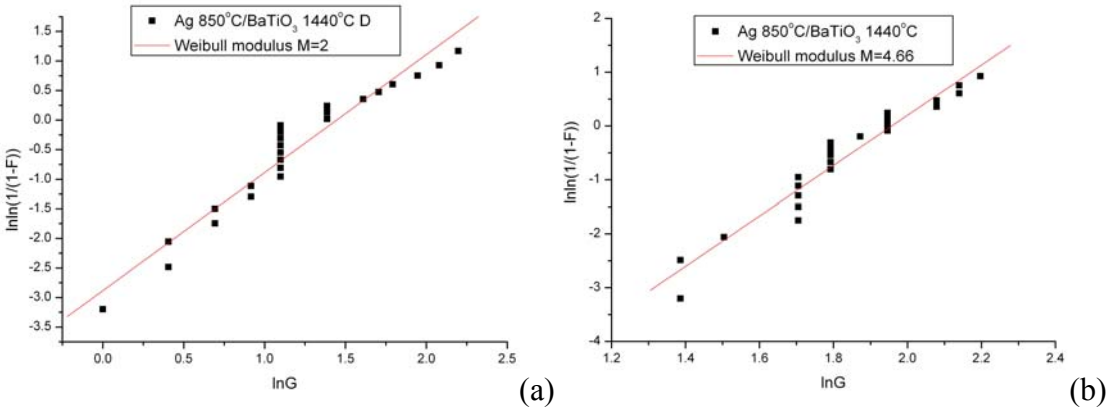

Figure 5-14: Weibull modulus plots of (a) 1440D and (b) 1440S.

Similarly, Table 5-3 shows the results of critical energy release rates G_{ci} of the $BaTiO_3$ (fired at 1350°C for 2 h)/Ag interfaces for different substrate surface treatments. The grinding procedure is the same as for $BaTiO_3$ sintered at 1440°C. The roughness of the substrate of the discs which were ground with fine SiC particles, marked as 1350S, is about 0.19 μm. The roughness of the discs which were ground with diamond particles, marked as 1350D, is about 0.21 μm.

The average G_{ci} of 1350S is about 6.6 J/m^2 and that of 1350D is about 3.88 J/m^2. Figure 5-8 and 5-15 show the experimental results of 1350S and 1350D respectively with the fitting blister equation of average interface energy release rate.

Table 5-3 shows the same trend as mentioned before for 1440S and 1440D. It seems that surface grinding method influences interface adhesion strength significantly. More research work is needed to understand the relationship between roughness distribution and energy release rate of interfacial cracks, with more complete characterization of substrate surface geometry.

Table 5-3: The resulting critical energy release rates G_{ci} of the $BaTiO_3$/Ag interfaces for different substrate surface roughness (the firing temperature of $BaTiO_3$ is 1350℃ for 2 h).

Substrate roughness	G_c (J/m^2)of successive pressurizations	Sample no.							
		1	2	3	4	5	6	7	Average
0.21(μm)	G_{c1}	1.8	6	3	2	8		4.5	
	G_{c2}	4	4.5	3	2	3		5	
	G_{c3}	5			2	3		6	
	G_{c4}	5.5			2			5.5	
	G_{c5}	3.5			2			4.5	
	G_{c6}							3.5	
	Average (J/m^2)	3.96	5.25	3	2		4.67	4.83	3.88

0.19(μm)	G_{c1}	6	8	6	4.5	6	7	6	
	G_{c2}		9	7	7		8	7	
	G_{c3}			6.5	7		6		
	G_{c4}				5				
	G_{c5}				5				
	Average (J/m^2)	6	8.5	6.5	5.7	6	7	6.5	6.60

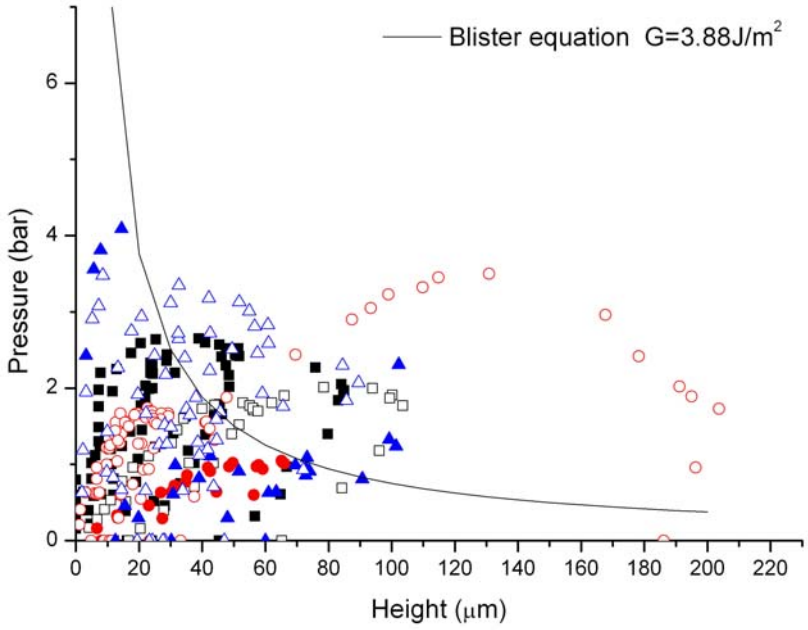

Figure 5-15: The experimental data acquired from blister test and the fitting blister equation, for 3.88 J/m^2. Ag is fired at 850℃ and $BaTiO_3$ is fired at 1350℃. The average surface roughness of $BaTiO_3$ substrate is 0.21μm.

1.1.3. Influence of different substrate firing temperature

Figure 5-16 shows the X-ray diffraction pattern of $BaTiO_3$ sintered at two different temperatures: 1350 and 1440℃. No phase change is found in X-ray diffraction pattern, so the influence of phase composition will not be concerned.

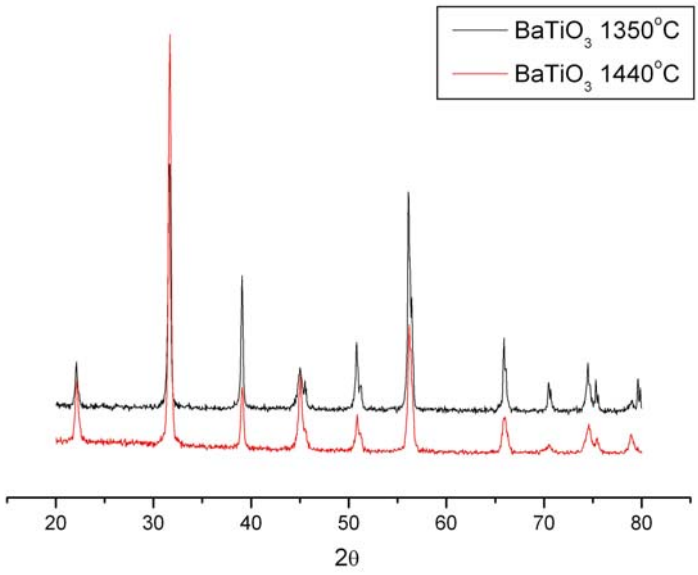

Figure 5-16: The X-ray diffraction pattern of $BaTiO_3$ sintered at two different temperatures.

Barium titanate is a material in which the grains tend to grow abnormally during sintering. The SEM picture of Figure 5-17 shows the microstructure of $BaTiO_3$. Figure 5-17(a) illustrates the $BaTiO_3$ fired at 1350℃ for 2 hours. The grain size grain is about 80μm. When firing temperature is increasing to 1440℃ for 2 hours the grains continue to grow and the grain size increases to more than 200μm (Figure 5-17(b)).

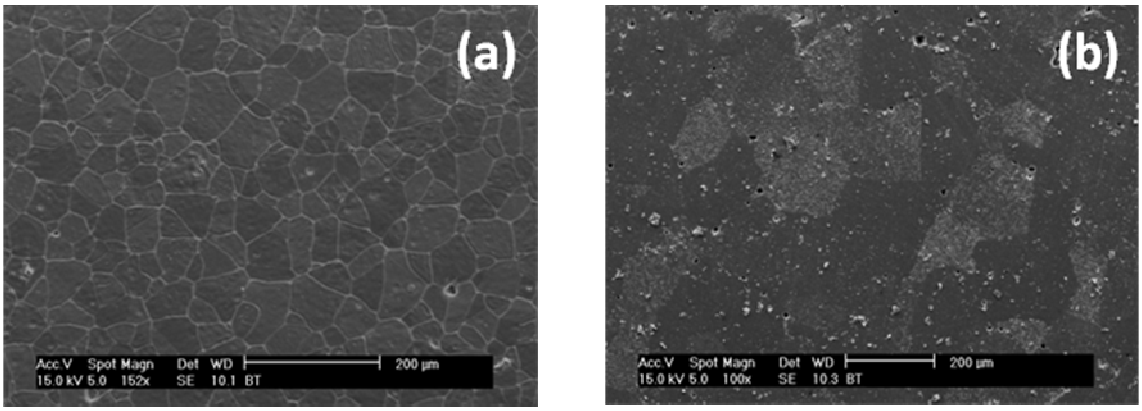

Figure 5-17: The microstructure of $BaTiO_3$ fired at (a) 1350℃ (b) 1440℃ for two hours (SEM).

From the experimental results shown in the previous section, Table 2-5 bring together the results of critical energy release rates G_{ci} of the $BaTiO_3$ /Ag interfaces for different substrate firing temperature. The $BaTiO_3$ were sintered at 1350°C and 1440°C

respectively, the surface treating process is the same. The roughness of ceramic substrates both are 0.21μm. The G_{ci} of Ag/$BaTiO_3$ interface is about 3.8 J/m^2 for both different substrates (Table 5-4). This result indicates that the size of abnormal growth grain does not influence the interface adhesion strength too much.

Table 5-4: The resulting critical energy release rates G_{ci} of the $BaTiO_3$/Ag interfaces for different substrate firing temperature.

Firing temperature	Substrate roughness	Average G_c of each specimen	Sample no.							
			1	2	3	4	5	6	7	Average
1350(℃)	0.21(μm)	G_c (J/m^2)	3.96	5.25	3	2		4.67	4.83	3.88
1440(℃)	0.21(μm)	G_c (J/m^2)	4.7	1.67	4.13	3.8	1.83	5		3.73

1.2. Nickel (Ni)/Barium Titanate ($BaTiO_3$)

The structure of metal/ceramic interfaces are important is multilayer ceramic capacitors (MLCCs), as they can affect physical and electrical properties of the devices. Nickel electrode is developed and used in MLCCs instead of silver electrode, which is widely used so far in MLCCs, to make the devices cost-down. Therefore, the adhesion strength of Ni/$BaTiO_3$ interface is studied in this section.

Figure 5-18 denotes the experimental data and the average critical energy release rates G_{ci} of the Ni/$BaTiO_3$ interfaces measured by blister test. The Ni films were fired at 1200°C in argon atmosphere to avoid nickel oxidation. Because the specimen preparation of blister test is difficult for this system, only five specimens have been successfully performed in this study. In Figure 5-18 we can observe that Ni does not deform plastically as easily as Ag, only one specimen shown extended plastic deformation. While Ni films begin to form a blister and separate from $BaTiO_3$, the Ni films burst and water leaks from interface making pressure drop. So we cannot use the same specimen to measure interface adhesion again, as we do in the Ag/$BaTiO_3$ system.

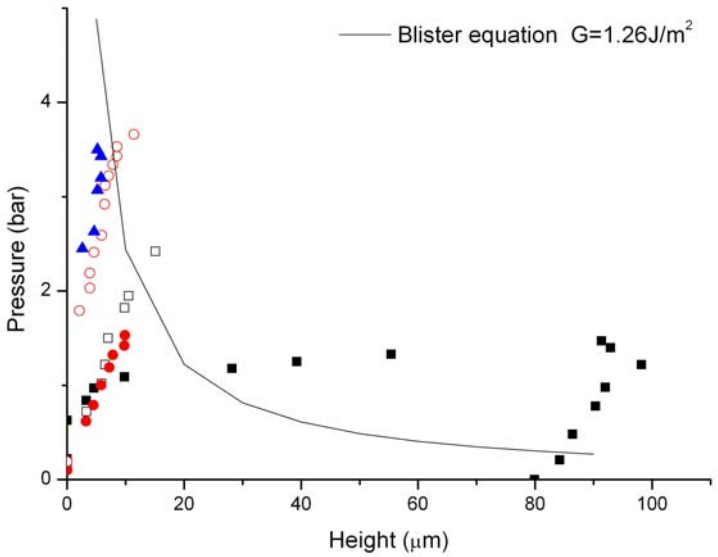

Figure 5-18: The experimental data and critical energy release rates G_{ci} of the $BaTiO_3$/Ni interface, with the fitting blister equation for 1.26J/m^2.

The average G_{ci} of the Ni/$BaTiO_3$ is about 1.26 J/m^2. This value is close to the usual estimates of the thermodynamical work of adhesion of metal/ceramic interfaces alone, around 1 J/m^2.

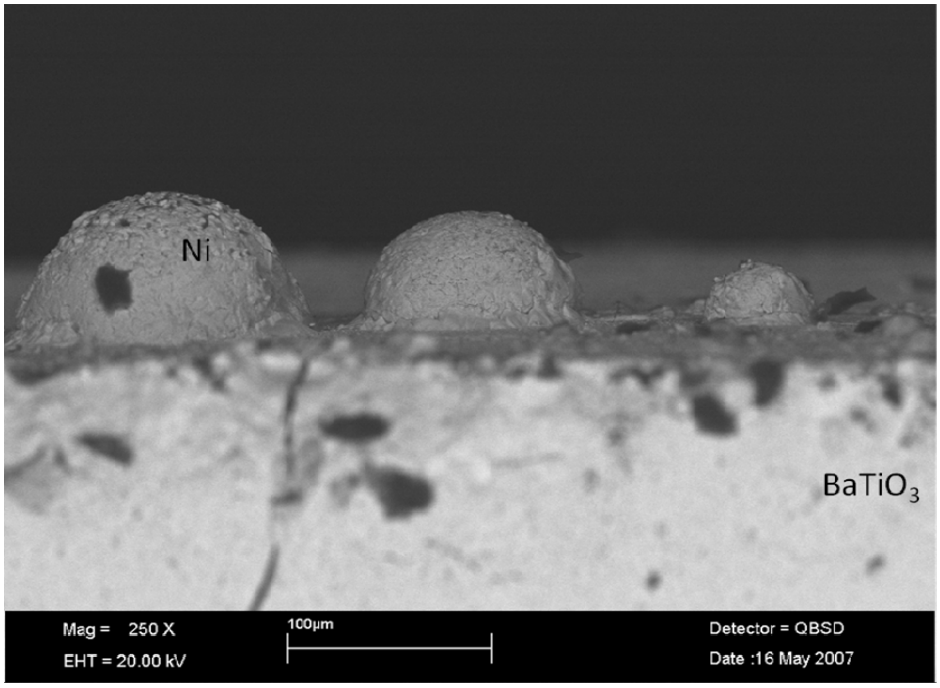

Figure 5-19: Nickel film fired over the melting point on barium titanate substrate in argon atmosphere.

In the case of Ni/$BaTiO_3$ interfaces, the contact angle of sessile drops in the Ni/$BaTiO_3$ system is indeed about 90 **[Sugihara 1990]** while the surface energy of

nickel is 2.45 J/m^2 **[Skriver 1992]**. Thus, W_a of Ni/$BaTiO_3$ interface can be estimated to be around 2.45 J/m^2. But the crack propagation energy G_{ci} is lower than W_a in this study. Consequently, other effects must be involved which reduce the adhesion of Ni/$BaTiO_3$ interface. Ni on $BaTiO_3$ gradually becomes hemispherical shape above the melting point, see Figure 5-19, and the Ni is not wetting well on the $BaTiO_3$.

According to literature, metallic interfacial reaction layer forms in Ni/$BaTiO_3$ interface at high temperature in reducing atmosphere. The major composition of this interfacial layer is Ni, also containing some Ti and Ba. The formation of the interfacial layer is associated with the extreme low oxygen concentration in $BaTiO_3$ grain regions next to the Ni electrode **[Yang 2005]**. The reaction which produces the Ni/$BaTiO_3$ interfacial layer may induce some mismatch of mechanical properties at the interface. Thus, sintering of Ni/$BaTiO_3$ causes stresses and these stresses cannot be released during sintering, which could lead to crack formation or delamination **[Kinemuchi 2005]**. Figure 5-20 shows a cross-section view of Ni/$BaTiO_3$ interface by Scanning Electron Microscopy. Obviously there are many defects and decohesions in the Ni/$BaTiO_3$ interface. These defects could be created during the firing process and be propagated by residual stresses. The cause of the residual stresses is due to the difference of thermal behavior between Ni Paste and $BaTiO_3$ substrate during firing procedure.

The residual stresses in Ni/$BaTiO_3$ MLCCs can reach to more than 100 MPa in particular directions **[Lee 2003, Shin 2003]**. The residual stresses in Ag/$BaTiO_3$ LTCC are only about 1MPa **[Lin 2004]**, hence the residual stresses in Ag/$BaTiO_3$ don't create similar cracks in interface. These results are consistent with our observations.

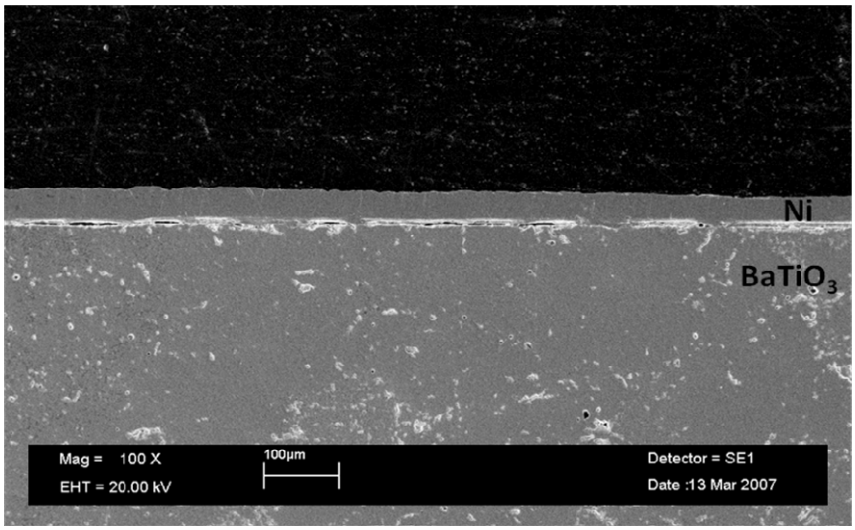

Figure 5-20: The cross-section view of Ni/$BaTiO_3$ interface

Porosity and decohesion at the interface affect adhesion strength significantly, as discussed in section 1.1. High residual stresses produce cracks in Ni/$BaTiO_3$ interface, most of them are large. Accurate identification of porosity in interface is difficult, but we assume that the porosity is more than 40% from cross-section view (Figure 5-20). Remembering Figure 5-11 for the Ag/BaTiO3 interface, we conclude that the results of blister test (1.26 J/m^2) is reasonable, due to the G_{ci} decreases while porosity increases.

Figure 5-21 shows the experimental data and the average G_{ci} of the Ni/$BaTiO_3$ interfaces measured by blister test, when Ni films were first fired at 1000℃ for 1h in argon and air mix atmosphere, and then fired at 1200℃ in 5% hydrogen and 95% nitrogen atmosphere to reduce nickel oxidation to pure nickel. The average critical energy release rate is about 1.06J/m^2.

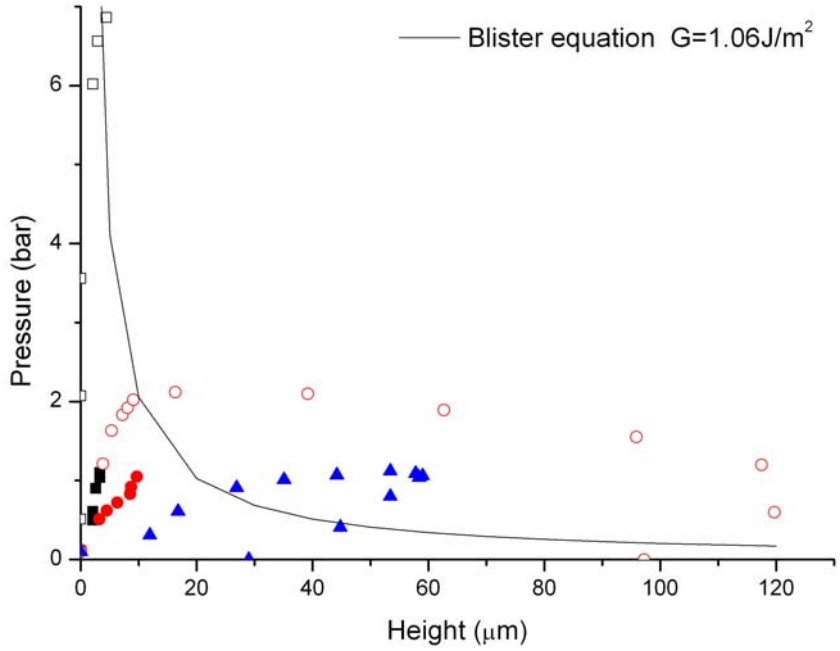

Figure 5-21: The experimental data and critical energy release rates G_{ci} of the interface between $BaTiO_3$ and reduced Ni, with the fitting blister equation for 1.06J/m^2.

Table 5-5 summarizes the crack propagation energy of the interface between barium titanate and nickel. Regardless of firing atmosphere, the energy release rates are about 1 J/m^2. The cracks between nickel and barium titanate, which are induced by residual stresses during firing process, seem to play a major role in adhesion. To fabricate uniform and full contact Ni/$BaTiO_3$ interface, it is necessary to apply a permanent pressure normal to the metal/ceramic interfaces during sintering **[Kinemuchi 2005]**.

Table 5-5: The resulting critical energy release rates G_{ci} of the $BaTiO_3$/Ni interfaces.

Firing temperature	Atmosphere	G_c of successive pressurizations	Sample no.					
			1	2	3	4	5	Average
1200(℃)	99%Ar	G_c (J/m^2)	1.3	1.6	0.8	2	0.6	1.26
1200(℃)	5%H_2 and 95%N_2	G_c (J/m^2)	0.2	1	0.6	1.5	2	1.06

1.3. Nickel (Ni)/Silver (Ag)/ Barium Titanate ($BaTiO_3$)

As mentioned in section 1.1, the plastic deformation affects adhesion measurement a lot. Although we propose a method to correct for the great part of the effect of plastic deformation in blister test, plastic deformation still takes place and may influences the experimental results slightly. So we tried the super-layer technique to reduce the plastic deformation of silver films during the blister test. The superlayer technique is based on increasing the resulting film thickness by putting a stiff overlayer (superlayer) on top of the tested structure. Since the Ni films have higher stiffness, we put Ni film on the Ag film. Specimens of Ag/$BaTiO_3$ were fired at 850°C for 1h (1350S) in air and then nickel paste was screen printed on them to make a sandwich structure (Ni)/ (Ag)/ ($BaTiO_3$). The specimens were fired again at 850°C for 1h under argon atmosphere to sinter nickel paste and to avoid nickel oxidation. Sintering at such low temperature as 850℃ is expected to reduce the influence of residual stress.

Figure 5-22 illustrates the blister test data of Ni/Ag/$BaTiO_3$. This diagram shows that the plastic deformation has been successfully reduced. The metal film had been pulled to observe the position of crack propagation after testing. The crack has propagated in Ag/$BaTiO_3$ interface, not in Ni/Ag interface.

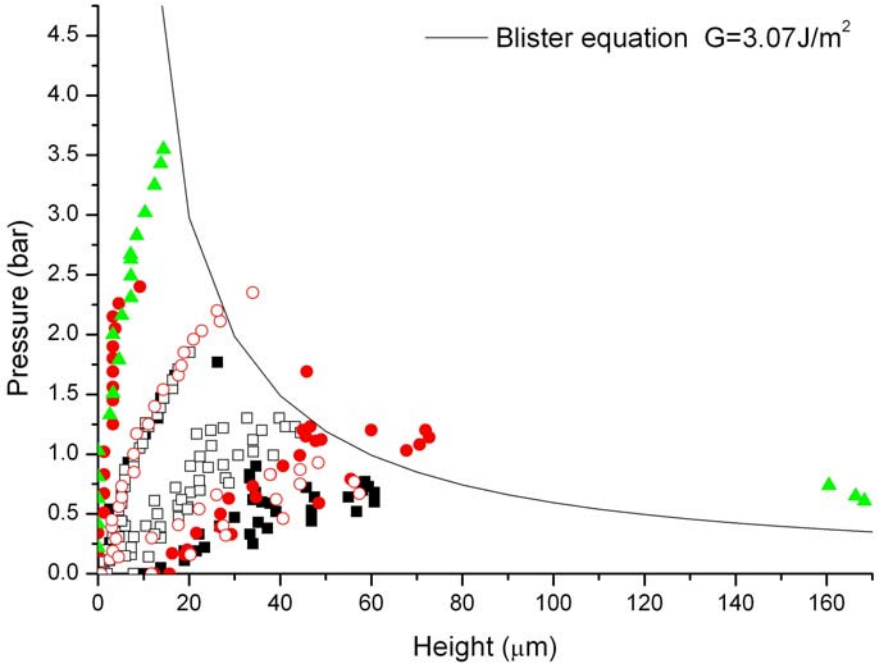

Figure 5-22: The blister test data of Ni/Ag/$BaTiO_3$.

Table 5-6 lists the critical energy release rates G_{ci} of the Ni/Ag/$BaTiO_3$ structure. The average G_{ci} is 3.07 J/m^2. Compared to the results of Ag/$BaTiO_3$ (G_{ci} = 6.6 J/m^2, Ag fired at same temperature), the addition of nickel film reduces the Ag/$BaTiO_3$ interface adhesion.

Table 5-6: The critical energy release rates G_{ci} of the Ni/Ag/$BaTiO_3$ structure.

G_c of successive pressurizations	Sample no.					
	1	2	3	4	5	Average
G_{c1} (J/m^2)	4	2.5	3.5	3	2	
G_{c2} (J/m^2)		3.4	4	2	4	
G_{c3} (J/m^2)		3.4		2		
Average (J/m^2)	4	3.1	3.75	2.33	3	3.07

Figure 5-23 shows the cross section view of Ni/ Ag/ $BaTiO_3$ sandwich structure. The upper layer is the Ni film, middle layer is the Ag film and lower layer is $BaTiO_3$. There are some pores in Ag/$BaTiO_3$ interface which are not observed in simple Ag/$BaTiO_3$ bi-material. The thermal misfit between nickel film and silver film during the second firing may cause these pores in Ag/$BaTiO_3$ interface. We supposed that the low firing temperature could reduce the influence of residual stresses on metal/oxide interface, but

obviously they still induce some crack propagation in $Ag/BaTiO_3$ interface. As introduced in section 1.1.1., it seems logical to conclude that the increased pores fraction in interface will reduce the adhesion strength, which explains why the metal/oxide interface adhesion strength decreases in $Ni/Ag/BaTiO_3$ sandwich structure.

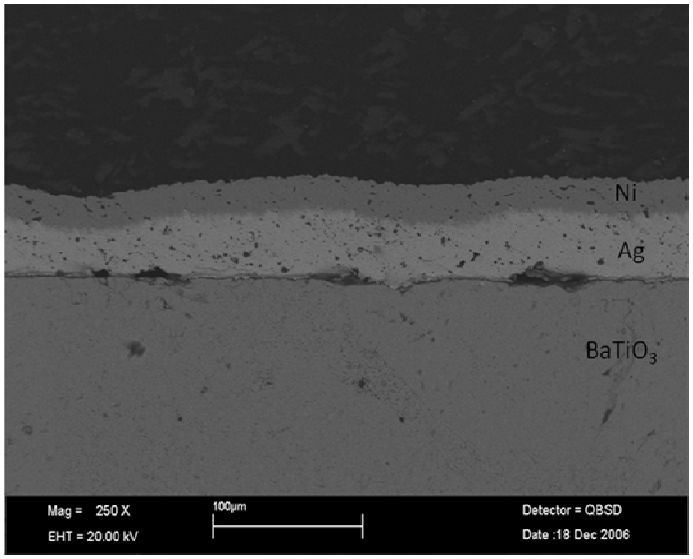

Figure 5-23: the cross section view of Ni/ Ag/ $BaTiO_3$ sandwich structure, upper layer is Ni film, middle layer is Ag film and lower layer is $BaTiO_3$.

1.4. Silver (Ag)/Nickel (Ni)

A sandwich structure (super-layer technique) has been successful used to reduce the plastic deformation of Ag. To avoid crack propagation between the super-layer and the metal film, the interface between the super-layer and the metal film must be stronger than the metal/oxide interface. The conventional fracture energy of our metal/oxide interface is less than 10 J/m^2, so the energy release rate of super-layer and metal film interface must be more 10 J/m^2. Therefore, the adhesion between silver and nickel should be measurable by blister test.

A pure nickel disc with a hole in central part is used as a substrate for blister test. Figure 5-24 shows the blister test data of Ag/Ni. The silver films fracture before debonding from Ni substrate. Therefore, it has been impossible to obtain energy release rate of Ag/Ni interface by blister test. Similar to most of the adhesion measurement techniques the blister test is useless for very strong interfaces and can only provide an estimate for a lower limit of G_{ci}. Although we cannot obtain precise result of Ag/Ni adhesion strength, we could estimate that the G_{ci} for Ag/Ni interface will be greater than 30 J/m^2 from Figure 5-24 (including energy absorbed by plastic deformation).

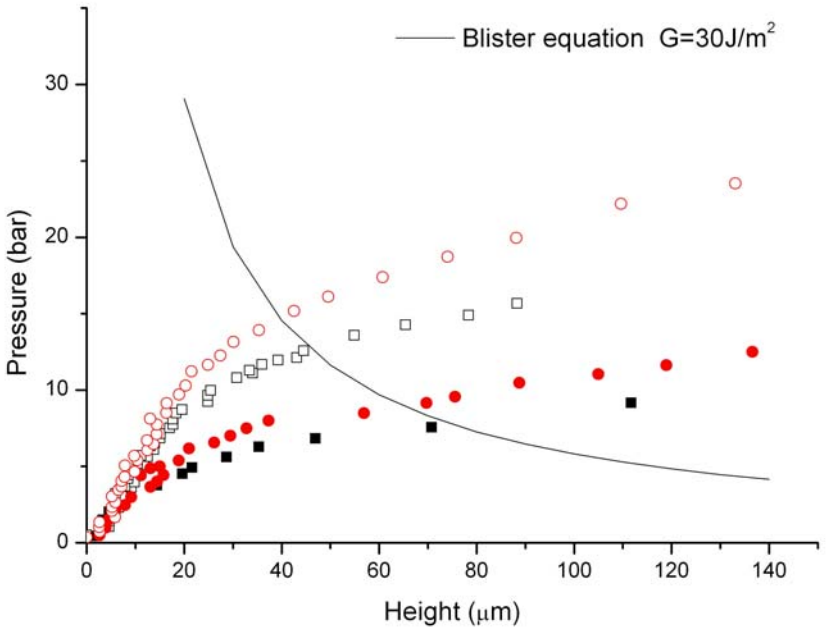

Figure 5-24: The blister test data of Ag/Ni interface adhesion.

2. Indentation test

Indentation can be used to de-laminate the film from the substrate in the case of a weakly bonded film, thus measuring the film coating interfacial strength. Three kinds of Vickers indentation are discussed in this section. First, indentations are performed perpendicular to the film surface (normal indentation test). The second and the third are indentations apply on the cross-section of film/substrate specimens; on interface (interface indentation test) and on substrate (cross-sectional indentation test) particularly.

2.1. Normal indentation test

When an indentation is made on a thin ductile coating surface, the coating arround the indent is under compressive stress and begins to delaminate from substrate to release compressive stress by buckling. If the coating is thick or has a high stiffness, a shear crack may occur and propagates down to the interface, delaminating the coating from the substrate around the indentation (Figure 5-25). The expression proposed by Toonder et al. **[Toonder 2002]** may be used to determine the adhesion (see chapter Ⅲ, section 3.1.):

$$G = 1.42\frac{Eh^5}{L^4}\left(\frac{(a/L)+(\beta_c\pi/2)}{(a/L)+\beta_c\pi}\right)^2 + \frac{h(1-\nu)\sigma_r^2}{E} + \frac{3.36(1-\nu)h^3\sigma_r}{L^2}\left(\frac{(a/L)+(\beta_c\pi/2)}{(a/L)+\beta_c\pi}\right) \quad (3\text{-}1)$$

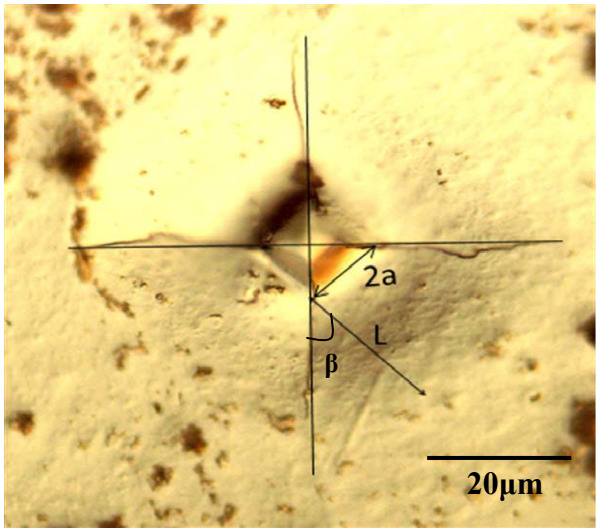

Figure 5-25: Indentation induced of a Ni coating (optical micrograph).

Silver and nickel thin films attach on $BaTiO_3$ substrates are used to quantify the adhesion by normal indentation test. We assume that residual stresses are small enough to be neglected in first approximation, then the expression can be rewritten as

$$G = 1.42\frac{Eh^5}{L^4}\left(\frac{(a/L)+(\beta_c\pi/2)}{(a/L)+\beta_c\pi}\right)^2 \qquad (5\text{-}1)$$

where E is the Young's modulus of the coating; h is the thickness of the coating; v is the Poisson's ratio of the coating; σ_r is the residual stress in the coating . L, a and β_c define the geometry of the chipped piece. The OM photograph (Figure 5-26) shows the coating detachment during loading of the indentation for a 400 nm thick silver film on $BaTiO_3$ substrate. At the indentation load 0.147 N, silver film bulges and separates from its substrate. While loading is 0.245 N, the Ag film begins spalling extension.

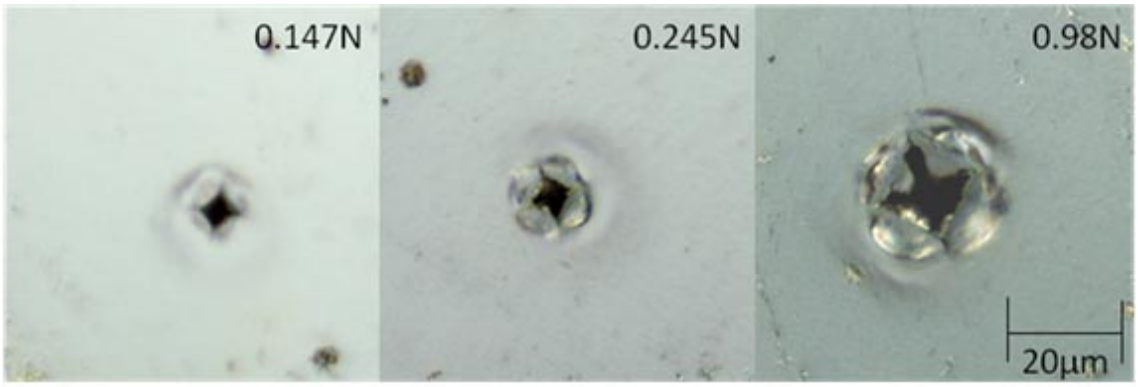

Figure 5-26: Coating detachment during loading of the indentation for a 400 nm thick silver film on $BaTiO_3$ substrate (optical microscopy).

The coating detachment during loading of the indentation for a 400 nm thick nickel film on $BaTiO_3$ substrate is showed in Figure 5-27. Nickel film also bulges and separates from its substrate around the indentation. Large loading may cause nickel film break during indentation

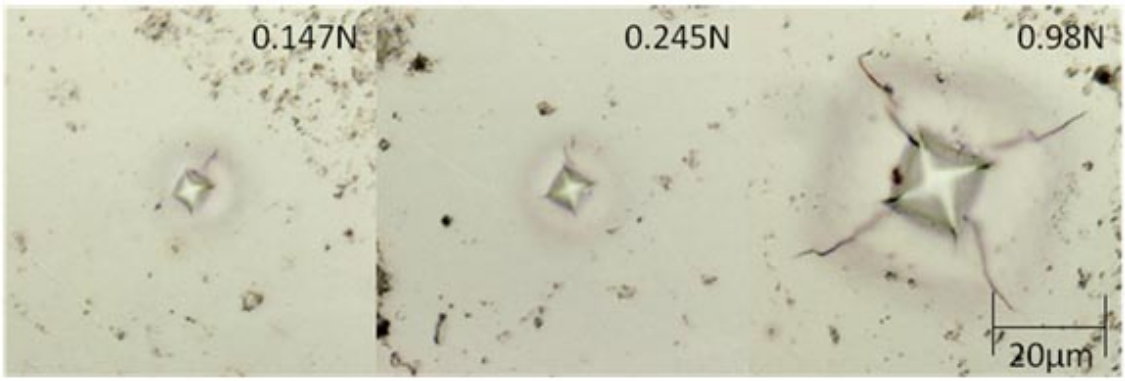

Figure 5-27: Coating detachment during loading of the indentation for a 400nm thick nickel film on $BaTiO_3$ substrate (optical microscopy).

The length L of the interfacial crack is inferred from the measurement of the radius of the bulge surrounding the indent. The measured interfacial crack radius increases almost linearly with load both in silver and nickel coatings.

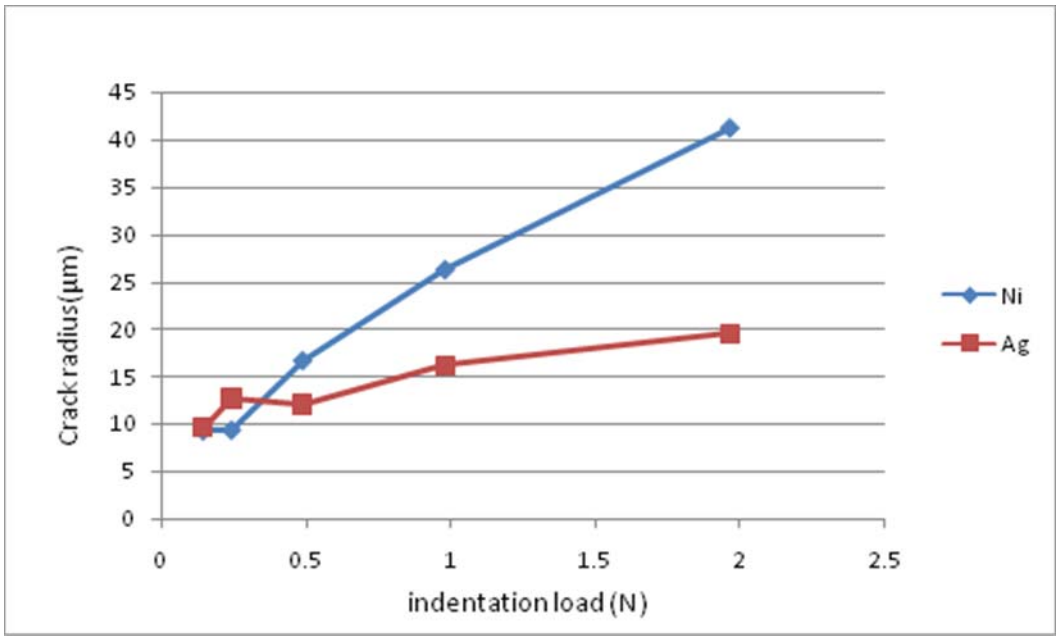

Figure 5-28: Plot of indentation load versus interfacial crack radius after normal indentation.

Equation (5-1) is used to calculate adhesion energy. This equation is very sensitive to the precise values of thickness and crack length. Hence its results must be regarded as dubious and they are widely dispersed indeed (see Figure 5-29).

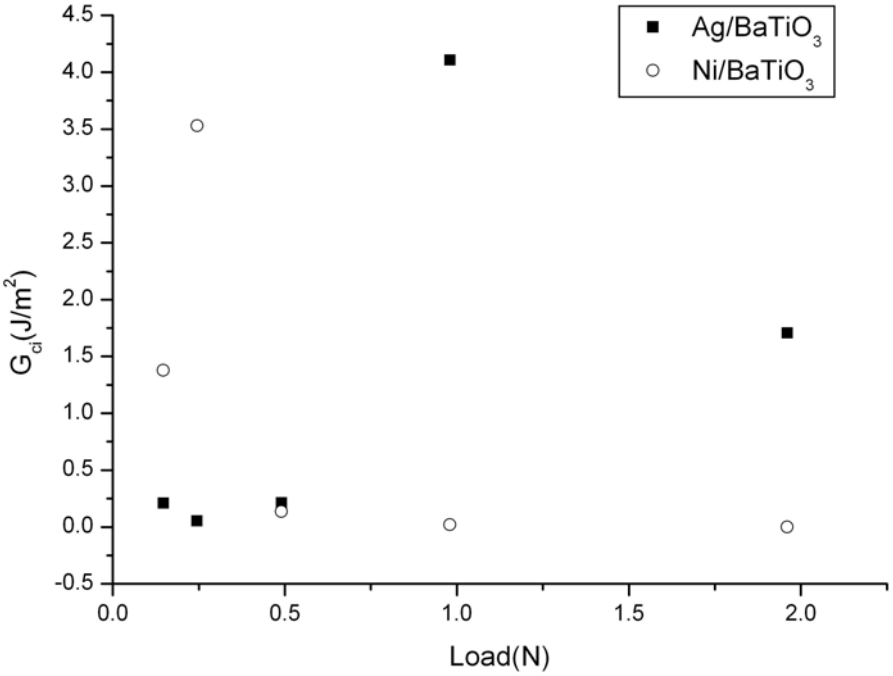

Figure 5-29: The energy of interfacial crack extension of silver and nickel thin coatings on barium titanate, from normal indentation tests.

The energy of interfacial crack extension of thin silver coating on barium titanate varies from 0.05 to 4.1 J/m^2. The G_{ci} of thin nickel coating on barium titanate changes from 0.02 to 3.5 J/m^2. These large distributions may be mostly due to the incorrect crack length measurement and plastic deformation of the coatings.

However, it must be recalled that these thin coatings have been prepared by a specific way (see chapter Ⅳ, section 3.2.2.). Therefore, their adhesion strength to $BaTiO_3$ substrate cannot be compared forwardly straight to the results of blister tests.

2.2. Interface indentation test

For these experiments silver paste is fired at 850°C for 1h on the $BaTiO_3$ substrate. We use the specimens 1350D to perform interface indentation test. A cross-section view is presented in Figure 5-30. Upper part is silver film and lower part is barium titanate. Vickers indentation is performed as exactly as possible on the Ag/$BaTiO_3$ interface. A first obvious experimental difficulty consists in adjusting the indent for tip to be coincident with the coating/substrate interface, and the diagonal of the indentation along the interface direction.

It is very difficult to identify clearly the exact length of indentation induced crack in interface (Figure 5-30(a)). We need to use backscattered electron mode to enhance contrast in SEM observation in order to see the crack (Figure 5-30(b)). The crack opening is very small so we can hardly define the crack length, even by using some

image analysis. Thus measuring the value of the half-diagonal of the indent for each indent and the length of the crack in the interface are not easy and care must be taken during experimental and analysis works.

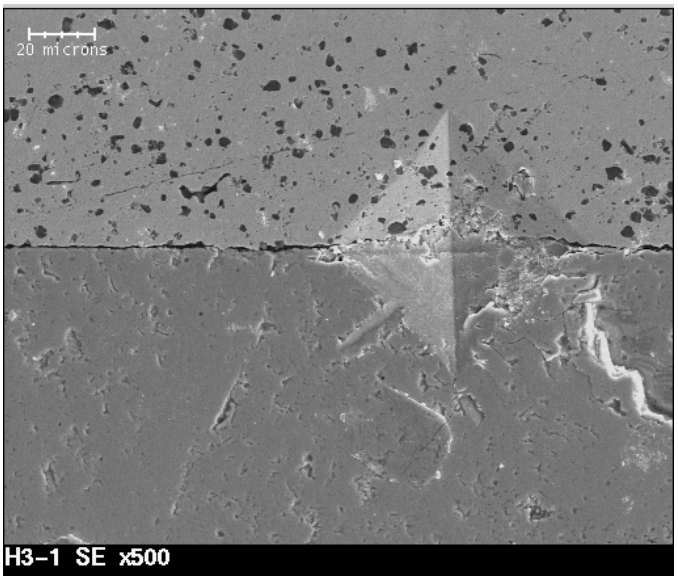

(a)

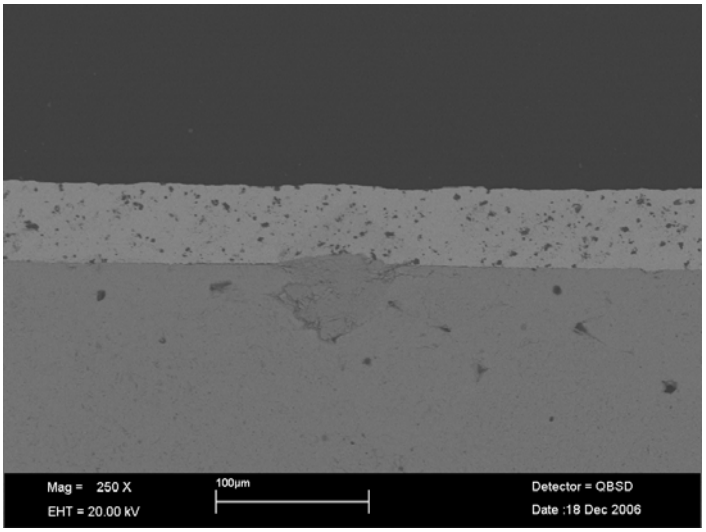

(b)

Figure 5-30: Cross-section of Ag/$BaTiO_3$ interface (a) SE mode (b) BSE mode (scanning electron microscopy).

Equations (3-2), (3-7) and (3-9) have been adopted to calculate the critical crack extension force (G_{ci}).

$$K_c = \alpha \frac{P}{a_c^{3/2}} \left(\frac{E}{H} \right)^{1/2} \tag{3-2}$$

$$\left(\frac{E}{H}\right)^{1/2} = \frac{(E/H)_S^{1/2}}{1+(H_s/H_F)^{1/2}} + \frac{(E/H)_F^{1/2}}{1+(H_F/H_S)^{1/2}} \tag{3-7}$$

$$G = \frac{(1-\beta^2)}{E_*}\left(K_I^2\right) \tag{3-9}$$

The parameters used in the equations are listed in Table 5-7.

Table 5-7: Parameters used to calculate G_{ci} in interface indentation test.

	Silver	Barium Titanate
Young's modulus (GPa)	76	178
Hardness(Vickers)	25	48
Poisson's ratio	0.37	0.35
Shear modulus(GPa)	27.8	35

Table 5-8: G_{ci} in interface indentation test for Ag/$BaTiO_3$ (1350D) specimens.

Number	1	2	3	4	5	6
crack length (μm)	35	62.55	59.25	48.9	50	61.4
G_{ci} (J/m^2)	2.54	0.445	0.524	0.932	0.871	0.471
Number	7	8	9	10	11	average
crack length (μm)	79.15	127	71.6	79.85	72.5	67.9
G_{ci} (J/m^2)	0.22	0.053	0.297	0.214	0.286	0.623

The critical energy release rates of Ag/$BaTiO_3$ (1350D) measured by indentation test are listed in Table 5-8. The film thickness is about 70μm, load is 1.96 N and the average crack length of 11 indentations is about 68μm. If constant α is 0.015 **[Lesage 2001]**, the interface energy release rate is 0.623 J/m^2. Compared to the result of blister test (G_{ci} about 3.8 J/m^2) this value is much smaller. Whereas the constant α is a material-independent constant for Vickers produced radial cracks, we should find out the appropriate fit to this system. Figure 5-31 shows the effect of changing the value of α versus the calculated G_{ci} for the couple of materials of interest here (Ag/$BaTiO_3$) and a_c=67.9 μm. We can see that a very small change of α could lead to values of G_{ci} comparable with those obtained from blister test. So analysis is needed to obtain accurate value of constant α.

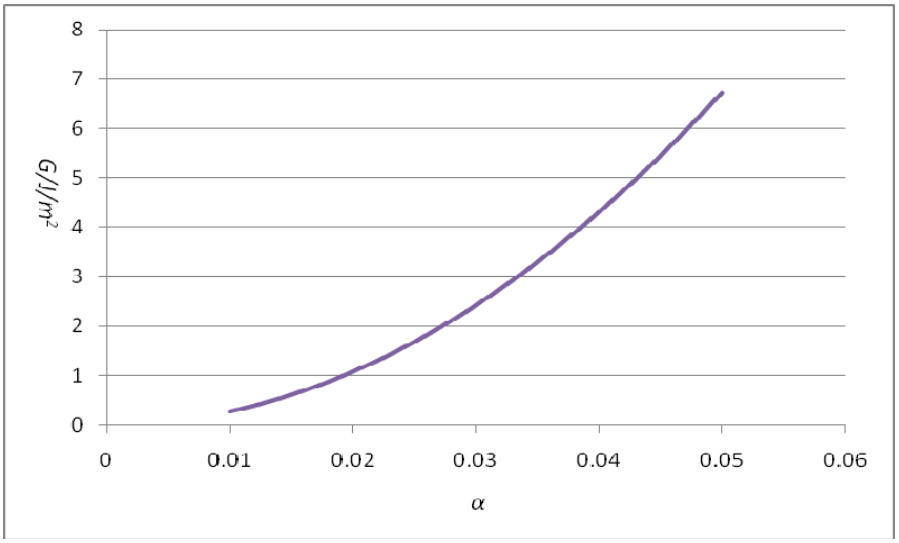

Figure 5-31:The effect of the constant α for interface indentation equation on calculated G_{ci} for $Ag/BaTiO_3$ and a_c=67.9 μm.

2.3. Cross-sectional indentation test

Cross-sectional indentation test is modified from cross-sectional nanoindentation test (CSN test). Cracks are initiated in the brittle barium titanate substrate by indenting with a Vickers diamond tip close to the $Ag/BaTiO_3$ interface. A conventional micro indentation is used to apply this method. Vickers indent is rotated to make the edge of the square indent parallel to the interface. Cracks propagate from two corners of the Vickers indentation towards the metal/oxide interface. The indentation load makes interfacial crack propagate and separate a chip from the brittle substrate, which pushes the film to debond and deflect outward (Figure 5-32).

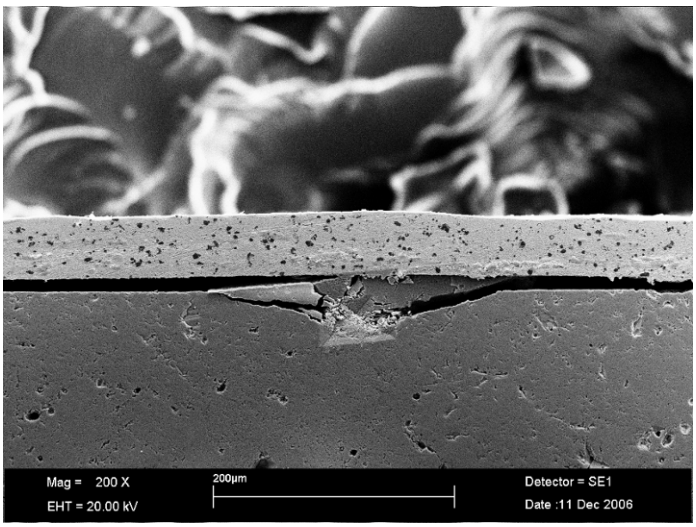

Figure 5-32: The cross-sectional indentation test with a Vickers indent.

Only the $Ag/BaTiO_3$ specimens have been used in our cross-sectional indentation tests. The $Ni/BaTiO_3$ interfaces are weak and full of porosities, so that nickel films are likely to separate from $BaTiO_3$ substrate during the sample preparing process. Indeed sample preparation for cross-sectional indentation test must be carried out carefully to avoid film separation (see chapter Ⅳ, section 3.2.), this is also important for most of interface adhesion measurement methods.

Crack length is measured by SEM photograph as show on Figure 5-33. The end of the crack in interface can be more precisely defined so we estimate that cross-sectional indentation test is more reliable than normal and interface indentation test.

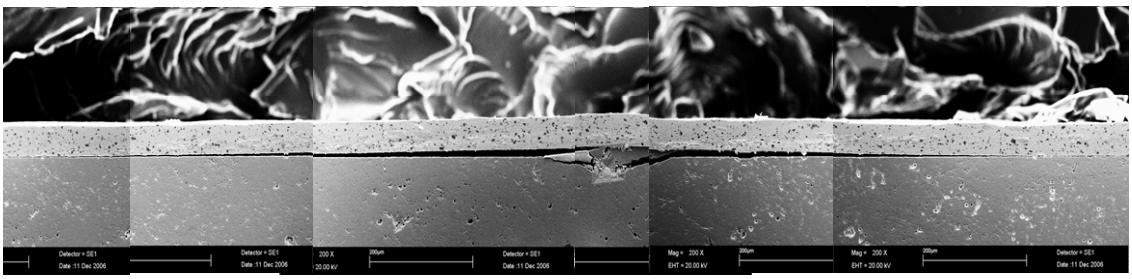

(a)

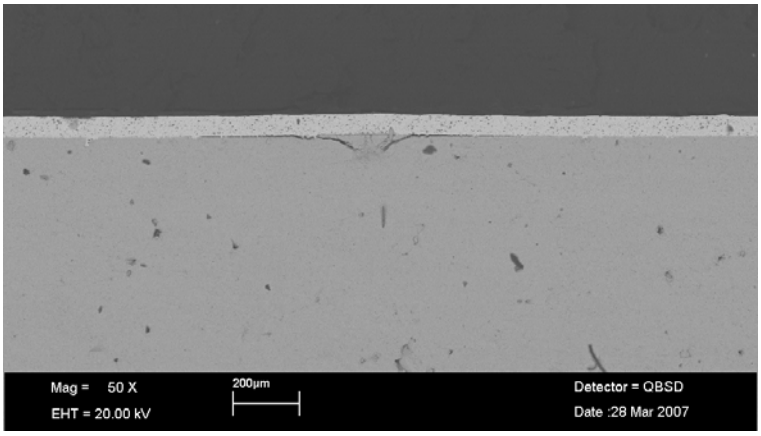

(b)

Figure 5-33: SEM photographs of cross-sectional indentation test with a Vickers indent

There are several models to interpret the results of cross-sectional indentation test: plate model, tapered beams model **[Sanchez 1999]** and restrained edges model **[Li 2006]**. Because of the large extension and small deflection of our interfacial cracks, we also propose a new model based on the blister induced by point load (point load model). All of these models are presented in Chapter 3, and we all use four models to calculate critical interface energy release rate of $Ag/BaTiO_3$ from our experiments. The appropriate formulae are recalled below for each model

Plate model $G = \frac{8Dw_0^2}{a^4}, \qquad D = \frac{Eh^3}{12(1-\nu^2)}$

Tapered beams model $G = \frac{D(1-\nu^2)\cdot w_0^2}{a^4}(2F(\lambda)+\lambda F'(\lambda))_S$

Restrained edges model $G = \frac{4Dw_0^2}{a^4}(2F(\lambda)+\lambda F'(\lambda))_L$

Point load model $G = \frac{F\cos\theta\sin\theta w_0}{\pi a^2}$

The experimental data and calculated energy release rates according to each model are listed in Table 5-9. Tapered beams model leads to the lowest values in four models and point load model leads to the highest.

Table 5-9: Experimental data and calculated interface energy release rate by four models for cross-sectional Vickers indentation tests on Ag/$BaTiO_3$ interfaces.

1350D	*a(μm)*	*b(μm)*	*F(N)*	*h(μm)*	*w_0(μm)*	*b/a*	G_{ci} of different model (J/m^2)			
							Plate	Tapered beams	Restrained edges	Point load
1	1135	31	0.98	60	15	0.03	1.90	0.97	2.07	3.82
2	552	17	0.98	60	6	0.03	4.90	2.55	5.41	6.46
3	702	16	0.98	60	6	0.02	1.30	0.63	1.39	3.99
4	1190	38	0.98	125	3	0.03	0.28	0.15	0.31	0.58
5	2150	153	2.94	125	10	0.07	0.65	0.51	0.87	2.13
average							1.81	0.96	2.01	3.39

1440S	*a(μm)*	*b(μm)*	*F(N)*	*h(μm)*	*w_0(μm)*	*b/a*	G_{ci} of different model (J/m^2)			
							Plate	Tapered beams	Restrained edges	Point load
1	865	30	1.96	85	5	0.03	1.30	0.73	1.46	3.94
2	688	30	1.96	85	3	0.04	1.40	0.85	1.64	4.16
3	808	30	1.96	85	5	0.04	2.12	1.20	2.41	5.03
4	1225	110	1.96	160	4	0.09	1.70	1.54	2.50	1.75
5	880	60	1.96	160	2	0.07	1.60	1.20	2.11	1.69
6	1228	92	1.96	123	5	0.07	1.20	0.96	1.63	2.18
average							1.55	1.08	1.96	3.13

In each model, only elastic strain energy has been considered. Due to the thick film (70µm) and low load (1.96N), the corresponding analysis to account for generalized plasticity effects on interfacial energy has not been adopted in this study. The fracture of the brittle substrate absorbs part of the incident mechanical work (Figure 5-32). But in the first three models, the strain energy of the system is estimated only from its geometrical parameters and material data. Only in the point load blister model, the applied load is needed, which may be perturbed by the fracture and friction of the substrate chip. However, comparing the crack propagation in the brittle substrate with one in interface, we may neglect energy dispersion due to the crack length in substrate which is much smaller than the crack length in interface.

To compare these values with each other, two column graphs are plotted in Figure 5-34 and 5-35. Tapered beam model provides small values in the condition of $b/a<0.1$. Restrained edges and Plate model seem to obtain close values in our case. Point load model is based on the applied load and the others are dependent only on the material properties of the film and substrate. Point load model gives higher values than the others, except for the thickest film (160µm). This may be explained or by an overstatement of the true applied load because of the fraction between the substrate chip, the substrate bulk and the indentor.

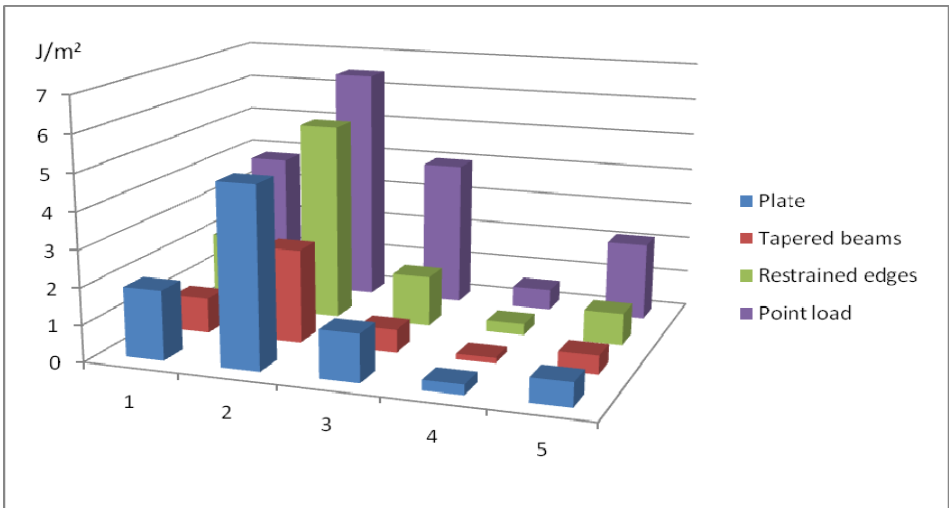

Figure 5-34: G_{ci} of Ag/$BaTiO_3$ (1350D) interface measured by different model on 5 different interface locations.

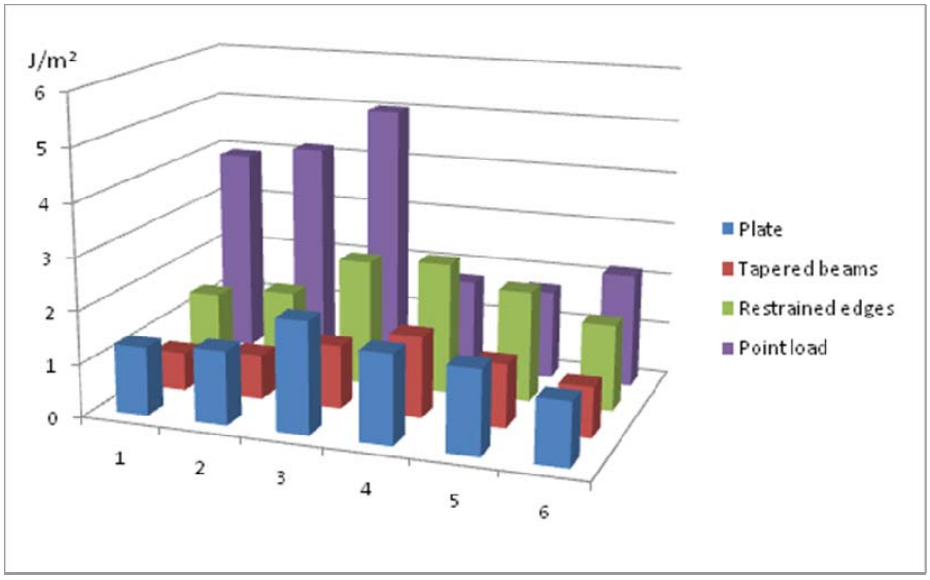

Figure 5-35: G_{ci} of $Ag/BaTiO_3$ (1440S) interface measured by different model on 6 different interface locations.

3. Comparison between blister and indentation test

3.1. Comparison between G_{ci} from normal indentation test with the values from blister test.

Mode mixity of normal indentation test is complex and the experimental measurement are uncertain, which make the value of critical crack propagation energy to disperse in a wide range. Normal indentation test also induces a lot of plastic deformation during film debonding. Moreover, the tested specimens are obtained with a different process. Therefore, we cannot compare the values from this test with the values from blister test.

3.2. Comparison between G_{ci} from interface indentation test with the values from blister test.

For $Ag/BaTiO_3$ interface, the interface adhesion strength measured by interface indentation test is about 0.6 J/m^2. The present model for interface indentation test only considers the fracture mode I, which would imply G_{ci} value from interface indentation smaller than from blister test. This is indeed what we measure. However, the equation used for interface indentation is still not completely developed, especially with non reliable value of the constant α for Vickers indentation. Therefore, precise comparison of G_{ci} with the results of blister test is still difficult.

3.3. Comparison between G_{ci} from cross-sectional indentation test with the values from blister test.

Compare to blister test, the G_{ci} measured by cross-sectional indentation test, using plate, tapered beams and restrained model, are smaller (Figure 5-36). The average critical energy release rate of Ag/$BaTiO_3$ obtained by cross-sectional indentation test (point load model) is similar to the value from blister test; this may be due to the similarity in their mechanical analysis. More theoretic and experimental developments are needed to complete this new adhesion strength test method.

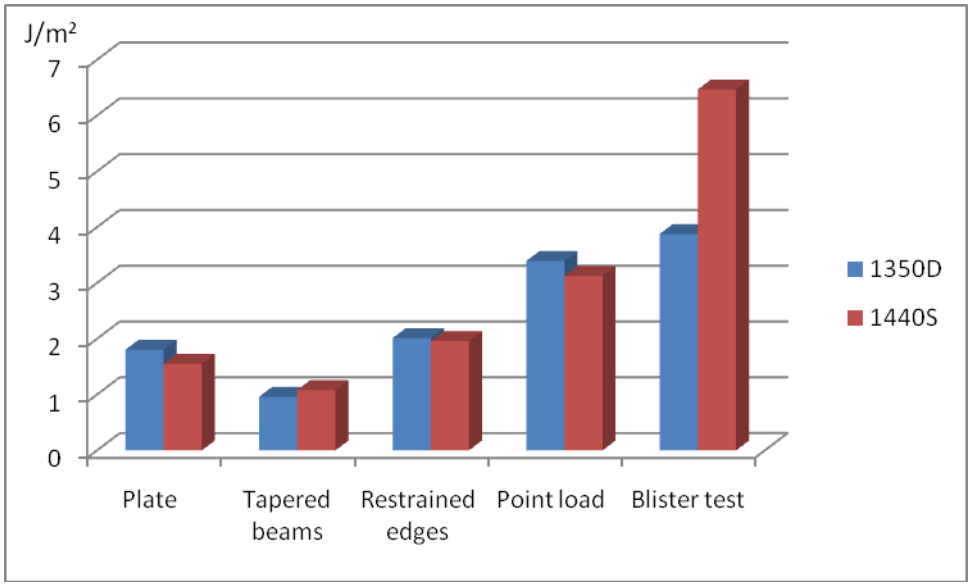

Figure 5-36: G_{ci} of Ag/$BaTiO_3$ interface measured by blister test and different model of cross-sectional indentation test.

4. Conclusions

Four methods are used and developed to measure critical energy release rate of metal/oxide interface: blister test, normal indentation test, interface indentation test and cross-sectional indentation test. The critical energy release rate of Ag/ $BaTiO_3$, Ni/ $BaTiO_3$, Ni/Ag/ $BaTiO_3$ and Ag/Ni interface have been measured.

4.1. Silver (Ag)/Barium Titanate ($BaTiO_3$)

The average value measured by blister test increases from 4.5 J/m^2 to 6.6 J/m^2 while the interface porosity decreases from 11% to 7%. The average value changes from 3.8 J/m^2 to 6.6 J/m^2 with different substrate surface conditions for silver fired at 850°C.

A thin silver film with a thickness of 400 nm has been prepared by thermal coating.

The average G_{ci} measured by normal indentation test is about 1 J/m^2 on this film.

The average G_{ci} measured by interface indentation test is about 0.6 J/m^2 according to the present mechanic model, for the silver fired at 850°C on the barium titanate substrate.

Four models are used in cross-sectional indentation test to calculate crack propagation energy. The average Gci measured by cross-sectional indentation test is about 1.6 J/m^2 calculated by plate model, about 1 J/m^2 calculated by tapered beams model and about 2 J/m^2 calculated by restrained edges model. A new model based on applied point load is developed in this study. The average Gci of Ag/$BaTiO_3$ is about 3.1 J/m^2 wiht this new model.

4.2. Nickel (Ni)/Barium Titanate ($BaTiO_3$)

The average value is about 1 J/m^2 while the Ni film is fired at 1200°C for 2 h on the dense barium titanate. The nickel films are oxidized first and then reduced to fabricate the nickel films attached on the $BaTiO_3$ substrate. Large residual stresses occur during firing process and cause partial debonding of nickel film from barium titanate substrate. These cracks in Ni/$BaTiO_3$ interface reduce the interfacial adhesion strength.

4.3. Nickel (Ni)/Silver (Ag)/ Barium Titanate ($BaTiO_3$)

The average value is about 3.07 J/m^2 from blister test on this system. The crack propagation is along the Ag/$BaTiO_3$ interface. The residual stresses during the sintering process of the nickel paste layer generate pores in Ag/$BaTiO_3$ interface and decreases the interface adhesion strength of Ag/$BaTiO_3$.

4.4. Silver (Ag)/Nickel (Ni)

The silver films fracture before the cracks begin to propagate. No exact value can be measured in Ag/Ni case by using blister test. The average value of interface energy loading is more than 30 J/m^2 before silver film fracture.

In spite of the difficulties for specimen preparation and the wide scattering of measured energies, the blister test seems to be a reliable technique to measure interfacial crack extension energy.

The various indentation techniques which are tried to apply to the same metal/ceramic system appear to be rather unprecise for crack length measurements and difficult to use for crack propagation energy calculations because of the various possible models which provide very different results.

References

[Dupeux 1998] M. Dupeux, A. Bosseboeuf, "*Application of the blister test to adhesion envergy measurements in metal / ceramic film-on-substrate systems*," Interfacial Science in Ceramic Jointing, (1998) pp.319-327.

[Felder 2003] E. Felder, E. Darque-Ceretti, Adhésion et Adhérence, CNRS Edt., Paris, 2003.

[ImageJ] ImageJ, http://rsb.info.nih.gov/ij/

[Kinemuchi 2005] Y. Kinemuchi, S. Uchimura, K. Watari, "*Centrifugal sintering of $BaTiO_3$/Ni layered ceramics*" Journal of the European Ceramics Society, 25 (2005) pp. 2223-2226.

[Lee 2003] S. G. Lee, U. Paik, Y. I. Shin, J.W. Kim, Y. G. Jung, "*Control of residual stresses with post process in $BaTiO_3$-based Ni-MLCCs*" Materials and Design 24 (2003) pp. 169-176.

[Lee 2006] C. Y. Lee, M. Dupeux, W. H. Tuan, "*Adhesion strength of Ag/$BaTiO_3$ interface*" Scripta Materialia 54 (2006) pp.453–457.

[Lesage 2001] J. Lesage, D. Chicot, "*Hardness and adhesion of coating*" Revista de la Facultad de Ingenieria de la U.C.V., Vol. 16, No. 1 (2001) pp.33-38.

[Li 2006] X. F. Li, "*Effects of an elastic substrate on the interfacial adhesion of thin films*" Surface and Coatings Technology 200 (2006) pp.5003-5008.

[Lin 2004] Y. C. Lin, J.H Jean, "*Constrained Sintering of Silver Circuit Paste*", J. Am. Ceram. Soc., 87 (2004) pp.187-91.

[Radi 2001] E. Radi, M. Cristina Porcu. "*Near-tip fields for quasi-static crack growth along the interface between a porous-ductile material and a rigid substrate*", International Journal of Solids and Structures, 38 (2001) pp.8235-8258.

[Sanchez 1999] J. M. Sanchez, S. El-Mansy, B. Sun, T. Scherban, N. Fang, D. Pantuso, W. Ford, M. R. Elizalde, J. M. Martinez-Esnaola, A. Martin-Meizoso, J. Gil-Sevillano, M. Fuentes, J. Maiz. "*Cross-sectional nanoindentation: a new technique for thin film interfacial adhesion characterization*" Acta Materialia 47, (1999) pp.4405-4413.

[Shin 2003] Y. I.. Shin, K. M. Kang, Y. G.. Jung, J. G.. Yeo, S. G. Lee, U. Paik, "*Internal stresses in $BaTiO_3$/Ni MLCCs"*, Journal of the European Ceramic Society 23 (2003) pp.1427-1434.

[Skriver 1992]H. L. Skriver, N. M. Rosengaard, "*Surface energy and work function of elemental metals*", Physical Review B, V.46, N.11, (1992) pp.7157-7168.

[Sugihara 1990]S. Sugihara, K. Okazaki, Application of Ferroelectrics, Proceedings of the 7th IEEE International Symposium, (1990), pp. 432–434.

[Toonder 2002] J. der Toonder, J. Malzbender, G. de With, R. Balkenende, "*Fracture toughness and adhesion energy of sol-gel coatings on glass*" Journal of Materials Research, 17 (2002) pp.224-233.

[Volinsky 2002] A. A. Volinsky, N. R. Moody, W. W. Gerberich, "*Interfacial toughness measurements for thin films on substrates*" Acta Materialia 50 (2002) pp.441–466.

[Yang 2005] G.. Y. Yang, E. C. Dickey, C. A. Randall, "*Interfacial reactions between Ni and $BaTiO_3$: An Analytical Transmission Electron Microscopy Study*", Microsc Microanal 11 (Suppl 2), (2005) pp.232-233.

Chapter VI

General conclusions and future work

The initial purpose of the present work was to study the adhesion strength of metal/ceramic interfaces. The interface between silver and barium titanate was chosen as our model reference system, because of the practical interest of these materials as dielectric and electrode metal in Multi-Layer Ceramic Capacitors (MLCC's) and the previous knowledge in their processing at the *Ceramic Matrix Composite Laboratory*, *Department of Material Science and Engineering, National Taiwan University*.

Similarly, because of the previous experience of the *Laboratoire de Thermodynamique et Physico-Chimie Métallurgiques* at *Université Joseph Fourier* in blister testing of coatings, this technique was chosen as the basic one to obtain quantitative values of adhesion on our metal/ceramic interfaces.

Thus the first and important practical result of this study was to develop an appropriate process to produce specimens with a free-standing Ag membrane over a perforated $BaTiO_3$ substrate, adapted to blister testing.

Specimen preparation:

Concerning the fabrication of ceramic substrate, high hardness and chemical stability of ceramic makes it difficult to perforate a hole into the substrate. Two-step sintering procedure of the ceramic substrate (thickness 2 mm, diameter 25 mm) is used to simplify perforating process. In the first step, the discs were first pre-fired at 1100°C for 1 h to obtain a handling strength with lower relative density. A hole with 3 mm diameter was then machined into the center of the pre-fired discs by using a steel drill. The discs were then sintered at 1350°C or 1440°C for 2 h. Therefore, the ceramic substrate with a hole in central part can be easily produced.

The hole in the substrate is covered with a small circular Ag membrane prepared separately (Ag membrane sintered at 500°C) to produce a free-standing window. Then screen printing with silver paste is performed over the substrate and sintering of the metal layer of interest with the required thickness, between 60 and 200 μm.

This technique has been adapted successfully to produce specimens with variable firing temperatures either for the substrate or for the metal silver layer, with various Ag paste sintering temperatures, surface roughness of the substrate and with Ni layers on $BaTiO_3$ substrates, or Ag layers on Ni substrates. It seems quite possible to derive an appropriate process from this basic technique to prepare any reactive or non-reactive metal/ceramic interface.

Blister test results:

Experimental apparatus of blister test was already setup in *Laboratoire de Thermodynamique et Physico-Chimie Métallurgiques*. Our specimens are suitable for the blister test apparatus and tests were performed to measure the pressure vs. blister deflection curves and deduce the interfacial crack propagation energy of our metal/oxide interfaces.

- Generalized plastic deformation of the metal membrane was observed during the test before or during interface decohesion. We set up a simple graphic procedure to correct for the generalized plastic work dissipated in the metal membrane and determine the interfacial toughness, including only the contribution of the confined plasticity at the crack tip. This procedure may obviously be useful for any plastic coating submitted to blister testing, and it has been described in a related journal article.

- On series of specimens with the same preparation conditions, the dispersed distribution of the obtained energy values satisfy to Weibull statistical law. Even if the Weibull modulus is small, this allows reliable comparison between the average values of the various series of results obtained from various classes of specimens.

- Since the sintered Ag membranes keep some pore fraction depending on their sintering temperature, the experimental results brought evidence for a non-linear dependence of the interfacial crack propagation energy on the interfacial pore fraction. Theoretical work is presently in progress to develop appropriate modeling of this effect. More experimental results obtained by testing interfaces with controlled porosity rates on a larger interval would help to validate or improve this model.

- Surprisingly, adhesion energies differing up to a factor of 2 are determined for $Ag/BaTiO_3$ interfaces with similar roughness, but different preparation routes for substrate polishing. More detailed exploration is needed to explain this effect of substrate preparation.

- The effect of interfacial chemistry is difficult to decide from comparing Ni to Ag metal layer. Indeed, Ni membranes seem to contain residual stresses which produce detrimental effect on adhesion by causing many interfacial debonded zones right after elaboration. Constrained press sintering process is suggested to reduce the influence of these residual stresses during sintering, but this has to be adjusted not to destroy the free standing Ni window on the blister test specimens.

Thus blister test confirms its advantages as a quantitative technique for interface adhesion measurement. It is well adapted to any system including a ductile coating on a ductile or brittle substrate. Its theoretical analysis is very complete and consistent in literature. We propose an easy process to overcome difficulties in sample preparation for this powerful technique in the case of metal/ceramic systems. Reducing or correcting the influence of plasticity which occurs during film deformation also proves to be of major interest for present and future work.

Therefore, we could publish the first available values in literature for the practical adhesion energy of $Ag/BaTiO_3$ interfaces, and study the influence of interface microstructural characteristics such as the relation between interfacial porosity and critical interfacial energy release rate.

Thanks to our tests during this study, many data are also available now from the bulge part of the curves. Information on the elastic behaviour and the plastic constitutive law of the Ag films may be derived from these results; evolution of these characteristics with the membrane thickness, firing temperature, pore fraction of the material is an open subject, still to be completed.

Because the preparation of specimens for blister testing is rather delicate, one of our

goals was cross-testing of the blister test results with another appropriate adhesion measurement technique using specimens more simple to prepare or provided by external source. Among the many techniques available for interface adhesion measurement, those which are based on indentation tests seem to be appropriate, because of three main reasons:

- nano or micro-indentation apparatus are common in many laboratories;
- specimen preparation and geometry are very simple for indentation tests;
- these techniques can provide local measurement of interface toughness on small specimens.

Indentation test results:

More practical difficulties than expected have been met to prepare cross-sections of $Ag/BaTiO_3$ specimens. Interfacial debonding tends to initiate and propagate during the sample preparation even with careful operation. A proper sample fixation method had to be adapted for this preparation step.

Comparison between normal indentation, interface indentation and so-called "cross-sectional indentation" testing led us to keep this last technique as the most convenient and reliable among the three. It is based on indentation of the brittle substrate close to its interface with the coating, which causes a small substrate chip to push the coating film laterally and debond it from the substrate. We derived it from "cross-sectional nano-indentation test", which was promoted for adhesion measurement of thin films on silicon substrate by Berkovich nano-indentation, and we adapted this technique to Vickers micro-indentation on our metal/ceramic specimens. Several mechanical models are available to deduce the interface crack propagation energy from the measurement of the crack extension and film deflection after indentation.

- Difficulties for accurate crack length measurement on a millimeter range made it necessary to use Scanning Electron Microscopy for cross-sectional indented specimens. Some experimental techniques such as AFM may also be helpful to determine the exact position of the crack tip more accurately and study its surface deformation field for detailed information.

- We introduce a new mechanical model based on point-blister loading to analyze the results of cross-sectional indentation test. This model is based on the assumption of point-load and small deflection, owing to the observed overall dimensions of the debonded membrane.

- Comparison between various models for result analysis shows that point-load blister model leads to higher values of G_{ci} than the three other models. These higher values are close to the blister test results, but more analyses are necessary to improve and validate this model. Using and instrumented indentation testor which can record the load vs. depth curve could probably help in determining the exact value of the critical debonding load and of the mechanical work which is put into the specimen during the interface decohesion step. It would also be useful to be able to measure the debonded membrane deflection under load – rather than after the test completion – as it is done in blister testing.

So cross-sectional indentation tests appear to be well adapted to metal/ceramic

coatings, and we transposed this technique to micro-Vickers indentation which is very common and available in many laboratories.

However, we can conclude that indentation tests are not as easy to perform and analyze as they appear at first sight. The sample preparation needs to be done carefully to make sure that coatings do not debond before the test, and the exact position and orientation of the indent with regard to the interface must be controlled accurately. So it is not easy to obtain a large number of interpretable results on a given specimen.

The quantitative result of the test, in terms of interface crack propagation energy, is very sensitive to the crack length and membrane deflection measurements, and the various available models provide rather different values. More investigations are certainly necessary to compare and improve their results.

Published Work

1. "Adhesion strength of Ag/$BaTiO_3$ interface", C-Y LEE, M. DUPEUX and W-H TUAN, Scripta Materialia, Vol. 54, pp. 453-457 (2006).

2. "Influence of firing temperature on interface adhesion between screen-printed Ag film and $BaTiO_3$ substrate", LEE Chao-Yu, DUPEUX Michel, TUAN Wei-Hsing, Materials Science and Engineering A, 467 (2007) pp.125-131.

3. "Mesure d'énergie d'adhérence d'une couche métallique plastique sur un substrat céramique par gonflement-décollement", C-Y LEE, M. DUPEUX, W-H TUAN, M. BRACCINI, Poster au Colloque Annuel "Plasticité 2006", Sevrier (France), 26-28 Mars 2006.

APPENDIX I

Average propagation energy of a crack along a Ag/$BaTiO_3$ porous interface

(M. DUPEUX, work in progress, private communication)

A model based on simple geometrical and physical assumptions can be built to describe the effect of a given fraction of interfacial pores on the average propagation energy of a crack running along this porous interface. It is able to predict a non-linear scaling of this energy with the fraction area p of interfacial pores.

Let G_{ci} (J/m^2) be the reference crack propagation energy along the interface between two materials A and B with perfect and full contact at atomic scale, and let G_{cav} denote the same quantity averaged over a porous interface between the same materials. G_{cav} is due to be equal to G_{ci} when $p = 0$ and tends to 0 when p tends to 1. A linear relation between G_{cav} and the remaining fraction area of contact (1-p) is the simplest assumption which may be made to describe the effect of p on G_{cav}, but it is not confirmed by experimental results, as seen in Chap. V, Sec. 1.1.1.

The porous interface may be schematized as a periodic array of (a x a) square unit cells, each of them containing a square cavity (d x d) (figure A-1). We shall assume that the presence of the cavity perturbs the propagation of an incident crack (running from left to right on figure A-1) along an interfacial area (αd x αd), slightly larger than the size of the cavity ($\alpha > 1$). For many possible physical reasons which will not be discussed here, this perturbation may result in a different crack propagation energy called G_{cp}.

Then the total average amount of energy needed to propagate the crack along the unit cell area a^2 can be written as:

$$G_{cav}.a^2 = 0.d^2 + G_{ci}(a^2 - \alpha^2 d^2) + G_{cp}(\alpha^2 d^2 - d^2) \qquad \text{(A-1)}$$

from which, because of the definition of $p = d^2/a^2$:

$$G_{cav} = G_{ci}(1 - \alpha^2 p) + G_{cp}.p(\alpha^2 - 1) \qquad \text{(A-2)}$$

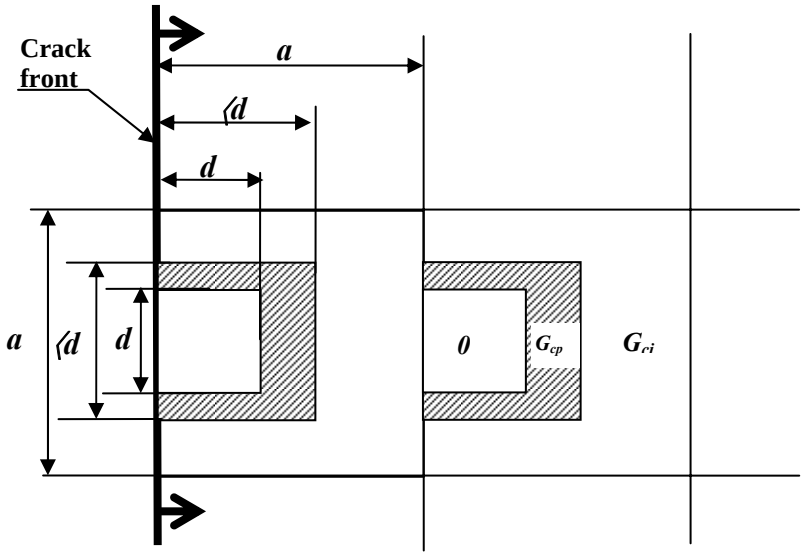

Figure A-1: schematic view of an interfacial unit cell with a porosity (d x *d) at the tip of a propagating crack and a perturbed area (αd* x *αd, for α ≅ 1.5) around the porosity* ***(αd < a)****.*

Of course, for a given value of α, if the interfacial porosity *p* increases, the validity of previous expression (A-2) is limited to the case where $\alpha d \leq a$. For larger pore sizes, the whole area of the unit cell is perturbed by the presence of the cavity (figure A-2) and the total amount of average propagation energy is expressed under the form:

$$G_{cav}.a^2 = 0.d^2 + G_{cp}(a^2 - d^2) \qquad \text{(A-3)}$$

which gives:

$$G_{cav} = G_{cp}(1-p) \qquad \text{(A-4)}$$

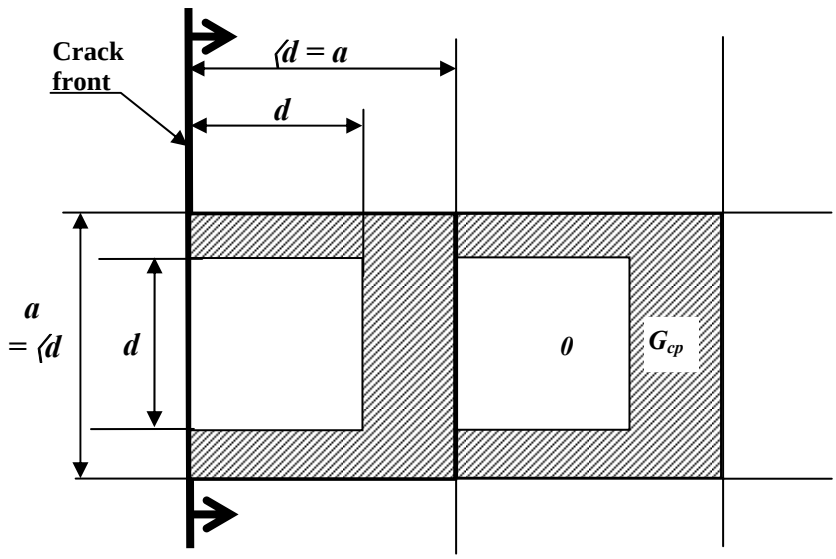

Figure A-2: schematic view of an interfacial unit cell with a porosity (d x *d) at the tip of a propagating crack and a perturbed area (αd* x *αd, for α ≅ 1.5) around the porosity* ***(αd ≥ a)****.*

The two equations (A-2) and (A-4) describe two different linear regimes of variation of G_{cav} with p. As needed from physical limit cases,

- in the first regime, the average energy G_{cav} tends to G_{ci} when p tends to 0.
- in the second regime, G_{cav} tends to 0 when p tends to 1.
- if $G_{cp} = G_{ci}$, both expressions lead to the simple linear interpolation $G_{cav} = G_{ci}.(1-p)$.
- the transition between the two regimes occur when $\alpha d = a$, i.e. $p = 1/\alpha^2$, which depends on the value of the dimensionless constant α.
- if $G_{cp} = 0$ (which actually means that the true debonded area is (αd x αd), even if it cannot be detected), G_{cav} tends to 0 for the transition value of $p = 1/\alpha^2$.

Limiting values for the couple of parameters (α, G_{cp}) of this simple model can be found by looking for a realistic fit with the experimental crack propagation energy values measured in function of the porosity rate (Chap. V, figure 5-11), according to the following criteria (see figure A-3):

i) the transition value of porosity $p = 1/\alpha^2$ must be at least 0.15, according to the experimental linear decrease of measured values. This means that $\alpha \leq 2.6$ is needed

ii) the largest value of G_{cp} compatible with experimental values is $G_{cp} = 3$ J/m^2, from the extrapolation of regime 2 to $p = 0$ through the lowest experimental point ($G_{cav} = 2.7$ J/m^2, $p = 0.15$). This also means that $\alpha \leq 2.6$.

iii) the smallest possible value $G_{cp} = 0$ J/m^2, introduced in equation (A-2), can only be compatible with the experimental points for $\alpha = 2.2$.

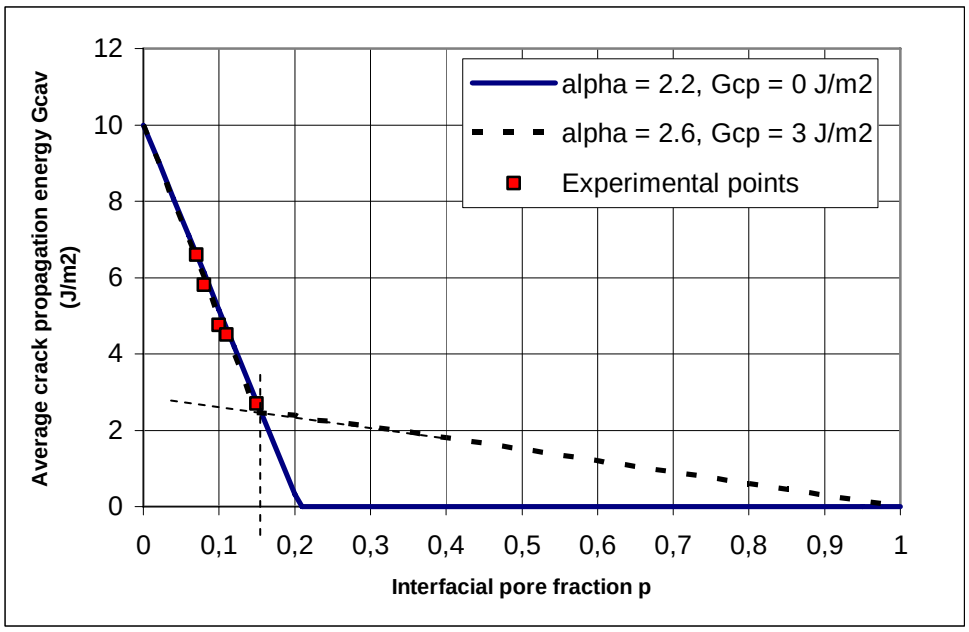

Figure A-3: variation of the average Ag/$BaTiO_3$ interfacial crack propagation energy with the interfacial pore fraction

Therefore the following conclusions may be derived:

- The two successive different linear regimes of variation of G_{cav} with p, as described by this simple model, are perfectly compatible with the experimental data of $Ag/BaTiO_3$ interfacial crack propagation energy measurements.
- The reference crack propagation energy of the perfectly bonded interface G_{ci} is around 10 J/m^2.
- The interfacial porosities in the $Ag/BaTiO_3$ interface are likely to perturb the crack propagation along an area between 2.2 and 2.6 times wider than the observed pore size.
- This perturbation results in a locally much weaker interface, with a crack propagation energy between 0 and 3 J/m^2.